UPPSALA
UNIVERSITET

In the confines of Cu(In,Ga)Se$_2$ thin film solar cells with rear surface passivating oxide layers

DOROTHEA LEDINEK

Dissertation presented at Uppsala University to be publicly examined in Room 80101, Ångströmlaboratoriet, Lägerhyddsvägen 1, Uppsala, Monday, 30 September 2019 at 09:30 for the degree of Doctor of Philosophy. The examination will be conducted in English. Faculty examiner: Dr. Christian Kaufmann (Helmholtz Zentrum Berlin).

Abstract
Ledinek, D. 2019. In the confines of $Cu(In,Ga)Se_2$ thin film solar cells with rear surface passivating oxide layers. *Digital Comprehensive Summaries of Uppsala Dissertations from the Faculty of Science and Technology* 1834. 118 pp. Uppsala: Acta Universitatis Upsaliensis. ISBN 978-91-513-0713-8.

The material supply to build renewable energy conversion systems needs to be considered from both a cost and an energy security perspective. For $Cu(In,Ga)Se_2$ (CIGS) thin film solar cells the use of indium in the absorber layer is most problematic. The material input per service unit can be reduced, if the absorber layers are thinned down without a loss in power conversion efficiency.

Thinning down absorber layers can increase the conversion efficiency. However, for real CIGS solar cells absorption losses and recombination rates at the rear surface between the CIGS absorber and the Mo rear contact as well as shunt-like behavior increase. Thus, both rear surface passivation and optical management are essential for maintaining high power conversion efficiencies.

In this work, thin oxide layers, so-called passivation layers, are introduced between the CIGS absorber layer and the Mo contact. They can passivate the CIGS surface, if the CIGS-oxide interface has a lower defect density than the CIGS-Mo interface and/or if they contain a negative fixed oxide charge, which increases the hole concentration and reduces the electron concentration in the CIGS in the vicinity of the oxide.

As these oxides are insulators, electrical conduction through the passivation layer has to be ensured. In this work, nanopoint contacts were etched into $ALD-Al_2O_3$ passivation layers in CIGS solar cells. These solar cells had 0.5 -1.5 µm thin absorber layers with a low In content and a high band gap. Ga grading was not used. Although absorber layers with a high Ga content have a short minority carrier diffusion length, a passivation effect could be discerned with the help of external quantum efficiency measurements and current-voltage measurements under varying temperatures in combination with optical and electrical modeling with a two-diode model. Moreover, the possibility of leaving out the additional fabrication step has been explored for $ALD-Al_2O_3$ and HfO_2 as passivation layers. The results suggest that the passivation layer does not necessarily need to be opened for electrical conduction in an additional fabrication step, if sodium fluoride (NaF) is deposited onto Al_2O_3 layers prior to CIGS evaporation. In this case solar cells with 215 nm absorber layers and 6 nm thin passivation layers have a power conversion efficiency of 8.6 %, which is 3 % (absolute) higher than the conversion efficiency on a reference. Shunt-like behavior is additionally reduced. For the HfO_2 layers photoluminescence data indicate a good passivation effect, but the layers need to be opened up to ensure conduction.

Keywords: Alkali, Alumina, Back contact, CIGS, CIGSe, Hafnia, Passivation, Rear contact, Sodium fluoride, Ultra-thin

Dorothea Ledinek, Department of Engineering Sciences, Solid State Electronics, Box 534, Uppsala University, SE-75121 Uppsala, Sweden.

To everybody who lifted me up on my way, even if only a tiny bit

List of Papers

This thesis is based on the following papers, which are referred to in the text by their Roman numerals.

I   Ledinek, D., Vermang, B., Edoff, M. (2014) Thickness and Ga-content variations in co-evaporated CIGS solar cells with a flat Ga profile – An electrical characterization. *Proceedings 29th European Photovoltaic Solar Energy Conference and Exhibition*, 1: 1832-1836

II   Ledinek, D., Salomé, P., Hägglund, C., Zimmermann, U., Edoff, M. (2018) Rear Contact Passivation for High Band gap Cu(In,Ga)Se$_2$ Solar Cells with a Flat Ga profile. *IEEE Journal of photovoltaics*, 8(3):864-870

III   Ledinek, D., Donzel-Gargand, O., Sköld, M., Keller, J., Edoff, M. (2018) Effect of different Na supply methods on thin Cu(In,Ga)Se$_2$ solar cells with Al$_2$O$_3$ rear passivation layers, *Solar Energy Materials and Solar Cells.* 187:160–169

IV   Ledinek, D., Keller, J., Hägglund, C., Chen W.-C., Edoff, M. (2019) Effect of NaF precursor on alumina and hafnia rear contact passivation layers in ultra-thin Cu(In,Ga)Se$_2$ solar cells, *Thin Solid Films*, 683: 156-164

My contributions to the papers

I   Part of planning, most of sample production; all profilometer, XRF, *JV, EQE*, *AQE* measurements; all data analysis and modeling; all figures; all article writing with feedback from co-authors.

II Planning of experiments in detail; all sample processing apart from passivation layer opening; all XRF, *JV, JV(T), EQE* and spectrophotometry measurements; all graphs; all data analysis; electronic device modeling together with one of the co-authors; all article writing apart from paragraph on optical modeling with feedback from co-authors.

III Part of planning the experiments, part of experimental work and supervision of the rest of the experimental work carried out by a master student; all extended data analysis; all modeling; most graphs; all writing apart from TEM related parts with feedback from co-authors;

IV Planning of experiments in detail; all sample processing apart from photolithography and deposition of HfO_2 layers; all profilometer, spectrophotometry, XRF, *JV, EQE, AQE* and PL measurements; all data analysis; writing with input from the co-authors especially on the parts on HfO_2 ALD-deposition, TEM analysis and photolithography; all figures apart from TEM related figures.

Contents

Abbreviations and symbols

Symbol	Description or physical quantity	Unit
A	Diode ideality factor	
A_0	Universal Richardson constant	A/(cm^{2}K^2)
$A(\lambda)$	Absorptance/absorbance	
AIGS	Ag(In,Ga)Se$_2$	
AFM	Atomic force microscopy	
ALD	Atomic layer deposition	
A_{par}	Parasitic absorptance at the rear contact	
AQE	Apparent quantum efficiency	
b	Position of the rear surface	
BF	Bright field	
c	Velocity of light	cm/s
CBD	Chemical bath deposition	
CGI	Cu-content in the absorber layer; [Cu]/([In]+[Ga])	
CIGS	Cu(In,Ga)Se$_2$	
c-Si	Crystalline silicon	
CV	Capacitance-voltage	
d_a	Thickness of the absorber layer	cm
d_{bu}	Thickness of the buffer layer	
d	Position of the quasi-neutral boundary between bulk and contact region	
D^e	Electron diffusion coefficient	cm/s
DF	Dark field	
D^h	Hole diffusion coefficient	cm/s
DI	Deionized	
E	Energy per electron hole pair	
e, e_0	Elementary charge	As
E_a	Activation energy	eV
EDX	Energy dispersive X-ray spectrometry	
EELS	Electron energy-loss spectrometry	
E_G	Energy of the band gap	eV
EQE	External quantum efficiency	

E_t	Energy level of a defect	eV
E_V	Energy of holes at the valence band edge	eV
F	Free Energy per electron-hole pair	eV
FF	Fill factor	
FIB	Focused ion beam	
G	Shunt resistance (one diode model)	S/cm^2
$G(x)$	Generation function, local generation rate	1/(cm^{3}s^1)
G_b	Shunt resistance in parallel to rear diode	S/cm^2
G^e	Total generation rate for electrons	1/(cm^{3}s^1)
G^h	Total generation rate for holes	1/(cm^{3}s^1)
GGI	Ga content; [Ga]/[Ga]+[In]	
$G_n(x,\lambda)$	Normalized spectral generation function	
$G_{0,r}{}^h$	Radiative generation rate for holes due to thermal back-ground radiation in equilibrium	1/(cm^{3}s^1)
$G_{0,r}{}^e$	Radiative recombination rate for electrons due to thermal back-ground radiation in equilibrium	1/(cm^{3}s^1)
$G_{ph}(x,\lambda)$	Spectral generation function	1/(cm^{3}s^1)
$G_{ph}{}^e$	Generation rate for free electrons due to illumination	1/(cm^{3}s^1)
$G_{ph}{}^h$	Generation rate for free holes due to illumination	1/(cm^{3}s^1)
$G_r{}^e$	Radiative recombination rate for electrons	1/(cm^{3}s^1)
$G_r{}^h$	Radiative generation rate for holes	1/(cm^{3}s^1)
$h, \hbar$	Planck's constant, reduced Planck's constant	eVs
HAADF	High-angle annular dark field	
i	Intrinsic	
I	Current	A
IQE	Internal quantum efficiency	
IV	Current-voltage	
J	Current density	A/cm^2
J_{dark}	Dark current density	A/cm^2
J_{diode}	Diode current density	A/cm^2
j_γ	Photon current density/photon flux density	1/(cm^{2}s^1)
J_{gen}	Generation current density	A/cm^2
J_{light}	Total current density under illumination	A/cm^2
J_{mp}	Current density at the maximum power point	
J_0	Saturation current density	A/cm^2
J_{0m}	Saturation current density of the main diode	A/cm^2
J_{0b}	Saturation current density of the rear diode	A/cm^2
J_{0beff}	Effective saturation current density of the rear diode	A/cm^2

$J_{0,r}$	Saturation current density due to radiative recombination/generation	A/cm^2
J_{00}	Reference current density of a diode	A/cm^2
J_{00m}	Reference current density of the main diode	A/cm^2
J_{00b}	Reference current density of the rear diode	A/cm^2
J_{ph}	Photocurrent density	A/cm^2
J_{phb}	Photocurrent density from the rear diode	A/cm^2
$J_{ph,EQE}$	Photocurrent density determined by EQE measurements	A/cm^2
$J_{ph,loss}$	Photocurrent density loss	A/cm^2
$J_{ph,m}$	Photocurrent density from the main diode	A/cm^2
J_{rec}	Recombination current density	A/cm^2
J_{recb}	Recombination current density at the rear surface	A/cm^2
J_{SC}	Short current density	A/cm^2
JV	Current-density-voltage	
$JVT, JV(T)$	Temperature dependent JV	
k	Boltzmann's constant	eV/K
LED	Light-emitting diode	
L_{QNR}	Minority carrier diffusion length in the quasi-neutral region	cm
L^e	Diffusion length for electrons	cm
L^h	Diffusion length for holes	cm
L_r^e	Radiative diffusion length for electrons	cm
L_r^h	Radiative diffusion length for holes	cm
MIS	Metal-insulator-semiconductor	
MPP	Maximum power point	
n	Electron concentration	1/cm^3
N_A	Acceptor concentration	1/cm^3
N_C	Effective density of states in the conduction band	1/cm^3
N_b	Electron concentration in the semiconductor at the rear surface	1/cm^3
n_d	Electron concentration at the quasi-neutral boundary between bulk and contact region	1/cm^3
N_D	Donor concentration	1/cm^3
n_0	Equilibrium electron concentration	1/cm^3
n_i	Intrinsic carrier concentration	1/cm^3
n_p	Electron concentration in a p-doped semiconductor layer	1/cm^3
N_V	Effective density of states in the valence band	1/cm^3

O_i	Oxygen interstitials	$1/cm^3$
p	Hole concentration	$1/cm^3$
P	Power density	W/cm^2
PL	Photoluminescence	
P_{mp}	Power density at the maximum power point	W/cm^2
p_n	Electron concentration in an n-doped semiconductor	$1/cm^3$
p_0	Equilibrium hole concentration	$1/cm^3$
Post-DT	Post-deposition treated/treatment	
Pre-DT	Pre-deposition treatment/treated, i.e. precursor layer	
q	Elementary charge	As
QMA	Quadrupole mass analyzer	
QNR	Quasi-neutral region	
R	Total reflectance of a solar cell	
R^e	Total recombination rate for electrons	$1/(cm^3s^1)$
R^h	Total recombination rate for holes	$1/(cm^3s^1)$
$R_{0,r}$	Radiative recombination rate at equilibrium	$1/(cm^3s^1)$
RF	Radio frequency	
R_S	Series resistance	$\Omega \cdot cm^2$
S	Entropy loss	eV/K
SCAPS	Solar cell capacitance simulator	
SCR	Space-charge region	
SE	Spectroscopic ellipsometry	
SEM	Secondary electron microscopy	
SLG	Soda-lime glass	
S_0^e	Electron surface recombination velocity at the rear surface	cm/s
S_0^h	Hole surface recombination velocity at the rear surface	cm/s
S_{eff}	Effective surface recombination velocity at the rear surface	cm/s
SRH	Shockley-Read-Hall	
STEM	Scanning transmission electron microscopy	
T	Temperature	K or ºC
t	Time	s
TEM	Transmission electron microscopy	
T_w	Transmittance of the window layer	
u	Normalized excess np-product	

U_b	Net recombination rate at the rear surface	$1/(cm^3 s^1)$
U^e	Net recombination rate for electrons	$1/(cm^3 s^1)$
U^h	Net recombination rate for holes	$1/(cm^3 s^1)$
U_r^e	Net rate for radiative recombination for electrons	$1/(cm^3 s^1)$
U_r^h	Net rate for radiative recombination for holes	$1/(cm^3 s^1)$
V	Bias voltage	V
V_{Al}	Aluminum vacancy	
V_O	Oxygen vacancy	
V_{OC}	Open-circuit voltage	V
V_{OCb}	Open-circuit voltage over the main diode	V
V_{OCm}	Open-circuit voltage over the rear diode	V
v_{th}^e	Thermal velocity for electrons	cm/s
v_{th}^h	Thermal velocity for holes	cm/s
V_{UL}	Upper-limit voltage	V
w_a	Width of the SCR/depletion region of the main junction in the absorber	cm
XPS	X-ray photoelectron spectroscopy	
XRF	X-ray fluorescence	
α_a	Absorption coefficient of the absorber layer	1/cm
β	Radiative generation constant	cm^3/s
ε	Dielectric constant	$As/(V{\cdot}cm)$
ε_{Fmet}	Fermi energy in the contacting metal	eV
ε_F	Fermi energy at equilibrium (without voltage or light bias)	eV
ε_i	Intrinsic Fermi level	eV
$\eta_C(x,V,j_\gamma)$	Collection function	
$\eta(V,j_\gamma)$	External collection efficiency, describes the dependence of the photocurrent collection on voltage and light bias	
κ	Transmission coefficient (an empirical parameter)	
λ	Wavelength	cm
$\lambda_{g,a}$	Wavelength corresponding to the absorber band gap	cm
$\lambda_{g,w}$	Wavelength corresponding to the window layer band gap	cm
μ	Chemical potential	eV
μ^e	Electron mobility	$\Omega{\cdot}cm$
μ^h	Hole mobility	$\Omega{\cdot}cm$
ρ_{beff}	Effective ohmic resistivity at the rear contact	$cm^2/(V{\cdot}s)$
ρ_{bohm}	Ohmic resistivity at the rear contact (MIS model)	$cm^2/V{\cdot}s$
σ	Standard deviation	

σ^e	Conductivity for electrons	S/cm
σ^h	Conductivity for holes	S/cm
$\sigma_{rec}{}^e$	Recombination cross section for electrons	cm^2
$\sigma_{rec}{}^h$	Recombination cross section for holes	cm^2
φ	Electrical potential	V
φ_0	Electrical potential under equilibrium conditions	V
$\varphi_b{}^e$	Electron barrier height at the rear contact	eV
$\varphi_b{}^h$	Hole barrier height at the rear contact	eV
ψ_b	Surface potential at the rear contact	V
ω	Angular frequency of a photon	rad/s
Ω	Solid angle	sr

Introduction

Efforts are being made worldwide to transition from fossil energy sources to renewable energy sources like solar energy, as fossil energy sources have severe limitations. Firstly, both the amount and the exploitation rate of fossil energy resources are limited. Secondly, fossil energy resources are unevenly distributed over the globe to the disadvantage of regions with a low density. Therefore, fossil energy prices and supply are partially politically determined and fluctuate heavily, endangering energy security[1]. Finally, the use of fossil energy is the main contributor to human-caused global warming[2].

Renewable energy resources are however not directly usable, but an energy system component needs to convert them into an energy carrier or secondary energy, which in turn can provide an energy service to the end consumer[3]. Solar cells are such a renewable energy conversion system. They convert solar energy into electrical energy, which can be finally converted for example into potential energy, when a mechanic lifts a weight with a crane. Thus, the material supply to build renewable energy conversion systems needs also to be considered from both a cost and an energy security perspective. The amount and the production rate of materials from primary and secondary resources (i.e. from end-of-life recycling) are in principle limited and exploitable ores are unevenly distributed over the globe. Shortages and large price fluctuations are thus not uncommon. For $Cu(In,Ga)Se_2$ (CIGS) thin film solar cells it is indium in the absorber layer that is most problematic[4].

Thus, a reduction of material input per unit of service (MIPS)[5] can enhance energy security and help to stabilize and/or decrease the levelized cost of energy despite finite material resources. Everything else being equal, the material input per unit of service is reduced, if (1) the same amount of energy services is provided with less material input to the energy conversion system or (2) if the amount of energy service provided is increased for the same material input.

In the case of solar cells for example, the material input per service unit is reduced, if the absorber layers are thinned down without a loss in power conversion efficiency or if the conversion efficiency is enhanced without an increase in material usage. A loss in conversion efficiency is especially detrimental to the levelized cost of energy[6] from photovoltaics, as the so-called balance of system costs, such as framing and mounting materials, cabling, inverters and labor costs for the installation make up a large and increasing share of the turnkey price of photovoltaic systems. As the balance-

of-system costs scale more with the module area of the photovoltaic installation than with its power conversion efficiency, it is important to maintain or increase power conversion efficiencies, even though production cost or material input at module level are decreased[7].

Fortunately, thinning down absorber layers can in principle increase the conversion efficiency. When absorber layers are thinned down, the same number of excess free charge carriers is confined into a smaller absorber volume, assuming an equal total generation rate and equal recombination rates at the front and rear surfaces. Elevated free charge carrier concentrations in the absorber bulk widen the splitting of the quasi-Fermi levels and can finally increase the open-circuit voltage.

However, for real CIGS solar cells, both absorption losses and recombination rates at the surface between the CIGS absorber and the Mo rear contact increase when thinning down absorber layers. The splitting of the quasi-Fermi levels in the absorber bulk, the open-circuit voltage, the short-circuit current density, the fill factor, and thus the power conversion efficiency decrease instead. Thus, both rear surface passivation and optical management[8] are essential for maintaining high power conversion efficiencies in CIGS solar cells, when the solar cells' absorber layers are thinned down.

Rear surface passivation reduces per definition the local recombination rates at the rear surface. A surface can be passivated by either reducing the density of defects at the surface (chemical passivation) and/or by making one carrier concentration much smaller than the other (carrier population control), thereby inhibiting recombination[9]. The absorbers in state-of the art CIGS solar cells are commonly Ga graded with high Ga contents close to the rear surface to elevate the hole concentration and reduce the electron concentration at the rear surface[10]. Instead, in this work, thin oxide layers, so-called passivation layers, are introduced between the CIGS absorber layer and the contact. They can passivate the CIGS surface, if the CIGS-oxide interface has a lower defect density than the CIGS-Mo interface and/or if they contain a negative fixed oxide charge, which similarly to the Ga grading increases the hole concentration and reduces the electron concentration in the CIGS in the vicinity of the oxide.

As oxides are insulators, electrical conduction through the passivation layer has to be ensured. This is commonly done by opening the passivation layer in an additional fabrication step[11,12], thereby establishing a direct electrical contact between the CIGS absorber layer and the Mo rear contact. Accordingly, in a part of this work nanopoint contacts have been etched into the oxide passivation layers in solar cells. These solar cells had CIGS absorbers with a high band gap, i.e. CIGS with a high Ga content and a low In content, as GIGS with high Ga contents is used at the rear of state-of-the-art CIGS solar cells[13]. Additionally, the possibility of leaving out the additional fabrication step has been explored for two different oxides. The results

suggest, that the passivation layer does not necessarily need to be opened for electrical conduction in an additional fabrication step, if the appropriate combination of passivation material and sodium fluoride (NaF) deposition is used.

Overview

In a first attempt (**paper I**), I produced, electrically characterized and electrically modeled a series of unpassivated CIGS solar cells to get acquainted with both processing and trends for primary and secondary solar cell parameters in dependence on the GGI = [Ga]/([Ga]+[In]) = 0.15, 0.30, 0.45, 0.60 of the absorber layer and its thickness d_a = 0.5, 1.0 and 1.5 µm. The absorber layers in CIGS solar cells are usually about 2 µm thick, much thinner than a hair (50 µm) and silicon solar cells (300 µm). Like for all solar cell samples in this work, elemental grading of the absorbers was not used to avoid its passivating effects.

High values of the GGI are used at the rear surface of state-of-the-art solar cell devices to reduce recombination at the rear surface. Therefore, I explored the influence of Al_2O_3 rear surface passivation layers on solar cells with absorbers with high band gaps/GGI (**paper II**). Thereby, I varied the thickness of the absorber layers, because the influence of rear surface recombination increases with declining absorber layer thickness. I described the current density-voltage characteristics of passivated and unpassivated reference solar cells by an equivalent circuit model (**papers II and III**) with two diodes in series. In this model, one diode describes the main junction and the other a hole barrier at the rear contact. By varying the temperature during the current-voltage measurements, four current density components over the rear contact could be discerned, one of them being a detrimental photocurrent density. This component of the current density increases for thinner layers and is reduced by passivation layers (**paper II**).

As Al_2O_3 is an insulator, point contacts were created by opening nanoholes in the passivation layer in **paper II**. To explore, if the costly patterning step can be avoided, the possibility of conduction via tunneling was explored in **paper III** by varying the Al_2O_3 layer thickness in another solar cell series. As Na is assumed to reduce the majority carrier barrier at the rear contact, Na was added in the form of NaF and the deposition methods and amount of NaF were additionally varied. The two-diode model was applied again and allowed for an estimation of the majority carrier barrier for these constellations.

Surprisingly, current density-voltage curves for solar cells that were processed with a NaF precursor layer on top of the Al_2O_3 layer did not show any signs of photocurrent blocking regardless of the Al_2O_3 layer thickness. On the other hand, if no precursor layer was applied, the photocurrent was increasingly blocked for increasing passivation layer thickness as expected.

As **paper III** had only proven the concept, but not the effectiveness of unpatterned Al_2O_3 passivation layers, the absorber thickness was reduced from 1 μm in **paper III** to 215 nm in the final study (**paper IV**). Such a reduction of the absorber thickness increases the impact of rear surface recombination on the solar cell parameters and a passivation effect can thus be more easily shown. Furthermore, I was curious if other oxides could be used as rear surface passivation layers and if the extra patterning step could be avoided for those materials. Due to its promising characteristics as a passivation material for silicon solar cells, we identified HfO_2 as a candidate. The HfO_2 layers however blocked the photocurrent despite NaF precursor layers, but the results of photoluminescence measurements indicate that HfO_2 also passivates the rear surface, i.e. it reduces the interface recombination rate.

In the following thesis summary, I rearrange the content that has been split up into four papers to give perspectives and contexts that were not elucidated in the papers. Additionally, I reflect on a fundamental shift in the understanding of solar cells and of junctions, both the pn-junction at the front contact and the semiconductor-metal junction at the rear contact.

This thesis summary also documents how I struggled with limited resources in the broadest sense, the messy reality of science and the confrontation with the border of human knowledge, while researchers improved standardized power conversion efficiencies from 19.6% to 22.9% [14,15] for CIGS solar cells. It is a tiny, blurry, broken and bumpy mirror of the world that enlarges certain aspects and shrinks others into oblivion. It leaves much unsaid under the cloak of objectivity and scientificity. It reflects the epistemologies of its time and place; it mirrors the physical, human and knowledge resources that were available to me under this period; it reveals some aspects of my relationships with this world; it mirrors a tiny part of me.

1 CIGS solar cell structure and processing
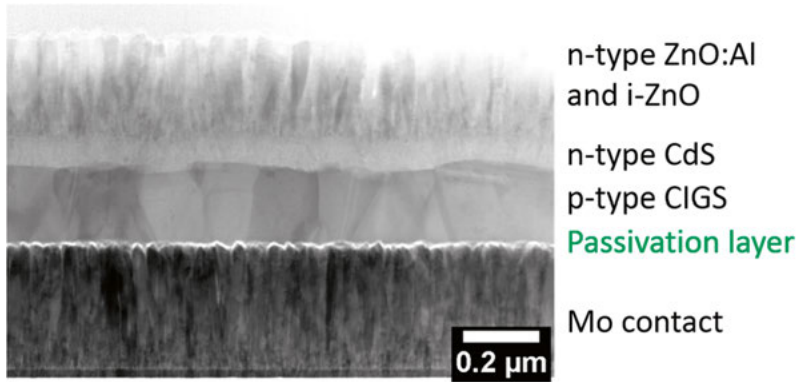
Figure 1. Cross-section of an ultra-thin CIGS solar cell reproduced from **paper IV**. A rear surface passivation layer has been added to the baseline CIGS solar cell process and the absorber thickness d_a has been reduced to only 215 nm. Image credit: Lars Riekehr.

In thin film processing, the different functional layers of a device are sequentially deposited on a substrate. The thin film solar cell group at the Ångström Laboratory in Uppsala uses a baseline approach for processing solar cells. In a baseline approach, the processing of all layers is kept as constant as possible for all batches and only few parameters are intentionally varied. Thereby, ideally, these intentional changes in processing can be connected to changes in the solar cells' electrical and optical characteristics. The baseline solar cells are built in the substrate configuration and have a soda-lime glass/Mo/CIGS/CdS/i-ZnO/ZnO:Al/Ni/Al/Ni stack. Instead of the inline-co-evaporation system described in the "baseline paper"[16], a Balzer's BAK was used for CIGS co-evaporation in all of this work.

I have intentionally
- added oxide passivation layers between the Mo rear contact and the CIGS absorber to reduce the recombination rate at the rear surface (**papers II, III and IV**),
- added alkali-diffusion blocking layers onto the glass substrate to compare the impact of Na on solar cells with and without rear surface passivation layers (**paper III**),

- added NaF precursor layers onto the passivation layers (**papers III and IV**) to supply Na to the absorber layer when the Na supply from the glass is blocked,
- added a NaF in-situ post-deposition treatment of the CIGS layer (**papers II and III**), which is another way to supply Na to the absorber layer if Na diffusion from the glass is blocked,
- varied the thickness of the CIGS layer (**papers I, II**),
- varied the composition of the CIGS layers (**paper I**),
- varied the material of the passivation layer **(paper IV**) to compare their effectiveness as a passivation layer and their sensitivity to NaF,
- varied the thickness of the passivation layers (**paper III**) and NaF precursor layers (**papers III, IV**) to optimize the combination of passivation layer thickness, material and NaF supply.

In **paper IV** the cells were not mechanically scribed but separated by etching assisted by a photolithography process. *Figure 1* depicts a solar cell from **paper IV**, with an ultra-thin CIGS layer and a passivation layer between the Mo contact and the CIGS layer.

Despite the baseline approach, reproducibility is hard to achieve over longer time periods. Therefore, in this thesis all passivated samples are compared to reference samples that were produced under the most similar conditions possible and comparison of runs over long periods of time serve mostly to exclude production errors.

In the following chapter, I describe the baseline processes based on [16] and the functionality of the layers based on [17] and [18]. I also describe those processes and layers that I used but are not part of the baseline.

1.1 Soda-lime glass substrates

Low-iron soda-lime glasses (SLG) with a thickness of 1 mm or 2 mm are used as substrates. SLG is available at large quantities and at low cost, electrically insulating and stable up to 550°C. Its thermal expansion coefficient matches the expansion coefficient of the absorber layer well and it has a smooth surface. If no layers blocking alkali-diffusion are deposited onto the glass, Na diffuses during CIGS co-evaporation from the glass through the oxygenated grain boundaries of the Mo rear contact into the CIGS layer. The effects of Na on CIGS deserve its own chapter in this work (see chapter 4).

Before Mo sputtering, the substrates are cleaned to increase reproducibility. They are immersed into a tank with deionized (DI) water at room temperature and Cole-Parmer Micro-90 detergent. The tank is subsequently heated to 60°C and put into an ultrasonic cleaning bath. After the cleaning step, the glass sheets are rinsed four times in 60°C warm DI water using ultrasonic agitation. Finally, the substrates are dried in a spin rinse dryer in a nitrogen atmosphere.

1.2 Sputtering the Mo rear contact

The polycrystalline Mo rear contact layer is deposited in a vertical inline MRC 603 direct current magnetron sputtering system using a Mo target. A first layer is deposited at high sputter gas pressure and a second layer at low sputter gas pressure. The first layer is under tensile stress and thus adheres better to the glass, but it suffers from a low conductivity. The second layer has a high conductivity. The sheet resistance of the resulting Mo (double-)layer is 0.6 ± 0.1 Ω/square and its thickness is 350 ± 20 nm.

Mo is used as a rear contact, because it is cheap and stable against alloying with Cu, In and Ga during the CIGS co-evaporation. However, a part of the Mo layer reacts with Se to form a thin film of $MoSe_2$, which is a layered semiconductor with an indirect band gap of 1.06-1.16 eV. The questions, whether the rear contact is completely "ohmic" and whether Na and/or $MoSe_2$ layer affect the barrier height for holes are however still under discussion. **Paper II** contributes regarding this topic. Additionally, the properties of the Mo layer influence the Na transport from the glass to the CIGS.

1.3 Atomic layer deposition of Al_2O_3 and HfO_2 rear surface passivation layers

Rear surface passivation layers are not a part of the baseline process, but are added in the experimental work for **papers II, III and IV** to study their influence on device performance and their sensitivity to NaF precursor layers. HfO_2 (Hafnia) is grown by atomic layer deposition (ALD) in a Picosun Sunale R200 hot wall, viscous flow reactor. Tetrakis(dimethylamino)hafnium(IV) (TDMAH, Sigma Aldrich) and water serve as precursors. The substrate temperature is 170°C and the TDMAH source container is heated to 75°C. The HfO_2 layer grows linearly at a velocity of 1.2 Å/cycle, as observed by in-situ spectroscopic ellipsometry and from TEM (transmission electron microscopy) cross sections.

To deposit the Al_2O_3 layers, trimethylaluminum (TMA) and water are used as reactants and nitrogen is used a purge gas in another Picosun Sunale R200 ALD system. In this case, the substrate temperature is 300°C and the precursors are kept at room temperature. A constant growth rate of 0.9 Å is achieved according to ex-situ spectroscopic ellipsometry.

For the study on high band gap solar cells (**paper II**), a quadratic pattern of contact openings, each with a length of 0.7 μm and a width of 0.4 μm and a pitch of 2 μm between the openings, was carefully etched into the Al_2O_3 layer by reactive ion etching after defining the pattern using electron beam lithography as in reference[11]. The diameter and depth of the contact openings was determined by atomic force microscopy in tapping mode to verify that the etching process was complete. Such a patterned rear surface is

sometimes referred to as partial rear contact, as only a part of its surface conducts current and serves as a contact in a more narrow sense[19–21].

1.4 Co-evaporation of the CIGS absorber

The polycrystalline CIGS layer is the absorber of the CIGS solar cell. It is intrinsically p-doped due to defects (most likely Cu vacancies V_{Cu}) and has – as a direct band gap semiconductor – a high absorption coefficient in the order of 10^4 to 10^5 cm^{-1}.

The polycrystalline CIGS absorber layer is co-evaporated in a vacuum chamber (Balzer BAK 550). Before the CIGS deposition, the samples are cut into 5 cm × 5 cm pieces that later contain 32 cells with an area of 0.5 cm^2 or into 2.5 cm × 5 cm pieces that later contain 12 cells of the same size. The sample holder has space for up to three 5 cm x 5 cm substrates and is heated from the back side by infrared radiation from halogen lamps. The temperature of the substrate holder is measured with a thermocouple which is inserted in a hole in the substrate holder and thereby is in thermal equilibrium with the substrate holder. The power of the lamps is adjusted via a feedback loop controlled by a computer to achieve a predefined profile. The heat source was rebuilt between sample production for **papers I and II** and the sample holder was exchanged for a sample holder with less thermal mass for increased temperature dynamics during cool-down. Between **papers II and III** a graphite plate was added on top of the samples to increase the thermal mass again, since the temperature fluctuated unintentionally for the low thermal mass.

Cu, In and Ga are evaporated from open-boat sources and Se is evaporated in excess from an effusion cell. The individual metal evaporation rates are monitored by a Balzer QmG 420 quadruple mass spectrometer and computer-controlled feedback loops control the electrical power to the sources individually. In this way, the actual evaporation rates follow the pre-defined evaporation rates and constant elemental profiles can also be achieved for very thin absorber layers as confirmed by energy-dispersive X-ray spectroscopy (EDX) for the samples in **paper IV**. As the relationship between the actual rates and the pre-determined rates shifts over time, the actual composition is evaluated by x-ray fluorescence (XRF). To achieve an as similar composition as possible for different CIGS layer thicknesses in **papers I and II**, the evaporation rates were not changed, but the evaporation time was adjusted accordingly. The temperature of the sample holder is lower at the beginning of the deposition to facilitate nucleation and increases to the end of the process. In this work, the substrates had temperatures between 410 to 530ºC during the evaporation and the times for evaporation ranged between about 5 and 20 minutes.

In all my work all elements were evaporated with constant evaporation rates. The CIGS is Cu poor, with a $CGI = [\text{Cu}] / ([\text{Ga}] + [\text{In}])$ of 0.8-0.9, whereas a $CGI = 1$ would indicate stoichiometry. Stoichiometry means that the elements have the same atomic ratios as given in the chemical sum formula. No intermediate Cu-rich stage ($CGI > 1$) that would facilitate larger grain sizes was used and a Cu-rich end product was avoided to avert the agglomeration of binary phases that shunt the cells.

The co-evaporation process can be unstable from run to run, so that only CIGS layers produced in one run or at least within few days can be reliably compared. Additionally, the maximum number of 0.5 cm^2 devices that can have their CIGS layer co-evaporated in one evaporation run is also severely limited and the number of devices per sample needs to be weighed against the number of samples that can be compared with each other. In **paper I**, two samples of 12 cells with the same sample stack were produced in the same co-evaporation run. All CIGS layers with a certain GGI were co-evaporated on the same day, and thus deviations between the samples can be attributed to the variation of the absorber thickness d_a. Samples with a different GGI on the other hand were produced over the span of a year, and their opto-electrical differences should be interpreted with more caution.

Samples with 32 cells were produced in the projects for **papers II** and **IV** to achieve more reliable result**s**. Thereby, the CIGS layers of the passivated and reference samples with otherwise equal sample stack were co-evaporated in the same CIGS run. All CIGS layers for **paper II** (and **paper IV**) were co-evaporated on the same day. The aim of the research for **paper III** was to show in principle if thin unpatterned passivation layers can provide a sufficiently strong passivation effect without blocking the current and to evaluate the influence of Na. In this case, the samples were produced over few months. The measurement results indicate very different trends for the different Na supply methods but should not be over-interpreted to quantify a possible passivation effect.

1.5 Chemical bath deposition of CdS buffer layer

The CdS buffer layer is deposited by a standard chemical bath deposition process with a specific recipe developed in our lab. To avoid experimental variation caused by differences in oxidation of the CIGS surface, this process is done within minutes after unloading the BAK. The CBD bath contains an alkaline aqueous solution with 1.1 M ammonia as a complexing agent, 0.1 M thiourea as a sulfur precursor, and 0.003 M cadmium acetate as a cadmium source. The samples are immersed into a beaker containing the solution at room temperature. Thereafter, the beaker is immersed into a 60°C water bath and the solution is stirred for 15 s each minute. At the end of the process time of 8 min and 15 s, the samples are directly moved from the CBD beaker into

a beaker with clean DI water to stop the growth process, thoroughly rinsed under a flow of DI water and thereafter dried with a nitrogen gun. According to transmission electron microscopy (**paper IV**), the CdS is 55-60 nm thick.

CdS is the first of three layers that together form the electron contact, sometimes referred to as buffer/window layer stack. The task of the buffer/window layer stack is to transmit light to the absorber and to conduct electrons. Unfortunately, CdS has a relatively low band gap of 2.4 eV and parasitically absorbs light, but it also has advantages. The polycrystalline CdS covers the CIGS densely and the CIGS/CdS interface has a lower recombination rate, than the interface created by directly sputtering the i-ZnO or ZnO:Al onto the CIGS layer. Additionally, unwanted native oxides are removed by the ammonia in the CBD.

1.6 Sputtering the i-ZnO-ZnO:Al front contact

A von Ardenne CS600S radio frequency (RF) horizontal sputtering system deposits an intrinsic ZnO layer (i-ZnO) and an Al-doped ZnO (ZnO:Al) front contact in a single run. The substrates are stationary during deposition. The ceramic ZnO:Al$_2$O$_3$ target contains 1 or 2 weight percent of Al$_2$O$_3$ and all targets have a purity of 3N. The highly resistive i-ZnO layer has a typical thickness of 90 ± 10 nm and the thickness of the ZnO:Al front contact is about 200 ± 40 nm. The sheet resistance of the stack is 30 ± 10 Ω/square.

The sputtering of the window layer can only be done for one 5 cm x 5 cm sample per run and the process has been unstable from day to day, affecting the sheet resistance. Therefore, all samples in **papers II and IV** had their respective window layer sputtered within a few hours. The samples in **papers I and III** were produced over several months, so that the window layer could not be deposited on the same day for all samples. In **paper I** two samples were produced for every sample type (*GGI* and thickness) and all samples with the same value of the *GGI* had their window layer sputtered on the same day. Samples with different values of the GGI were however produced over several months. Therefore, I cannot completely exclude that some of the deviations in the measurement results between samples with different values of the *GGI* stem from unintentional deviations in the window layers.

The baseline recipes for these sputtering processes and the targets were changed several times during my work due to a creeping degradation of transparency and conductivity and due to target changes. No such changes were however made while processing the solar cells for a paper.

The i-ZnO layer's high resistance reduces electrical inhomogeneities over the area and reduces the influence of shunting defects and increases reproducibility but reduces the short-circuit current density J_{SC} only slightly. ZnO:Al is an n-doped transparent conducting oxide (TCO). It needs to have both a sufficiently high electron conductivity σ^e to transport electrons laterally

to the grid fingers and a large band gap and low free carrier absorption, i.e. a low free carrier concentration, to allow for high transmittance. Therefore, the electron mobility should be high. $\mu^e \approx 20$ cm^2/Vs for the baseline.

1.7 Electron-beam evaporation of the Ni/Al/Ni metal contact

The metal contacts are deposited by electron-beam evaporation of the metals through an aperture mask and consist of a Ni/Al/Ni stack. The first nickel layer improves the contact resistance of the metal contact to the ZnO:Al and prevents the Al from reacting with oxygen in the ZnO and thus from forming a layer of highly resistive Al_2O_3. The second layer protects the Al against oxidation in air. The contact consists of a contact pad that is contacted for electrical characterization and grid fingers that collect the current from the ZnO:Al. The metal contact reduces the series resistance of the cells and allows for thinning down the ZnO layer, but it shadows a part of the cell.

1.8 Cell definition

Solar cells are defined on the samples by mechanical scribing with a stylus or by photolithography assisted etching. Etching is used to avoid shunting along the scribed lines in ultra-thin devices. Such shunts are visible in both dark and light JV curves and thus most probably not related to the voltage and light dependent current collection described in chapter 3.3. The etching removes all window layers along a closed line around the individual cells, the mechanical scribing also removes the CIGS layer. In some cases, the samples with rear surface passivation had to be mechanically scribed several times, to remove the CIGS from the oxide layer. Baseline cells have a size of 0.5 cm^2.

2 Solar cell device physics

2.1 What drives a solar cell?

The temperature difference between the surface of the sun and the solar cell is the driving force of any solar cell[22]. Correspondingly, solar cells are a thermodynamic energy converter that converts solar radiation first into chemical energy and then the chemical energy into electrical energy[23]. Nevertheless, they are traditionally described based on semiconductor device physics.

The basic differential equations[22,23] that govern all semiconductor-based solar cell devices, are well known. They consist of the Poisson equation

$$\nabla(\varepsilon\nabla\varphi) = -\rho \tag{1}$$

the continuity equations for electron and holes

$$\frac{\partial n}{\partial t} = \frac{1}{q}\nabla_{\overrightarrow{J^e}} + G^e - R^e \tag{2}$$

$$\frac{\partial p}{\partial t} = -\frac{1}{q}\nabla_{\overrightarrow{J^h}} + G^h - R^h \tag{3}$$

and the equations governing the hole and electron current densities, respectively[22].

$$\overrightarrow{J^e} = \mu^e\, n\nabla\varepsilon_{FC} \tag{4}$$

$$\overrightarrow{J^h} = \mu^h\, p\nabla\varepsilon_{FV} \tag{5}$$

In these equations ε is the dielectric constant, φ the electrical potential related to the local vacuum level, ρ the space charge density, q the elemental charge and t time; G^e *and* G^h are the generation rates, R^e and R^h the recombination rates and μ^e and μ^h the mobilities for electrons and holes, respectively; n and p are the free electron and hole concentrations and ε_{FC} and ε_{FV} the quasi-Fermi levels for the electrons in the conduction band and valence band, respectively.

The Maxwell-Boltzmann approximation of the carrier concentrations can be used, if the semiconductors are non-degenerate, which is in general the case for CIGS solar cells in the dark and in unconcentrated sunlight.

$$n = N_C e^{\frac{\varepsilon_{FC}-E_C}{kT}} \qquad (6)$$

$$p = N_V e^{\frac{E_V-\varepsilon_{FV}}{kT}} \qquad (7)$$

Here, E_C and E_V are the energies of the conduction and the valence band edge, and N_C and N_V the effective density of states in the conduction and the valence band, respectively. In the dark, the product of $n = n_0$ and $p = p_0$ is equal to the square of the intrinsic carrier concentration n_i independently of the doping (law of mass action).

$$n_i^2 = n_0 p_0 = N_C N_V e^{\frac{-E_G}{kT}} \qquad (8)$$

E_G is the semiconductor's band gap. Already at room temperature and in the dark – often referred to as under equilibrium conditions - all shallow donors and acceptors are ionized so that the equilibrium electron concentration is equal to the net-donor concentration $n_0 \approx N_D$ and $p_0 \approx n_i^2/N_D$ if $N_D > 0$ (n-type semiconductor) and the equilibrium hole concentration is equal to the net-acceptor concentration $p_0 \approx N_A$ and $n_0 \approx n_i^2/N_A$ if $N_A > 0$ (p-type semiconductor).

The gradients of the quasi-Fermi levels can then be rewritten as the sum of a drift and a diffusion component.

$$\nabla\varepsilon_{FV} = -kT\frac{1}{n_0}\nabla n_0 + kT\frac{1}{n}\nabla n = -q\nabla\varphi + \nabla\mu \qquad (9)$$

The first term is the gradient of the electrical potential φ, and the second term is the gradient of the chemical potential μ. The electrical potential depends on the equilibrium carrier density and thus not on excitation, while the chemical potential depends on the total carrier concentration and is the potential acting on the access carrier concentration under illumination[24].

Equation 1-5 are in the general case highly non-linear, cannot be solved analytically and their mathematics is hard to understand intuitively. They can however be solved numerically. To solve them for every point in the different semiconductor layers of the solar cell, the boundary conditions of the simulation domain are to be specified. Numerical modeling typically involves over 100 parameters, that need to be measured or estimated, and the influence of single parameters on different effects is a-priori unknown[25].

While numerical modeling has enabled researchers to understand and predict experimental results, it can still be hard to translate simulation results into a picture of the underlying physics[23]. In contrast, analytical models enable a verbal description of the physical processes and are conductive for yet another layer of comprehension called "ingenuity", "art", "deeper understanding"[26], but require simplifications that are not always justifiable. Only under specific conditions and assumptions, can the non-linear differential equations 1-6 be brought into a linear form and be analytically solved[18,25,27–33].

To my surprise, solar cell researchers do not agree on how solar cells work. P. and U. Würfel, A., Cuevas et al. and S. Smit [20,23,24,26,30,34,35] amongst others, argue that parts of the common physical picture(s) of solar cells are thermodynamically incorrect, incoherent or naïve and suggest models based on thermodynamics. I do not intend to provide the reader with more than those scraps of information that are needed to understand the gist of their arguments, but I recommend reading those works. I advise to start with [36], where the function of a pn-diode as rectifier, light emitter and solar cell is explained in a very intuitive way. In this context, it also becomes obvious that an excellent solar cell (with a high V_{OC}) must also be an excellent light emitting diode with excellent external and internal luminescence efficiencies and an excellent photon mirror at the rear surface[8]. In their text book "Physics of solar cells" [23] P. and U. Würfel present the most comprehensive elaboration of solar cells as thermodynamic energy converters. The paper, "Charge carrier separation in solar cells"[30], should not be missed, as it addresses the little criticism that has been levelled against this interpretation. Finally, S. Smit has expanded on P. Würfel's thermodynamic arguments and introduced a solar cell model based on non-equilibrium thermodynamics[26].

Although above equations clearly state that J^e and J^h are driven by gradients in quasi-Fermi levels, photocurrent transport and charge separation in solar cells with pn-junctions are conventionally described as being driven by the electric field established over the pn-junction (see *Figure 2*). P. Würfel argues that the notion that built-in electrical fields (over the pn-junction and also over the unipolar junction at the rear contact) drive the photocurrent density J_{ph} is physically wrong, as the electrostatic force is conservative and energy would be dissipated due the charge carrier's collisions with the lattice; the depletion region's capacitance would get discharged and the current flow would vanish after a dielectric relaxation time. According to him, "a gradient of the electrical potential is only maintained because it is compensated by the gradient of the chemical potential. Otherwise, the pn-junction would be discharged in the same way as a capacitor."[23] Neither is the electrical field's ability to dissipate energy the driving force. Only free energy F, which is the part of the energy E of an electron hole pair that is free of entropy, can be dissipated when electrons move from the p to the n-side. Ions within a battery also move against the electrical force, because the gradient of their chemical

30

potential overcompensates the gradient of their electrical potential as the charge currents need to fulfil the continuity equation. The gradient in the electrochemical potential is the ions' only driving force. It points into the same direction as the gradient of the chemical potential.

Furthermore, in many text books[37–39] J^h and J^e are split into diffusion and drift currents that flow simultaneously in different directions over the pn-junction. This description violates energy conservation, as these currents would dissipate energy even if the electrons and holes are in thermal and electrochemical equilibrium. Instead, the electrical and chemical force need to first be summed up to give the electro-chemical force, i.e. the gradient in the quasi-Fermi levels just as in equations 4 and 5. Two kinds of electrons, that either only are subject to the electrical field or only to the gradient in the chemical potential, do not exist, just as two different kinds of molecules that either get pushed down due to the gravitational force or pushed upwards due to the pressure gradient do not exist in air. The forces need to be added up first to a total force acting on every molecule instead. In air, two simultaneous upwards and downwards currents of molecules do not exist.
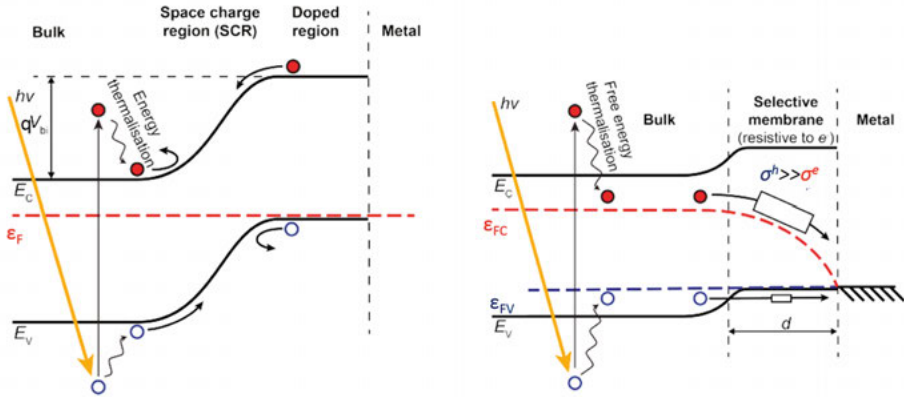

Figure 2. Conventional (left) and selective membrane model (right) of a hole contact based on a pn-homojunction. The conventional picture emphasizes the built-in electrical potential V_{bi} and the force that the electrical field in the space charge region exerts on the charge carriers. Furthermore, the solar cell is depicted in equilibrium although light shines on it, as the Fermi level ε_F is not split into two quasi-Fermi levels. Finally, the thermalization loss of an electron-pair on the left is drawn as the loss of internal energy. On the right-hand side, electron-hole pairs thermalize to the difference in quasi-Fermi levels $F=\varepsilon_{FC}-\varepsilon_{FV}$. The gradients of the quasi-Fermi levels transport the charge carriers. As the gradient for holes towards the hole contact is much smaller than the gradient for electrons, the electron transport towards the hole contact needs to be mitigated by a very low electron conductivity σ^e and hole transport needs to be supported by a very high hole conductivity σ^h. (Adopted from [26]).

Finally, the thermodynamic view of solar cells emphasizes the quasi-Fermi levels that represent the free energy of the electrons and holes, as only free

energy is available to generate work. Therefore, thermalization should be seen as free energy thermalization instead of internal energy thermalization as shown in *Figure 2*.

2.2 The carrier-selective membrane model
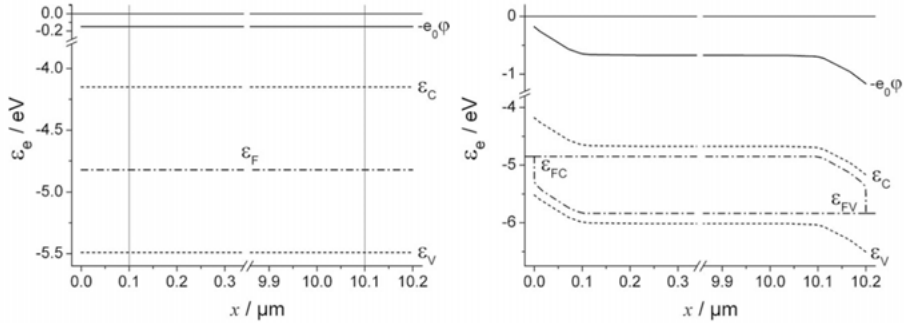
Figure 3. Band diagram of a mobility-junction solar cell in the dark and without applied voltage (left) and under illumination and at the voltage at the maximum power point V_{mp} (right) with Fermi level ε_F, quasi-Fermi energy levels ε_{FC} and ε_{FV} for electrons in the conduction band and the valence band, respectively, electrical potential energy $-e_0\varphi$ and conduction and valence band edge ε_C and ε_V. There is no built-in electric field as none of the layers is doped and they have the same band gap and the same electron affinity. The electron contact is located at $x = 0$ and the hole contact at $x = 10.2$ µm. The vertical lines at $x = 0.1$ µm and $x = 10.1$ µm are a guide to the eyes and depict the interfaces between absorber and selective transport layers. (Source: [30])

If the charge transport to the contact is selective, solar cells that either lack a built-in electrical field in the dark and/or have an electrical field directed against the carrier flow at the maximum power point (see *Figure 3*) reach the Shockley-Queisser conversion limit in simulations based on equations 1-6 [30]. As the force stemming from the gradients in the Fermi level is not selective (i.e. it cannot facilitate charge separation), this selectivity needs to be achieved by a strong asymmetry in the conductivities of electrons $\sigma^e(x) = q \cdot \mu^e(x) \cdot n(x)$ and holes $\sigma^h(x) = q \cdot \mu^h(x) \cdot p(x)$ in two regions of the device (see *Figure 2*). A selective region acts as a current transport layer towards the contact for one type of charge, but strongly reduces the transport of the other charge. It ensure that the least resistive recombination pathway for carriers is located at the correct contact and that they only lose minimal free energy/generate minimal entropy on the way to that contact. The differences in conductivity need to be so large, that the majority carrier current towards the contact is much larger than the minority carrier current, even though the

gradient in the majority carrier quasi-Fermi level is much smaller than the gradient in the minority carrier quasi-Fermi level (see *Figure 2*).

The entropy generation S due to carrier transport into the hole contact is proportional to various electrical quantities in the following way[26]

$$S \propto -\varepsilon'_{FC} J^e + \varepsilon'_{FV} J^h \propto \sigma^e (\varepsilon'_{FC})^2 + \sigma^h (\varepsilon'_{FV})^2 \propto \frac{J^{e2}}{\sigma^e} + \frac{J^{h2}}{\sigma^h} \qquad (10)$$

According to equation 10, the transport losses can be split into transport losses for the hole and for the electron current towards the contact. To reduce entropy generation from hole transport, an upwards bending $\Delta\varepsilon_{FV}$ or a small σ^h need to be avoided as J^h is necessarily large. $\Delta\varepsilon_{FV}$ reduces qV_{OC} approximately linearly (see chapter 2.4)

$$qV_{OC} \approx (\varepsilon_{FC} - \varepsilon_{FV})|_{bulk,V_{OC}} - \Delta\varepsilon_{FV}|_{V_{OC}} \qquad (11)$$

The large gradient in ε_{FC} cannot be avoided, because in the absorber bulk a large quasi-Fermi level splitting is required to generate useful work and in the metallic contact the quasi-Fermi level splitting is zero. Therefore, in an ideally selective membrane $J^e = 0$ and the only way to reduce entropy generation from minority carrier transport is to minimize σ^e. If electrons are generated in a selective hole-conducting membrane, they will not be transported to the absorber bulk but recombine at the hole contact, as the resistance towards the hole contact is lower than the resistance towards the electron contact. Minority carrier transport to and recombination at the hole contact mostly affects the quasi-Fermi level splitting (see chapter 2.4). Therefore, light absorption and free carrier generation should be avoided in the selective membranes.

According to the selective-membrane model, pn-junctions work as solar cells, because the doping provides a large density of majority carriers and a small density of minority carriers and thus a high conductivity for majority carriers and a low conductivity for minority carriers in the p- and n-doped regions. The p- and n-doped regions however select poorly for the respective majority charge carriers, as illumination enhances the minority carrier concentrations by a much larger factor (about 12 orders of magnitude) than the majority carrier concentrations. Thus, majority carrier concentrations in the dark must be at least as large as the additional concentrations generated by illumination in the selective charge transport regions. N_D and N_A must match the potential difference φ^n-φ^p in the dark between the n- and p-doped areas to the expected chemical energy per electron-hole pair during illumination. This condition can be expressed as (ref. [23]):

$$kT \ln \frac{N_D \cdot N_A}{n_i^2} = q(\varphi^n - \varphi^p) \geq \varepsilon_{FC} - \varepsilon_{FV} = kT \ln \frac{p \cdot n}{n_i^2} \qquad (12)$$
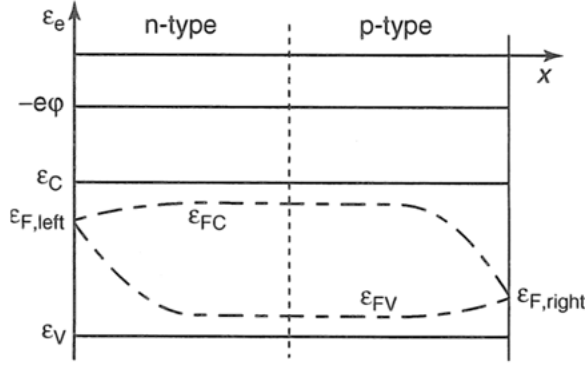
Figure 4. Band diagram with quasi-Fermi-energy levels ε_{FC} and ε_{FV} for electrons in the conduction band and the valence band, respectively, electrical potential energy $e\varphi$ and conduction and valence band edge ε_C and ε_V in a homogenously illuminated pn-structure under open-circuit conditions. (Source: [23])

For the pn-homojunction based solar cell in *Figure 4*, the doping of the p- and n-sides is chosen so that φ is constant under the applied illumination and open-circuit conditions. The open-circuit voltage V_{OC} is equal to the difference in quasi-Fermi levels on the left and right side, $\varepsilon_{F,left}$-$\varepsilon_{F,right}$. It is not equal to the difference in electrical potential at the left and right side, which is zero in this case. At the contact, recombination pins the (quasi-)Fermi levels under illumination to the Fermi level in the dark. Therefore, the split of the quasi-Fermi levels $F=\varepsilon_{FC}$ - $\varepsilon_{FV}|_{bulk}$ in the center is larger, than $qV_{OC} = \varepsilon_{F,left}$-$\varepsilon_{F,right}$. For the continuity equations to hold, the gradient toward the contacts in quasi-Fermi level for the majority carriers is smaller than the gradient in quasi-Fermi level for minority carriers. In the carrier selective regions, a strong bending of the minority carrier quasi-Fermi level and thus a decrease in the quasi-Fermi level splitting in the semiconductor is necessary for a decrease of the minority carrier conductivity.

Unfortunately, a low concentration of minority carriers reduces the voltage at the maximum power point. Only high concentrations of both majority and minority carriers lead to a large split of the quasi-Fermi levels (see equation 12). A high voltage V_{mp} and high current density J_{mp} at the maximum power point can thus not be achieved in a solar cell with single pn-homojunction. Only if the recombination rate of the minority carriers at the contacts or the contact area is strongly reduced as in partial contacts, can they reach the Shockley-Queisser limit according to simulations[30].

Conversely, for solar cells based on pn-heterojunctions, highly asymmetric conductivities can be caused by highly asymmetric carrier mobilities, instead of highly asymmetric carrier concentrations. The selective transport layer that faces the sun is called window layer in inorganic thin film solar cells (compare chapter 1.6).

Although the fundamental equations governing solar cells are undisputed and the works criticizing the traditional description are available and accessible, many solar cell researchers are only familiar with the traditional descriptions and not with their criticism. Considering the citations in the peer-reviewed literature, the engagement with the criticism seems to be quite low. However, some parts of the silicon solar cell research community focusing on selective and passivating contacts and parts of the organic and dye-sensitized solar cell research community have formulated their models considering the criticism, as citations show[26,40–49].

The doping concentrations and therefore d_w/d_a ratio vary strongly between different types of solar cells. In both organic solar cells, dye sensitized solar cells and crystalline silicon solar cells, w_a in the dark and without applied bias is very small compared to d_a (and even smaller at forward bias and under light). Therefore, the electrical field only plays a minor role in the charge carrier separation regardless of the model. On the other hand, for typical inorganic thin film solar cells, the d_w/d_a ratio varies from around 1/10 in CIGS solar cells to 1 in fully depleted devices like amorphous, microcrystalline Si solar cells [50] or pin solar cells [30]. Therefore, for inorganic thin film solar cells a larger shift in the understanding of the physics is required and a discussion of the underlying physics might advance the understanding of these solar cells considerably.

For the thin film heterojunction solar cell under illumination and short circuit conditions in *Figure 5*, the gradients of the quasi-Fermi levels in the absorber space charge region are large and indeed similar to the gradients in E_C, E_V and the electrical potential, which is about equal to the electrical potential energy in equilibrium $-q\varphi \approx q\varphi_0$. Therefore, drift dominates strongly over diffusion and *EQE, AQE* and *JV* data recorded at negative bias or short-circuit can be crudely discussed by assuming that all minority charge carriers reaching the space charge region are collected (as I have done in chapter 2.3.2 and 3.1 and for the negatively biased junction at the rear contact in chapter 5.4.2). In stark contrast, under open-circuit conditions, the (positive) gradients of E_C, E_V and $-q\varphi$ and the width of the space charge region d_w are strongly reduced compared to the equilibrium condition, and the quasi-Fermi levels have a slightly negative gradient, in the opposite direction compared to the electrical field. The band diagram at the maximum power point (not depicted) is very similar to the one at open circuit, with approximately horizontal quasi-Fermi levels in the diminished space charge region. Thus, when discussing the solar cell at strong forward bias, or the efficiency η or J_{mp}, the electrical field should in general not be considered.
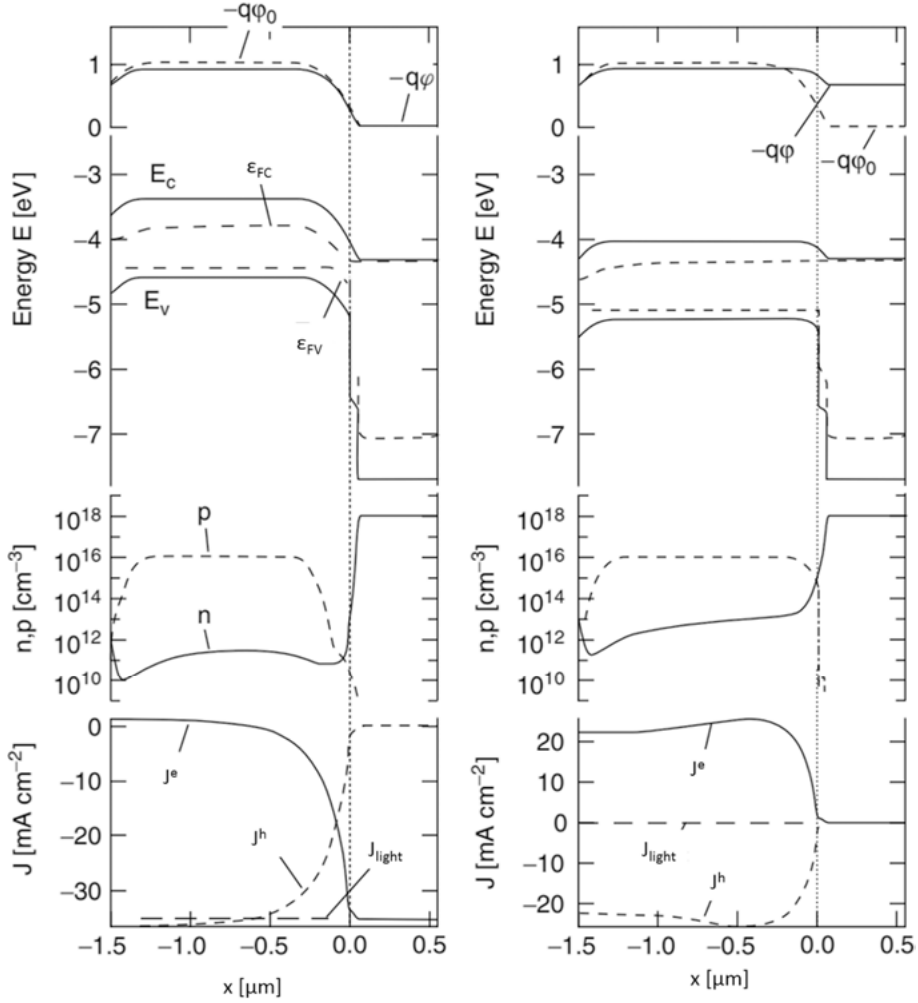
Figure 5. Band diagram, carrier densities *p* and *n* and currents J^e, J^h and J_{light} in a thin-film heterojunction solar cell with an absorber/buffer/window layer stack under illumination at short circuit (left) and at open circuit (right). $q\varphi$ denotes the electrical potential energy under the applied conditions, $q\varphi_0$ at equilibrium (i.e. in the dark and without applied voltage). (Source: [18])

Most articles in the CIGS solar cell field are based more or less explicitly on the traditional interpretation, and a language describing CIGS solar cells regarding the above-mentioned criticism has not been established to my best knowledge. Some researchers have tried to unite the various interpretations, but have not directly contradicted P. Würfel's claim that parts of traditional interpretations are wrong[22,50–52] and/or Würfel has replied to their criticism[30]. The traditional interpretations are still taught to students without mentioning the on-going discussion and alternative interpretation, nearly a decade after the publication of Würfel's "The physics of solar cells" in

English. Hopefully, the fact that P. Würfel got awarded the Becquerel prize for outstanding merits in photovoltaics in 2018, will increase the visibility of the different models and interpretations and the debates surrounding them.

In this thesis, **papers I, II, and III** are based on the conventional solar cell models and their interpretations. Only, when I read several papers by Cuevas et al. [9,20,24], did I conclude that I could not avoid the topic if I wanted to explain rear surface passivation to my best knowledge. The electrical field itself is not responsible for the rear surface passivation, but asymmetric charge carrier densities held in place by the electrical field are (see chapter 2.4). Therefore, I motivated the usage of rear surface passivation with help of the newly found understanding in paper **IV**. I hope that my thesis exemplifies how we develop our understanding and make progress, both personally and in science.

2.3 Current-density voltage characteristics of a solar cell

The interfaces between the different layers in a solar cell stack form pn-homo- or heterojunctions or semiconductor-metal junctions. Researchers devoted to the front contact study the pn-heterojunctions between the CIGS layer and the buffer layer, which is the main junction in CIGS solar cells, and the heterojunction between the buffer layer and the window layers. At the rear contact, there is a heterojunction between the CIGS layer and $MoSe_2$ layer and a semiconductor-metal junction between the $MoSe_2$ and the Mo, if the solar cells are processed according to the baseline. If an ultra-thin oxide passivation layer is added on top of the Mo, a metal-insulator-semiconductor (MIS) contact is formed. Such a MIS contact might have been formed for solar cells with an unpattterned ultra-thin oxide layer between the semiconductor absorber and the metal contact in **paper III and IV** (see chapter 5.2.2).

2.3.1 An ideal solar cell

To be able to describe solar cells analytically, to understand how they work in principle and to quantify losses, assumptions that simplify the equations governing solar cells behavior are made. The solar cells described by these simplified models are often called "ideal solar cells", but in which way they are ideal differs from author to author, and model to model. The following chapter uses the assumptions and paraphrases the derivation of the diode equation presented in [23]. In this ideal solar cell model, only one junction and only radiative recombination and generation is considered, i.e. defect related recombination and generation, including surface recombination and generation are not considered. The absorber layer is thus assumed to be thicker

than the minority carrier diffusion length . All other assumptions made in this model will be mentioned at the appropriate places throughout this chapter.

As a pn-junction rectifies the current, its current-voltage characteristics can be described as those of a diode. If the device is biased in reverse, i.e. positively at the n-side relative to the p-side, only thermally generated minority charge carriers that have not radiatively recombined before reaching the region, where they are majority carriers, can flow over the junction. Thus, only minority carriers generated within a diffusion length L_r^e or L_r^h for radiative recombination from the junction contribute to the current across the junction. At forward bias, both electrons and holes move from the regions where they are majority carriers into the oppositely doped regions, where they are minority carriers. There, they recombine radiatively in average after one minority carrier diffusion length, again L_r^e or L_r^h. In the rest of the p and n-regions, the minority carrier concentration is much smaller than the majority carrier concentration and the current is carried only by the majority carriers. This assumption is valid in the case of weak excitation, i.e. if the concentration of additional minority carriers from light bias and voltage bias stays smaller than the concentration of minority carriers due to the doping. For both forward and reverse direction, the charge current is transferred from the minority charge carriers to the majority carriers within a diffusion length on both sides of the pn-junction. The charge current density under illumination $J_{light}=J^e+J^h$ can then be calculated by integrating only over the divergence of one charge current density component considering that $J^h = 0$ for $x < -L_r^h$, and $J^h = J_{light}$ for $x<L_r^h$. (see *Figure 6*). As the absorber layer is intrinsically p-doped in CIGS solar cells, I have chosen to integrate over the hole current density.

$$J_{light} = - \int_{-L_r^h}^{L_r^e} div \ J^h dx \qquad (13)$$

Under steady-state conditions the continuity equation for holes (equation 3) can be simplified to

$$div J^h = q(G_r^h - R_r^h) \qquad (14)$$

Where G_r^h and R_r^h are the generation and the recombination rates for holes, respectively. G_r^h under illumination can be split into a generation rate $G_{0,r}^h$ due to the thermal background radiation in the dark and G_{ph}^h due to illumination.

$$G_r^h = G_{0,r}^h + G_{ph}^h \qquad (15)$$

R_r^h is proportional to the concentration of both holes and electrons with a proportionality constant β

$$R_r^h = \beta np = R_{0,r}^h \frac{n \cdot p}{n_i^2} = R_{0,r}^h e^{\frac{\varepsilon_{FC} - \varepsilon_{FV}}{kT}}. \tag{16}$$
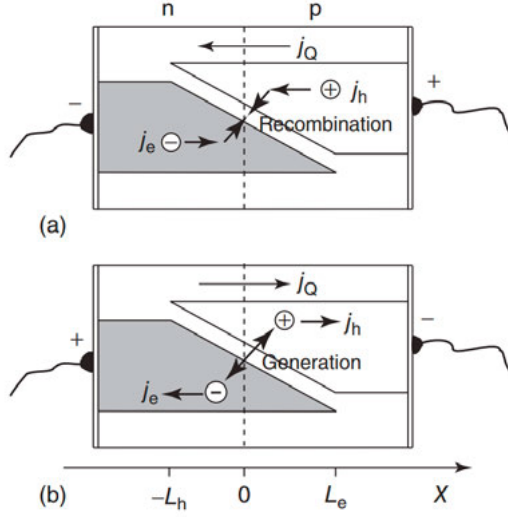

Figure 6. Electron and hole currents in a pn-junction. (a) For a negative bias of the n-region with respect to the p-region, i.e. in the forward direction, electrons and holes flow towards the pn-junction, where they recombine. (b) At reverse bias, i.e. for a positive bias at the n-region compared to the p-region, electrons and holes are produced in the pn-junction and flow away from it. (Source: [23])

Considering finally that

$$G_{0,r}^h = R_{0,r}^h \tag{17}$$

we arrive at

$$div\, J_h = q\left(G_{0,r}^h + G_{ph}^h - R_{0,r}^h \frac{n \cdot p}{n_i^2}\right) = q\left(G_0^h\left(1 - \frac{n \cdot p}{n_i^2}\right) + G_{ph}^h\right) =$$

$$= q\left(G_{0,r}^h\left(1 - e^{\frac{\varepsilon_{FC} - \varepsilon_{FV}}{kT}}\right) + G_{ph}^h\right). \tag{18}$$

$$U_r^h = R_r^h - G_{0,r}^h = R_{0,r}^h\left(\frac{n \cdot p}{n_i^2} - 1\right) = R_{0,r}^h u \tag{19}$$

is often referred to as net-recombination rate.

$$u = \frac{n \cdot p}{n_i^2} - 1 = e^{\frac{\varepsilon_{FC} - \varepsilon_{FV}}{kT}} - 1 \tag{20}$$

is the normalized excess np-product. When inserting equation 18 and 20 into equation 13, the current density under illumination becomes

$$J_{light} = q \int_{-L_r^h}^{L_r^e} \left(G_{0,r}^h \left(e^{\frac{\varepsilon_{FC} - \varepsilon_{FV}}{kT}} - 1 \right) - G_{ph}^h \right) dx =$$

$$= q \int_{-L_r^h}^{L_r^e} \left(G_{0,r}^h \, u - G_{ph}^h \right) dx \qquad (21)$$

The current through a pn-junction is usually not limited by the transport resistance, but by the reactions of holes, electrons, photons and phonons. Therefore, no more electrons and holes can flow away from the junction than are produced there, and no more charge carriers can flow towards the junction than can disappear there due to recombination. Thus, the difference between the quasi-Fermi levels can be assumed to be constant for $-L_r^h < x < L_e^h$ and equal to qV. This assumption makes the continuity equation linear, but it is not always an adequate approximation (see chapter 3.3). Then, the integrand in equation 18 is constant over the range of the integration and the integration is simplified to

$$J_{light} = q G_{0,r}^h \left(L_r^h + L_r^e \right) \left(e^{\frac{qV}{kT}} - 1 \right) - q \int_{-L_r^h}^{L_r^e} G_{ph}^h \, dx =$$

$$= J_{0,r} \left(e^{\frac{qV}{kT}} - 1 \right) - J_{SC} = J_{dark} - J_{SC}. \qquad (22)$$

J_{SC} is the current density that flows at external short circuit *(V = 0)* and J_{dark} is the current density over the junction in the dark. That J_{SC} can be simply added to J_{dark} is called shifting approximation. If no current flows, the voltage over the pn-junction is the open-circuit voltage

$$V_{OC} = \frac{kT}{q} \ln \left(1 - \frac{J_{SC}}{J_{0,r}} \right) \qquad (23)$$

In the dark $G_{ph}^h = 0$ and we find for large negative voltage bias a small current density $J_{0,r}$, referred to as reverse or recombination current density or dark saturation current density or recombination current density pre-factor[24]. In an ideal solar cell in the dark at room temperature, this current density is only produced by the absorption of 300 K background radiation within a radiative diffusion length from the junction.

$$J_{0,r} = qG_{0,r}^h(L_r^h + L_r^e) = q\beta n_i^2(L_r^h + L_r^e) = q\beta N_C N_V e^{\frac{-E_G}{kT}}(L_r^h + L_r^e) \quad (24)$$

In real pn-junctions non-radiative generation rates (see chapter 2.3.2) are much larger than radiative generation rates. These generation (and recombination) rates can be expressed in terms of minority charge carrier lifetimes

$$G_0^{h,e} = R_0^{h,e} = \frac{n_p}{\tau_e} = \frac{p_n}{\tau_h} = \frac{n_i^2}{N_A \tau_e} = \frac{n_i^2}{N_D \tau_h} \quad (25)$$

Here, n_p is the electron concentration in the p-side and p_n is the hole concentration in the n-side. Using the relationship

$$\tau = \frac{L^2}{D} \quad (26)$$

between the minority carrier lifetime τ, the minority carrier diffusion length $L^{h/e}$ and the diffusion coefficient D, the reverse saturation current density can be rewritten as

$$J_0 = qn_i^2\left(\frac{D^e}{n_A L^e} + \frac{D^h}{n_D L^h}\right) = q\, N_C N_V e^{\frac{-E_G}{kT}}\left(\frac{D^e}{n_A L^e} + \frac{D^h}{n_D L^h}\right) \quad (27)$$

As seen from equation 23, a high J_0 reduces the V_{OC}.

Another assumption for this ideal solar cell is, that only photons absorbed within L^e in the p-side and L^h in the n-side of the pn-junction can contribute to J_{SC}. (The collection function η_C as defined in chapter 2.3.2 is equal to 1 within a distance L^e and L^h from the junction and equal to 0 outside.) Assuming that the n-layer faces the sunlight, the pn-junction needs to lie no further than L^h from the surface. In the following, the n-layer is assumed to be very thin, so that absorption in it can be neglected, and it is called the window layer. In this constellation, the p-layer is called the absorber layer. A photon density spectrum dj_γ (λ, $x = 0$) incident on the absorber at $x=0$ generates the following differential generation rate in the absorber

$$dG_{ph} = (1 - R(\lambda))\alpha_a(\lambda)e^{-\alpha_a(\lambda)x}\frac{dj_\gamma(\lambda, x = 0)}{d\lambda}d\lambda \quad (28)$$

Here, α_a is the absorber's absorption coefficient and R the total reflectance of the solar cell. J_{SC} is equal to the generation current density J_{gen} generated within a diffusion length from the junction.

$$dJ_{SC} = q \int_0^{L^e} dG_{ph}^h dx =$$

$$= q\big(1 - R(\lambda)\big)\alpha_a(\lambda) \int_0^{L^e} e^{-\alpha_a(\lambda)x} dx \frac{dj_\gamma(\lambda, x = 0)}{d\lambda} d\lambda =$$

$$= q\big(1 - R(\lambda)\big)\big(1 - e^{\alpha_a(\lambda)L^e}\big) \frac{dj_\gamma(\lambda, x = 0)}{d\lambda} d\lambda =$$

$$= q \cdot A_a(\lambda, L^e) \frac{dj_\gamma(\lambda, x = 0)}{d\lambda} d\lambda \qquad (29)$$

Here,

$$A_a(\lambda, L^e) = \big(1 - R(\lambda)\big)\big(1 - e^{\alpha_a(\lambda)L^e}\big) \qquad (30)$$

is the absorptance of the absorber layer within L^e (compare to the equations in chapter 3.5). If L^e is longer than the thickness of the absorber layer d_a, d_a is to be used instead of L^e, if the rear surface is perfectly passivated to prevent the electrons from reaching the rear surface and recombining there. Otherwise not all generated minority carriers are collected and equation 29 is not valid. Rear surface passivation for CIGS solar cells has become more urgent, as both L^e has improved in recent years and the aim is to decrease d_a (see chapter 2.4). The J_{SC} originates from the photons absorbed within the shorter of the two lengths, d_a or L^e. For $L^e < d_a$

$$J_{SC} = q \cdot \int_0^\infty A_a(\lambda, L^e) \frac{dj_\gamma(\lambda, x = 0)}{d\lambda} d\lambda \qquad (31)$$

Even though equations 22-27 are in principle equal to the equations found in the conventional literature on semiconductor device physics, the exponential dependence of the current on the voltage is not caused by the potential barrier between the n- and p-sides in above derivation. Here, the majority carriers diffusing towards the junction at forward bias do not need to surmount a potential barrier (as for example in [37,39,53]). Instead, the exponential rise of the forward current is caused by the dependence of the recombination rate on the carrier concentrations, which in turn depends on the voltage and differs for different recombination mechanisms[18,23] (see chapter 2.3.2).

2.3.2 A more general solar cell

This chapter is based on [18,23] and J. Malmström's excellent PhD thesis[54], as those three works are to a good extent compatible. In a real solar cell several types of recombination processes occur in parallel, each carrying a part of the

current. Although those currents are determined by recombination processes, they are commonly referred to as diode currents and not recombination currents, as recombination via defects also reduces the J_{ph}[18]. Thus, the term "diode model" refers to the expression for the voltage-dependency of the current for a recombination process[54]. Solar cells are often described by several diodes in parallel and the diode current density components are summed up.

$$J_{diode} = \sum_i J_{diode,i} \qquad (32)$$

It can be shown that any contribution to the total diode current density can be expressed as [18]

$$J_{diode,i} = J_{0,i}\left(e^{\frac{qV}{A_i kT}} - 1\right) \qquad (33)$$

with

$$J_{0,i} = J_{00,i} e^{\frac{-E_{a,i}}{A_i kT}} \qquad (34)$$

A_i is the ideality factor of the recombination process i, $E_{a,i}$ the activation energy and $J_{00,i}$ the reference current density, which is only weakly temperature dependent. Which component is dominating the J_{diode} at which voltage and temperature is determined by A_i and $J_{0,i}$. According to equation 17, 19 and 20 $A_i = 1$ and $E_{a,i} = E_G$ for radiative recombination, but $A_i = 2$ for example for Shockley-Read-Hall recombination via a mid-dap defect in the space charge region.

Recombination processes can be categorized in two different ways: according to the recombination mechanism and according to the path, where the recombination takes place (space charge region, quasi neutral region, rear surface, front contact, interfaces). A concise overview of different recombination mechanisms in different regions of the solar cells is given in [55] and a comprehensive one is given in [18]. Recombination at the rear surface adds another summand $J_{diode,i}$ to J_{diode} (see chapter 2.4).

The different recombination paths are not only responsible for the diode current density, but also for the photocurrent density loss $J_{ph,loss}$ due to incomplete collection.

$$J_{rec}(j_\gamma) = J_{diode}(V, j_\gamma) + J_{ph,loss}(V, j_\gamma) \qquad (35)$$

The relative magnitude of different recombination paths is different for those two components of J_{rec}. In CIGS solar cells J_{diode} is usually dominated by the

interface path at the front contact, but $J_{ph,loss}$ is dominated by recombination in the absorber bulk[54].

Now, let us have a look at the photocurrent density J_{ph}, which shall be the current density generated by illumination and collected at the contacts in a solar cell with an absorber layer, a window layer and a rear contact. The probability that a photon gets absorbed in the absorber is expressed as the absorber's absorptance [23] or absorbance[18].

$$A_a(\lambda) = 1 - T_w(\lambda) - R(\lambda) - A_{par}(\lambda) \qquad (36)$$

Photons are not absorbed in the absorber, if they do not pass through the window layers ($T_w \neq 0$) due to absorption, if they get reflected from the solar cell ($R \neq 0$) or if they are parasitically absorbed at the rear contact $A_{par} \neq 0$. The current density generated by illumination in the absorber is then

$$J_{gen}(j_\gamma) = q \cdot \int_{\lambda_{g,w}}^{\lambda_{g,a}} \frac{dj_\gamma(\lambda, x = 0)}{d\lambda} A_a(\lambda) d\lambda \qquad (37)$$

By setting the limits of the integral to the wavelength corresponding to the band gap of the absorber $\lambda_{g,a}$, and of the window layer $\lambda_{g,w}$, the absorption of photons with energies lower than the absorber's band gap and higher than the window layer's band gap has been excluded. A position and wavelength dependent generation rate, here called spectral generation function, can be defined for $\lambda_{g,a} > \lambda > \lambda_{g,w}$,

$$dG_{ph}(\lambda, x, j_\gamma) = (1 - R(\lambda))\alpha_a(\lambda, x)e^{-\alpha_a(\lambda)x} \frac{dj_\gamma(\lambda, x = 0)}{d\lambda} d\lambda \qquad (38)$$

From dG_{ph} the local generation rate of charge carriers at the position x in the absorber can be calculated (see *Figure 7*):

$$G(x, j_\gamma) = \int_{\lambda_{g,w}}^{\lambda_{g,a}} \frac{dG_{ph}(\lambda, x, j_\gamma)}{d\lambda} d\lambda \qquad (39)$$

The spectral generation rate can also be normalized to the photon flux:

$$G_n(\lambda, x) = \frac{dG_{ph}(\lambda, x, j_\gamma)}{dj_\gamma(\lambda, x)} \qquad (40)$$
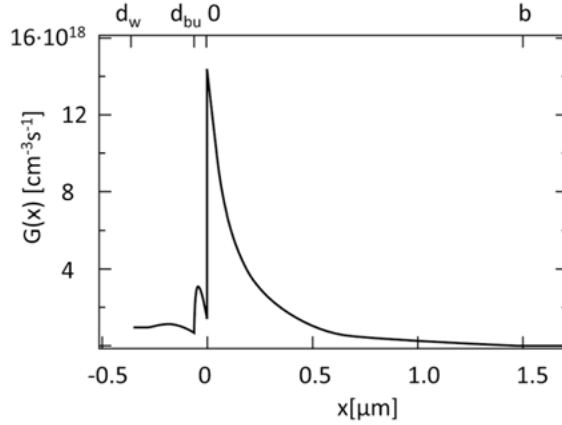
Figure 7. Optical generation function of a thin film heterojunction solar cell with a buffer-window layer stack thickness $d_w = 0.5$ µm and a buffer layer thickness $d_{bu} = 0.05$ µm. The decline of the generation rate in the absorber is supra-exponential. (Source: [18])

J_{gen} can be written in dependence on the spectral, local or normalized generation function or the absorptance.

$$J_{gen}(j_\gamma) = q \cdot \int_0^{d_a} \int_{\lambda_{g,w}}^{\lambda_{g,a}} \frac{dG_{ph}(\lambda, x, j_\gamma)}{d\lambda} d\lambda dx = q \int_0^{d_a} G(x, j_\gamma) dx =$$

$$= q \cdot \int_{\lambda_{g,w}}^{\lambda_{g,a}} \frac{dj_\gamma(\lambda, x = 0)}{d\lambda} \left(\int_0^{d_a} G_n(\lambda, x) dx \right) d\lambda =$$

$$= q \cdot \int_{\lambda_{g,w}}^{\lambda_{g,a}} \frac{dj_\gamma(\lambda, x = 0)}{d\lambda} A_a(\lambda) d\lambda \qquad (41)$$

A part of J_{gen} does not contribute to J_{ph} due to recombination losses.

$$J_{gen}(j_\gamma) = J_{ph}(V, j_\gamma) + J_{ph,loss}(V, j_\gamma) \qquad (42)$$

$J_{ph.loss}$ and J_{ph} can be voltage dependent. J_{ph} can be written as the convolution of the generation function $G(x, j_\gamma)$ and the collection function $\eta_C(x, V, j_\gamma)$, which is a unique function of the device[18]. $\eta_C(x, V, j_\gamma)$ gives the probability for a generated charge carrier to be collected at the contacts and to contribute to J_{ph}.

$$J_{ph}(V, j_\gamma) = q \int \eta_C(x, V, j_\gamma) G(x, j_\gamma) \, dx \qquad (43)$$

The integral here and in the rest of the chapter include the whole solar cell and not only the absorber. For example, a high interface recombination velocity at the contacts lowers $\eta_C(x,V,j_\gamma)$ locally. The $J_{ph,loss}$ is then

$$J_{ph,loss}(V,j_\gamma) = q \int \left(1 - \eta_C(x,V,j_\gamma)\right) G(x,j_\gamma)\, dx \qquad (44)$$

$\eta_C(x,V)$ is often assumed to be independent of the generation rate (and thereby independent of the photon flux density) and is traditionally expressed in dependence on the d_a, $w_a(V)$, the minority carrier diffusion length L_{QNR} in the quasi-neutral region and the effective rear surface recombination velocity S_{eff} (in cm/s). Its light dependence is neglected. Thereby, $\eta_C(V) = 1$ is assumed for the whole depletion region, which is a good approximation in the case for long minority carrier lifetimes in the depletion region and small interface recombination velocities at the front contact. If $L_{QNR} < d_a$, the collection function can be approximated by[18]

$$\eta_C(x,V) = e^{\frac{x+w_a(V)}{L_{QNR}}} \qquad (45)$$

This approximation is used in the derivation of the Gärtner formula[28] for the external quantum efficiency (see next chapter). The sum $w_a(V) + L_{QNR}$ is referred to as collection length.

If $L_{QNR} > d_a$, then recombination at the rear surface is to be considered, and the boundary condition at the rear surface is often set to

$$\left.\frac{d\eta_C(x)}{dx}\right|_{x=d_a} = \frac{S_{eff}}{D^e}\eta_C(x) \qquad (46)$$

with S_{eff} donating the effective recombination velocity at the rear surface. Solutions to equation 46 are found in *Figure 8*. $\eta_C(x,V)$ also acts on J_{diode} and limits it in the diffusion limit (i.e. when diffusion and not recombination and generation limit the current transport). The reciprocity theorem establishes a link between the collection function of J_{ph} under illumination and J_{diode} in the dark. If the continuity equation can be linearized by applying only small deviations of the minority carrier concentration from equilibrium the generalized reciprocity theorem can be used and the collection function can be written as[18,54]:

$$\eta_C(x,V,j_\gamma) = \frac{u(x)}{e^{\frac{qV}{kT}} - 1} = \frac{e^{\frac{\varepsilon_{FC}(x)-\varepsilon_{FV}(x)}{kT}} - 1}{e^{\frac{qV}{kT}} - 1} \approx \frac{\varepsilon_{FC}(x) - \varepsilon_{FV}(x)}{qV} \qquad (47)$$

Considering this equation, it becomes obvious that $\eta_C(x) = 1$ for $-L^h < x < L^e$ in the ideal solar cell in chapter 2.3.1.
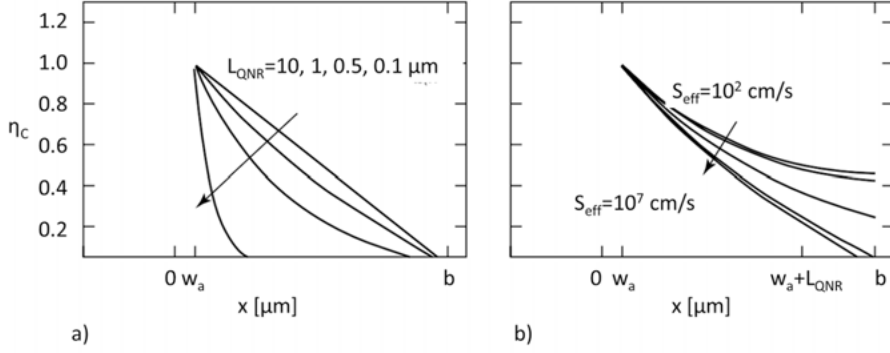
Figure 8. Collection function η_C in the absorber as a function of the position x. The diffusion constant for electrons was set to $D^e = 1$ cm/s and the absorber thickness d_a is 1.5 μm. The space charge region is located between 0 and w_a. In a) the diffusion length L_{QNR} is varied at a fixed $S_{eff} = 10^7$ cm/s. In b), the diffusion length is fixed at $L_{QNR} = 1$ μm and the effective recombination velocity S_{eff} at the rear surface is varied. The curves of $S_{eff} = 10^6$ and $S_{eff} = 10^7$ are not distinguishable in the graph. (Adapted from: [18])

Equation 44 is only valid, if the net recombination rate of the recombination path considered is linear in $u(x)$, i.e. if $A = 1$ and $U_r^h = R_0^h \, u(x)$. See equation 20 for a definition of the normalized carrier excess np-product. If $A \neq 1$, then $U_r^h = R(x) \cdot u(x)^{1/A(x)}$. The total current density for a solar cell under illumination can then be written in the following general way

$$J_{light}(V, j_\gamma) = J_{rec}(V, j_\gamma) - J_{gen}(j_\gamma) = -q \int \left(R(x, V, j_\gamma) - G(x, j_\gamma) \right) dx =$$
$$= J_{diode}(V, j_\gamma) - J_{ph}(V, j_\gamma) =$$
$$= -q \int \eta_C(x, V, j_\gamma) \left[R(x) \left(e^{\frac{qV}{A(x)kT}} - 1 \right) - G(x, j_\gamma) \right] dx \qquad (48)$$
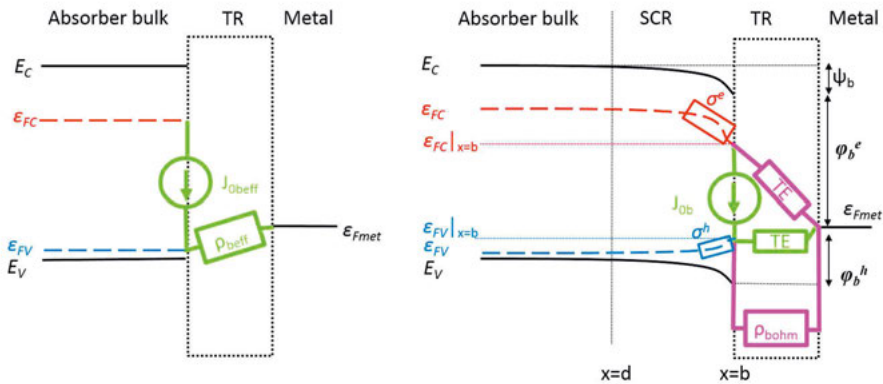
2.4 Electric models of the rear contact

Figure 9. Lumped diode model (left) and metal-insulator-semiconductor M(I)S model (right) suggested in [47]. The transition region TR between the absorber bulk and metal contact is hard to model in full detail. In different simplified empirical models, it is modelled with various numbers of input-parameters. To the basic M(I)S model (green) consisting of SRH recombination and thermionic emission TE of the majority carriers, an ohmic resistor and thermionic emission TE of the minority carriers can be added (pink). The lowered conductivities for hole and electron transport in the space charge region (SCR) can also be considered.

In a small, finite transition region between the semiconductor and the metal neither of them can be described as bulk. As many material parameters needed for modeling are not empirically accessible, it is hard to model numerically in full detail. The positions of the quasi-Fermi levels are also unknown in the transition region. Therefore, the current through the region is sometimes modelled with smaller numbers of empirical input-parameters in various empirical models.

These empirical electric models of the rear contact can be divided into two categories: Models in the first category describe effective carrier recombination at the rear surface in parallel to all other recombination paths (see chapter 2.3.1). Models in the second category neglect net recombination at the rear surface and use exchange currents into the contact.

For models in the first category, the total current over the contact interface consists only of majority carriers. The effective contact resistance for the total current is usually modelled by an ohmic resistor in series to the diode(s). This lumped diode model (see *Figure 9*) is commonly used to describe the rear surface in Si solar cells [35,40,42,45,48], but it can neither describe the temperature dependence of the contact resistance nor can it model kinks and roll-over behavior in the *JV* curve [47] as measured for CIGS solar cells at low temperatures or with a Na deficiency (see chapter 3.7).

J_{0b} representing the recombination flux of the blocked (minority) carriers and the contact resistivity ρ_C representing the interface resistance to the

collected majority carriers have been combined into the so-called "upper-limit" voltage at the maximum power point V_{UL} [35,45], which has been shown to be an important parameter for cell efficiency.

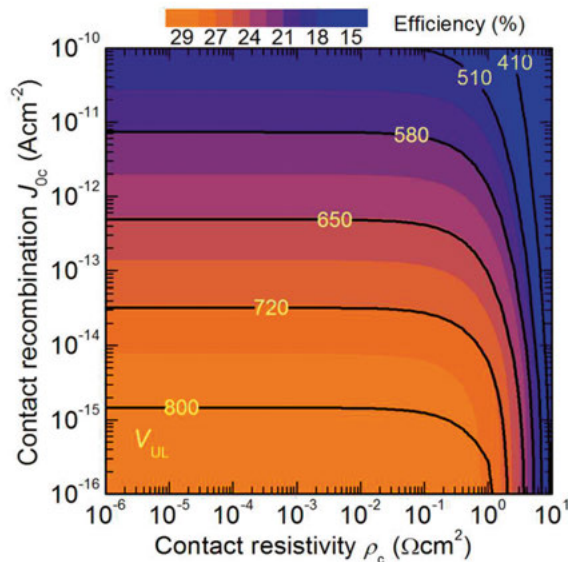$$V_{UL} = \frac{kT}{q} ln \left(\frac{J_{gen}}{J_{0b}}\right) - J_{gen}\rho_C \qquad (49)$$

Figure 10. Power conversion efficiency in dependence of $J_{0b} = J_{0c}$ and ρ_C as simulated full-area Si solar cell. The "upper-limit" voltage at the maximum power point V_{UL} (black lines) follow the color contours indicating the power conversion efficiency from the simulation very well. (Source: [45])

According to simulations for a Si solar cell with a full-area contact (see *Figure 10*), the relationship between V_{mp} and the contact resistivity ρ_C is approximately linear (ρ_C introduces a voltage drop, i.e. a step in the Fermi level) so that ρ_C does not impact V_{mp} for sufficiently low values. Conversely, V_{mp} depends approximately logarithmically on J_{0b} and a smaller J_{0b} improves V_{mp}, until another recombination path becomes dominant. Thus, the simulated efficiency contours and V_{UL} align very well in *Figure 10*.

Some models in the first category assume location-independent majority and minority carrier quasi-Fermi levels in semiconductor within a distance d from the contact (in contrast to the band-diagrams in chapter 2.2), low level injection ($p \approx p_0$), recombination rates that are independent of the majority carrier concentration and that the surface charge does not affect the effective surface recombination velocity S_{eff} (see also chapter 2.3.2). In this case, the relation between the recombination current density at the rear surface J_{recb}, the net recombination rate U_b and S_{eff} can be expressed as

$$J_{recb} = qU_b = qS_{eff}\Delta n_d \tag{50}$$

Here $\Delta n_d = n - n_0$ is the excess minority carrier concentration in the absorber at a distance d from the rear surface so that the minority carrier density is not affected by the surface charge and the recombination is modelled to take place at an imaginary quasi-neutral boundary located at d instead of directly at the contact. S_{eff} does not depend on Δn_d as long as U_b is only limited by the supply of minority carriers. In this case majority carrier transport is not limited and the contact resistance for majority carriers can be neglected, and S_{eff} is sufficient to describe the contact.

When U_b is limited by the supply of both carrier species, the SRH equation for the recombination rate through defect states indicates that S_{eff} generally depends on Δn_d. In this case, J_{recb} is often better described by a diode model (see chapter 2.3.1):

$$J_{recb} = qU_b = J_{0b}\left(\frac{p_b n_b}{n_{ib}^2} - 1\right) =$$

$$= J_{0b}\left(e^{\frac{\varepsilon_{FCb}-\varepsilon_{FVb}}{kT}} - 1\right) = J_{0b}\left(e^{\frac{qV_b}{kT}} - 1\right) \tag{51}$$

Here, the subscript b refers to the actual surface at the rear contact. In case of a small surface charge, J_{0b} depends on Δn_d and the surface charge, but it in case of a large surface charge, it is independent of both. The SRH equation for a single defect energy can be rewritten to show how J_{0b} is determined by the defect parameters:

$$U_b = \frac{p_b n_b - n_{ib}^2}{\frac{p_b + p_1}{S_0^e} + \frac{n_b + n_1}{S_0^h}} = \frac{n_{ib}^2}{\frac{p_b + p_1}{S_0^e} + \frac{n_b + n_1}{S_0^h}}\left(e^{\frac{qV_b}{kT}} - 1\right) \tag{52}$$

$$p_1 = n_{ib}e^{\frac{E_t - E_i}{kT}} \tag{53}$$

$$n_1 = n_{ib}e^{\frac{\varepsilon_i - E_t}{kT}} \tag{54}$$

$$S_0^e = v_{th}^e N_{it}\sigma_{rec}^e \tag{55}$$

$$S_0^h = v_{th}^h N_{it}\sigma_{rec}^h \tag{56}$$

E_t is the energy of the defect state, ε_i the intrinsic Fermi level, N_{it} the interface defect density, S_0^e and S_0^h are the surface recombination velocities, σ_{rec}^e and σ_{rec}^h the capture cross sections and v_{th}^e and v_{th}^h are the thermal velocities for electrons and holes respectively. An overview over the conditions which warrant either the use of equation 50 or 51 is given in [56].

As stated above, models in the second category neglect net recombination at the rear surface. Instead, they model the minority carrier current as exchange current into the contact [26], or both minority and majority carrier currents as exchange currents into the contact[41]. In the context of an inorganic semiconductor-metal contact the exchange currents are modelled as thermionic emission currents [57]. In this case, the recombination current density pre-factor at the rear contact J_{0b} parametrizes thermionic emission current and not SRH recombination. According to the thermionic emission model the electron and hole exchange currents through the transition region are expressed by [26,47]

$$ J_{bTE}^e = \kappa^e \, A_0 T^2 e^{\frac{-\varphi_b^e}{kT}} \left(e^{\frac{\varepsilon_{Fmet} - \varepsilon_{FC}|_{x=b}}{kT}} - 1 \right) \tag{57} $$

$$ J_{bTE}^h = \kappa^h A_0 T^2 e^{\frac{-\varphi_b^h}{kT}} \left(e^{\frac{\varepsilon_{Fmet} - \varepsilon_{FV}|_{x=b}}{kT}} - 1 \right) \tag{58} $$

In above equations κ^e and κ^h are the transmission coefficients, $\varphi_b{}^e$ and $\varphi_b{}^h$ the barrier heights for electrons and holes, respectively, ε_{Fmet} the Fermi level of the metal, which can be changed by a applying a bias (referenced to the semiconductor bulk) and A_0 the universal Richardson constant. The interface can thus be seen as non-linear point-like resistance for electrons and holes and the total resistance is given by the sum of the transport resistance in the space charge region and the resistance of the transition region. The $e^{\frac{-\varphi_b^e}{kT}}$ dependency should however not be interpreted as charge carriers having to cross an energy barrier, but that the barrier depletes the interface[26].

The ratio of the minority to majority exchange current determines the position of the applied potential within the quasi-Fermi level split in the bulk. As $\varphi_b{}^h + \varphi_b{}^e = E_G$, an increase in the majority carrier barrier lowers the minority barrier height. This eventually leads to a step or gradient in ε_{FV} even at V_{OC}, reducing the V_{OC} below the difference of the quasi-Fermi levels in the bulk[47]. Such a loss has been associated with high-level injection[41].

Inserting a tunneling oxide between the semiconductor and the metal (MIS contact, see **paper III**), reduces both κ^e and κ^h, usually (and unfortunately regarding carrier selectivity) by the same factor $e^{\frac{-\varphi_I}{kT}}$, where φ_I is the barrier height for transport through/over the insulator layer[41,47]. Inserting a partial contact as in **paper II** can also be viewed as reducing κ for both electrons and holes. Then, if the minority carrier exchange current dominates the other recombination currents and if the contact operates under low-level injection, V_{OC} improves as the quasi-Fermi level splitting in the bulk increases. If the majority carrier exchange current is further reduced, the contact operates under high-injection conditions and the V_{OC} is reduced below the quasi-Fermi

level splitting in the bulk. A small majority carrier exchange current can eventually degrade the fill factor [41,47] (see also *Figure 24* from **paper III**).

A combination of the lumped diode model and the exchange current model has been suggested in [47] and [26]. In [47] (see *Figure 9*), the minority carriers recombine at the rear surface according to a diode model and the contact resistance is modelled by thermionic emission of the majority carriers in series with the recombination paths, which are modelled by the diode(s). For the majority carriers, a current through an ohmic resistance can be added in parallel to the thermionic emission current. For the minority carriers a thermionic emission current into the rear contact can be added. In the extended model in [26] both generation and recombination are taken into account as a point-like source/sink of minority carriers in addition to the minority carrier exchange current. If the sink is close to the bulk, it adds directly to the total recombination current and reduces the cell-performance significantly. Conversely, if the sink is close to the rear surface, it is only slightly detrimental to the cell performance, since the minority carriers would have recombined via the minority carrier exchange current anyways.

As stated in **paper III**, the rear contact of CIGS and CdTe solar cells has been associated with a kink and roll-over in the *JV* curves especially if measured at low temperatures[58–67]. These solar cells can thus not be described with a model of the first category. The kink has been explained by a hole extraction barrier[60], whereas the roll-over has been explained by a hole injection barrier[58,60,62] and/or a Schottky barrier [63,65,68]. Some studies identified the valence band off-set between CIGS and $MoSe_2$, that is usually formed between the CIGS and Mo[60,67], as the hole injection barrier. A cross-over between the dark and light curve can also be explained by a barrier at the rear contact as exemplified for CdTe solar cells[61,69]. An overview over the effects of a barrier at the rear contact on *JV* curves is given in [18].

Assuming that a hole barrier at the rear contact is responsible for the roll-over of *JV* curves, that the two depletion regions do not overlap and that the minority carriers are not collected by the junction at the rear contact, these *JV* curves have been modelled by a diode in series with the main junction [61,62,66,67,69–73], (see *Figure 11* a). If the holes accumulate between the two space charge regions, compensate the negative charge, lower the hole barrier and modulate the injection of electrons from the Mo into the CIGS, the solar cell works as a phototransistor [63,65]. In both models, the voltage over the complete solar cell is split into the voltage over the primary photodiode and over the secondary diode, so that the primary diode is forward biased and the secondary diode is reverse biased for bias voltages $V \geq V_{OC}$ over the complete solar cell.
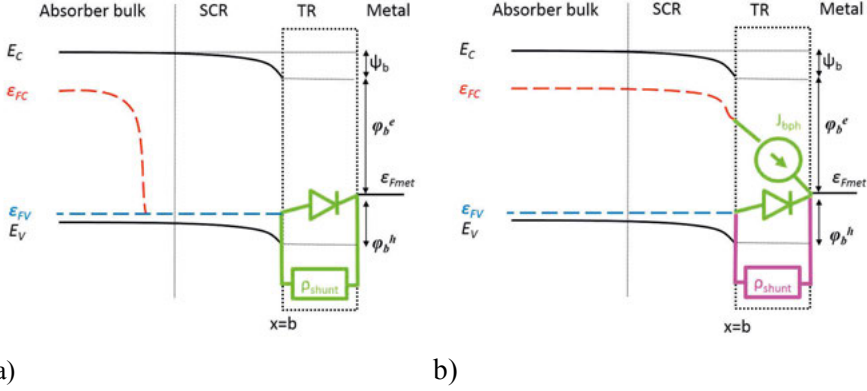
Figure 11. a) Model of the rear contact in CIGS or CdTe solar with optically thick absorbers and a hole barrier described as a diode and shunt resistor in parallel. b) In the solar cells in **paper III** the minority carriers are both generated at the rear contact and reach the rear contact by drift-diffusion. Therefore, I substituted the diode by a photodiode and thus added a photocurrent generator in parallel to the diode.

In **papers III and IV**, I proposed a hole barrier at the rear contact, without stating the exact location of this barrier nor the exact current transport mechanisms. The (highest) hole barrier could be located at the CIGS-MoSe$_2$, or the MoSe$_2$-Mo, or the CIGS-Mo interface if MoSe$_2$ is not formed. In the case of rear contacts with an ultra-thin oxide passivation layer inserted between the Mo and the CIGS, the oxide layer might constitute the highest barrier for holes (see chapter 5.4.3). The current limiting transport mechanism could be thermionic emission (with or without tunneling), drift-diffusion or trap-assisted transport through the passivation layer. All three mechanisms can be described by a diode equation, so that the current transport mechanism is not important for the mathematical description.

The secondary diode's dark saturation current density J_{0b} consists of holes that are injected over the rear barrier from Mo into CIGS. It depends exponentially on the temperature according to

$$J_{0b} = J_{00b} e^{\frac{-\varphi_b^h}{A_b kT}} \tag{59}$$

Hereby, J_{00b} is the reference current density, A_b is the diode's ideality factor and φ_b^h is the height of a barrier for holes at the rear contact, i.e. the energy difference between the Fermi level in the CIGS and the valence band at the CIGS-rear contact interface. At room temperature and for sufficiently small values of φ_b^h, J_{0b} is several orders of magnitude larger than the photocurrent density from the main junction so that the current is not limited, and no roll-over occurs. For high enough voltages over the rear contact barrier the dark saturation current density can increase due to tunneling or a breakthrough.

For optically thin solar cells or solar cells with a long L_{QNR}, some minority carriers reach the rear surface and J_{phb} is additionally generated (**paper II,** see *Figure 11* b). This current density is approximately temperature independent and consists of electrons that with a higher statistical probability end up in the rear contact than in the front contact, as the conductivity for transport to and transfer into the rear contact is higher than for the front contact. By measuring at low temperatures (100 K), J_{0b} can be reduced to about the same level as the secondary photocurrent density J_{phb} at 1% light flux, so that J_{phb} can be discerned. As it is a photocurrent density, it depends on the amount of photons absorbed and the collection function of the secondary junction, and thereby on the incident primary light flux on the solar cell, the absorption profile and the absorber layer thickness (see chapter 2.3.2). If the collection function of the main diode depends on the carrier loss at the rear surface, the photocurrent over the main diode J_{phm} and the photocurrent over the secondary diode J_{phb} cannot be described independently from each other. J_{phb} corresponds approximately to a minority carrier recombination current into the contact. It is however neither modelled by a diode model for a recombination path at the rear surface in parallel to other recombination paths as in the models of the first category [9,20,45,48,56] nor by a thermionic emission model for the transport of minority carriers into the contact in parallel to the thermionic emission of majority carriers as in the models of the second category [26,41,47]. Instead, J_{phb} is generated by a current source in parallel with the majority carrier diode at the rear contact (see the equivalent circuit in *Figure 18*).

A shunt conductance G_b can be added in parallel to the secondary (photo-)diode [61,71]. While such a G_b was not necessary to model the cells in **paper II**, we introduced it in **paper III** to explain the absence of roll-overs in the *JV* curves measured at low temperatures.

Thus, four current density components can flow over the reversely-biased rear contact: the secondary diode's saturation current density J_{0b} carried by holes, a breakthrough current for reverse biases over the secondary diode higher than its breakthrough voltage also carried by holes, the secondary photocurrent density J_{phb} carried by electrons and the hole current density over the secondary shunt J_{shb}. J_{0b} and J_{phb} determine the *JV* point above V_{OC}, where the *JV* curve becomes current limited, and the slope of the roll-over curve is determined by G_b. If $1/G_b$ equals or is smaller than the lumped series resistance of the device, the slope of the roll-over matches the slope of the *JV* curve at V_{OC} and the roll-over disappears regardless of $\varphi_b{}^h$ [61]. $\varphi_b{}^h$ may be quantified by *JVT* measurements, either by extracting J_{0b} for independent diodes for optically thick solar cells [66,67,72] or from V_{OC}-T graphs for the phototransistor model[63] and also for two independent junctions for optically thin solar cells as I showed in the appendix to **paper III**. I repeat this derivation in chapter 3.4.

2.5 Rear surface passivation

Thinning down the CIGS absorber decreases material consumption and may increase throughput in production. It can also increase the V_{OC}, namely if the same number of free carriers is confined into a smaller absorber volume compared to common absorber volumes, so that the free hole and electron density and thus the difference between the quasi-Fermi levels increases. Therefore, CIGS solar cells with thin and ultra-thin absorber layers are increasingly being explored by researchers.

In reality, thin absorber layers do not confine the same number of free carriers, as thinning down the absorber layer also reduces photo-absorption in the absorber and increases the impact of rear surface recombination on the collection function. Furthermore, voltage-dependent photocurrent collection and shunt like behavior under illumination have been observed and the superposition principle may fail[55,74–77]. To increase the reflection at the rear surface, oxide layers, nanoparticles and nanopatterns have been introduced into the rear contact region[78–83]. Interface recombination has been curbed by front surface[84,85] and rear surface oxide passivation layers (citations are given in detail in chapter 5).

According to equation 52, recombination at the absorber interfaces can be suppressed by reducing N_{it} (chemical passivation) and/or by making one carrier concentration much smaller than the other (carrier population control[35]). At a fixed difference of the quasi-Fermi levels $F=\varepsilon_{FC} - \varepsilon_{FV}$, U_b is highest for $p \cdot \sigma_{rec}{}^h = n \cdot \sigma_{rec}{}^e$ and decreases strongly for asymmetric carrier concentration densities[9,35,46].

Relative charge carrier concentrations can be modified by

    a.   heavy doping or use of high band gap materials with an asymmetric band gap offset to the absorber layer (for example as in a p$^+$ rear contact layer in p-type Si solar cells[9,24] or for a high Na concentration at the rear contact in CIGS solar cells, as mentioned in chapter 3.7)

    b.   grading of the conduction band,

    c.   adjusting the metal contact work function so that majority charge carriers are accumulated[9] and

    d.   by other charge assisted control (for example fixed charges in insulator passivation layers)[9].

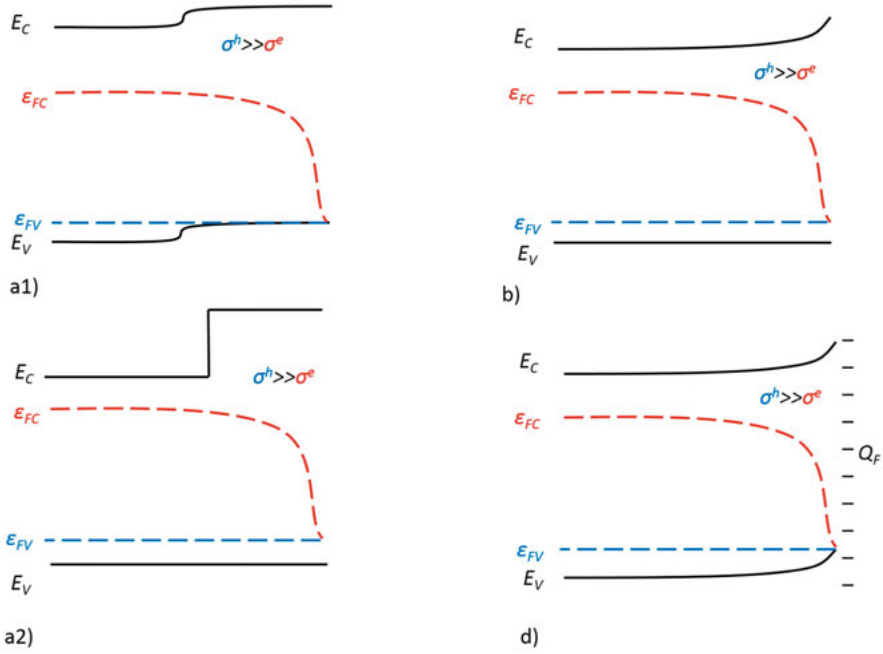Band diagrams for these methods are depicted in *Figure 12*.

Figure 12. Band diagrams at V_{OC} for different methods to establish asymmetrical conductivities in the selective membrane at a hole contact. a1) p^+p homojunction, a2) heterojunction, b) conduction band grading, d) fixed oxide charge (adopted from: [42])

If the insulator passivation layer has a high concentration of negative charges, the positive charge of a thin sub-surface (accumulation layer) with strongly elevated hole concentration and reduced electron concentration mirrors the insulator charge in a p-type semiconductor such as CIGS. A sufficiently high positive oxide charge would form an inversion layer, with a high concentration of electrons and a low concentration of holes.

In addition, the layer with strongly asymmetrical carrier concentrations acts as a carrier selective membrane, as the charge carrier conductivities $\sigma^e=q \cdot \mu^e \cdot n$ and $\sigma^h=q \cdot \mu^h \cdot p$ and thus $J^e=(\sigma^e/q)(d\varepsilon_{FC}/dx)$ and $J^h=(\sigma^h/q)(d\varepsilon_{FV}/dx)$ become much larger for the majority carriers, even in the presence of a large driving force $d\varepsilon_{FC}/dx$ on the minority carriers close to the contact. Conduction by a single carrier type and a reduction of surface recombination thus go hand in hand, as both require an asymmetry in carrier concentrations[9,23,30].

Thus, a negative oxide charge as found in annealed ALD-Al$_2$O$_3$ (see chapter 5.1.1) passivates the contact in the following ways:

1) It lowers φ_b^h in its vicinity, which can reduce majority carrier transport losses (see equations 10, 11 and 49)
2) It increases the asymmetry of the minority and majority carrier density, which decreases the SRH recombination or the minority carrier transfer

current into the rear contact or J_{phb} depending on the empirical model used.

The lowering of the hole barrier can be seen as a measure for the increase in asymmetry of the minority and majority carrier density and vice versa. For which sample types and to what extent $\varphi_b{}^h$ is lowered is discussed in **paper II and III** and in chapter 5.2.4.1 and chapter 5.4.3.

Traditionally, all four passivation methods named above are explained by electrical fields[33] acting on the photo-generated excess minority charge carriers: a) electrical field (back surface field) at the p^+p-homojunction , b) quasi-electric field due to band grading (for example Ga grading with higher Ga concentration at the rear contact in CIGS solar cells[10,55,86]), c) electrical field at a metal-semiconductor junction and d) quasi-electrical field due to a fixed oxide charge. The following explanation of the passivation effect is used [87–91]: An electric field acts like an electron mirror and drifts away light generated minority carriers from the passivated contact so that they cannot recombine there. The term "drift assisted minority carrier diffusion enhancement"[90] is sometimes used to describe the electrical field's effect on the minority carrier diffusion length. According to [9], this picture cannot explain cases where a depletion region is formed at the rear contact in silicon solar cells, but recombination becomes worse. It is just another face of the notion that the built-in electrical field is directly responsible for the separation of excess charge carriers at pn-junctions (compare chapter 2), disregarding that the electrical field exerts a conservative force.

In the introduction to **papers II and III,** I have referred to the field effect (implying that it acts on excess minority carriers) to motivate the usage of a charged oxide layer. In the introduction to **paper IV**, however, I have shifted to a motivation based on charge carrier concentration asymmetries as explained above. The two-diode model describing the majority carrier current in **papers II and III** is not strongly affected by this re-interpretation. The oxide charge might however not reduce the drift component, but increase σ^e in series with a reduced recombination rate due to the asymmetry of carrier densities[35]. Therefore, I have reformulated some important details in this thesis compared to the papers.

3 Characterization and modeling

Unintentional deviations between the solar cells on a single sample can be large. Whereas a high number of processing steps is not at all uncommon in thin film processing for solid state electronics, the large area of solar cell devices makes defects more probable. At an area of 0.5 cm^2, the solar cells in this work are over 7 orders of magnitude larger than the area of many silicon based electronic devices. Moreover, the CIGS peels often from passivated rear surfaces during the chemical bath deposition of CdS, especially if thick NaF precursor layers or thick passivation layers without nanopatterning are used. The peeling starts often in the corners of the sample, so that either the number of devices to be analyzed is reduced or the sample cannot be used at all. I excluded cells that are obvious outliers (for example shunted cells or cells with too high J_{SC} due to poor scribing) from the analysis or used only a certain amount of the best cells (that are not positive outliers) in the analysis. This selection process is not completely objective. In **paper IV**, I show the results of all cells as by far more unpassivated reference cells than passivated cells were shunted (*Figure 23*).

Measurement results for a single cell cannot be reproduced, if this cell is not stable over time. As not all device characterization can be done on the same day, a subjective decision has to be taken concerning which results can be reported together. For example, if I measure current density-voltage *(JV)* curves, thereafter capacitance-voltage (*CV*) curves and *JV* curves again and the measurement results differ, do I report the first *JV* or the second *JV* curves together with the *CV* curves? Do I report both? If I report only the first *JV* curves, do I mention that I measured them again, and that the results were different? Will my honesty backfire, as the paper's story becomes muddled and is drowned out by details? In **paper III**, we decided to present those results that indicated a smaller passivation effect and focused on the general trends for the different Na supply methods instead.

If I had to describe and justify all small subjective decisions I have made in my work, that description would fill pages. That being said, I have still described the sample processing, the number of samples and cells per sample, the number of cells actually used for the analysis and measurement in more detail than common to enable the reader to judge the quality of the data themselves.

3.1 External, internal and apparent quantum efficiency
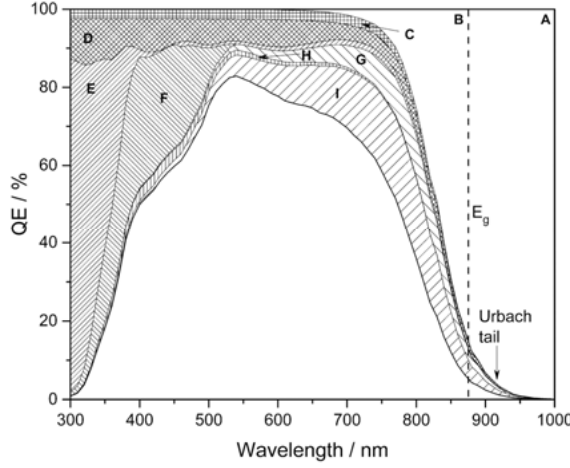
Figure 13. Schematic external quantum efficiency and optical losses for a CIGS solar cell. (A) sub-band gap generation losses, (B) incomplete absorption in the CIGS absorber layer corresponding to parasitic absorption in the Mo rear contact, (C) shading from the grid, (D) front surface reflection, (E) parasitic absorption in the window layers including free carrier absorption, (F) parasitic absorption in the CdS layer, (G) incomplete collection due to rear contact recombination, (H) incomplete collection due to front surface recombination, (I) incomplete collection due to recombination losses in the bulk. (Source: [92])

If one measures J_{SC} of a monochromatically illuminated solar cell, and divides the number of charge carriers extracted from the solar cell by the number of photons hitting the solar cell, one arrives at the external quantum efficiency *EQE* for that wavelength (see *Figure 13*).

$$EQE(\lambda) := \frac{dJ_{ph}(V = 0, \lambda, j_\gamma)}{q \, dj_\gamma(\lambda)} \qquad (60)$$

The *EQE* is thus the probability that an incident photon contributes to J_{SC} and can therefore be written as the product of the absorptance (see chapter 2.3.2) and a collection probability, the so-called internal quantum efficiency, *IQE*.

$$EQE(\lambda, j_\gamma) = A_a(\lambda)\mathrm{IQE}(\lambda, j_\gamma) \qquad (61)$$

Thus, the *IQE* quantifies the recombination losses at different wavelengths. The absorptance is often simplified by neglecting the T_w and A_{par}. This means that all photons not reflected at the solar cell are assumed to generate electron hole pairs.

$$A_a(\lambda) = 1 - T_w(\lambda) - R(\lambda) - A_{par}(\lambda) \approx 1 - R(\lambda) \qquad (62)$$

59

R can be measured on the whole solar cell stack and the *IQE* can be calculated from the *EQE* and *R* data. For CIGS solar cells with thin absorber layers this simplification cannot be made for photons with energy values close to E_G.

The EQE can also be expressed as the convolution of the normalized generation rate G_n and the collection function $\eta_C(x,V)$.

$$EQE = \int_0^{d_a} G_n(\lambda, x)\eta_C(x, V = 0, j_\gamma)dx \qquad (63)$$

If G_n respectively A_a are equal for two solar cells, all differences in the *EQE* data stem from differences in η_C respectively in *IQE*. Thus, we estimated how much of the difference in *EQE* stemmed from a difference in A_a (**papers II, III, IV**) by comparing two otherwise equal solar cells with and without a rear surface passivation layer. The reflectance of the whole sample stacks was measured for both passivated and unpassivated reference samples with a Perkin Elmer L900 spectrophotometer with an integrating sphere. The differences in reflectance at the whole sample stacks can only explain a small part of the differences in *EQE*. The thickness of the Al$_2$O$_3$ layers and the complex refractive indices of the Mo, the Al$_2$O$_3$ and the CIGS (with $GGI = 0.15$ for **papers III and IV** and $GGI = 0.60$ for **paper II**) were determined by spectroscopic ellipsometry on different sample stacks with a Woolam VASE instrument. The reflectance at the rear surface was determined to be only slightly larger when a passivation layer is introduced between the Mo and the CIGS. For example, it increases from 13% to 16% at 785 nm wavelength if an Al$_2$O$_3$ passivation layer with a thickness of 6 nm is introduced between the Mo and the CIGS with a $GGI = 0.15$. The obtained refractive index and absorption coefficient were used to calculate the light intensity reaching the rear surface at different wavelengths using the transfer matrix method. According to these calculations most light is absorbed in a single pass of the absorber, even for the thinnest absorber layers. For example, for the samples with a 450 nm absorber layer with a $GGI = 0.60$, only 10% of the increase in the J_{SC} due to the 27 nm thick Al$_2$O$_3$ passivation layer could be explained by a higher A_a.

For a certain photon density spectrum, J_{ph} can be calculated from the *EQE*.

$$J_{ph,EQE}(V = 0, j_\gamma) = q \int \frac{dj_\gamma(\lambda, x = 0)}{d\lambda} EQE(\lambda, j_\gamma)d\lambda =$$

$$= q \int \frac{dj_\gamma(\lambda, x = 0)}{d\lambda} A_a(\lambda)IQE(\lambda, j_\gamma)d\lambda \qquad (64)$$

Measuring the EQE and calculating the $J_{ph,EQE}(AM1.5G)$ for the AM1.5G spectrum can be more accurate than measuring the J_{SC} with the *JV* set-up, as the spectrum of the lamp of the *JV* set-up does not reproduce the AM1.5G

spectrum well in the infrared region. The infrared region of the spectrum influences the J_{SC} differently for different band gaps, so that the J_{SC} from the JV measurements cannot be reliably compared. Therefore, the J_{SC} was re-adjusted according to the $J_{ph,EQE}(AM1.5G)$ derived from EQE measurements in **paper I**. The light intensity reaching the solar cell in most EQE measurement set-ups is however much smaller than 1000 W/m^2. If J_{SC} depends on j_γ, $J_{ph,EQE}(AM1.5G)$ is not equal to $J_{SC}(AM1.5G)$ (see chapter 3.3).

The band gap can be extracted from the EQE by plotting EQE^2 against the photon energy $\hbar\omega$ and fitting the low photon energy part of the curve linearly. The intercept of the fitted line with the $\hbar\omega$-axis, gives the approximate band gap energy (see **paper III**). If the quantum efficiency is measured under a voltage bias, it is referred to as apparent quantum efficiency AQE. By comparing the values of the AQE at different biases, the bias-dependency of the main recombination mechanism can be explored. In **papers I and IV** the EQE and AQE was used to analyze the apparent shunt behavior of (ultra-)thin solar cells without a rear surface passivation layer and with such a layer. In all other **paper**s the EQE and IQE data is only analyzed qualitatively, for example to distinguish parasitical absorption from recombination losses at the rear surface.

The ratio between the AQE and EQE for a solar cell according to the Gärtner formula[18,28] is

$$
\frac{AQE}{EQE} = \frac{T(\lambda)(1 - R(\lambda)\left(1 - \dfrac{e^{-\alpha_a(\lambda)w_a(V)}}{1 + \alpha_a(\lambda)L_{QNR}}\right)}{T(\lambda)(1 - R(\lambda)\left(1 - \dfrac{e^{-\alpha_a(\lambda)w_a(V=0)}}{1 + \alpha_a(\lambda)L_{QNR}}\right)} =
$$
$$
= \frac{1 + \alpha_a(\lambda)L_{QNR} - e^{-\alpha_a(\lambda)w_a(V)}}{1 + \alpha_a(\lambda)L_{QNR} - e^{-\alpha_a(\lambda)w_a(V=0)}} \tag{65}
$$

and is a measure for voltage dependent photocurrent collection due to an increase in d_w at negative bias. For short wavelengths $\alpha_a(\lambda)w_a(V) \gg 1$, and the EQE approaches unity regardless of bias. The dependency of the AQE on bias increases with longer wavelengths, as can be seen from *Figure 14*.

The group's *EQE* measurement set-up consists of a Xenon arc lamp and a monochromatic filter wheel, which varies the wavelength of the light beam from ultra-violet (UV) to infrared (IR). To prevent photons from the ambient light to contribute to the *EQE* signal, the beam is chopped, and the measurement signal is processed by a lock-in amplifier synchronized with the chopper. Then, the beam is split by a semitransparent mirror, which transmits a part of the beam to a monitoring detector which monitors changes in light intensity over time. The main part of the beam is focused on the solar cell, which generates a current. Before *EQE* measurements, the set-up is calibrated

with a GaAs and a Si calibration sample. The preliminary quantum efficiency value is multiplied with the ratio of intensity on the monitor detector during calibration and during the measurement for every wavelength. Finally, the current is converted to a voltage, which is the input signal for the lock-in amplifier.
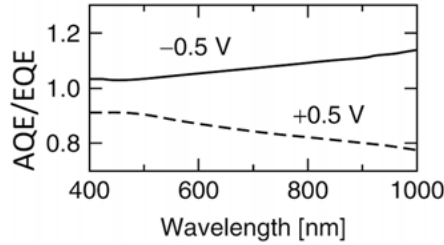

Figure 14. Simulated ratio of the AQE to EQE for an AQE at -0.5 V reverse bias and 0.5 V forward bias. (Source: [18])

3.2 Current-voltage measurements

The first electrical measurement on newly fabricated solar cells are current-voltage (*IV*) measurements in the dark and under light at 25°C. As the current density *J* is independent of the solar cell area, current-density-voltage (*JV*) curves are usually published. The sample temperature is maintained by a Peltier element in the sample stage. The light source of our home-built solar simulator is a Quartz Halogen lamp with a cold mirror. The distance between the lamp and the sample stage is adjusted so that a certified reference solar cell gives a pre-defined J_{SC}. A Keithley 2401 source measure unit sweeps the voltage between a probe contacting a pad of the Ni-Al-Ni grid and a probe contacting the rear contact. The current is measured between two other probes, just next to the voltage probes to avoid the influence of resistive losses in the cables and the contact resistance on the measurement results (four-point probe technique).

From the *JV* curve, the primary characteristic parameters of a solar cell, J_{SC}, V_{OC}, fill-factor FF and the maximum power point (V_{mp}, J_{mp}), can be easily read. The J_{SC} and V_{OC} are the two points where the *JV* curve intersects the voltage and current density axis, respectively (see *Figure 15*). The FF gives the ratio between the maximum power density $P_{mp} = V_{mp} \cdot J_{mp}$ and the product of J_{SC} and V_{OC}.

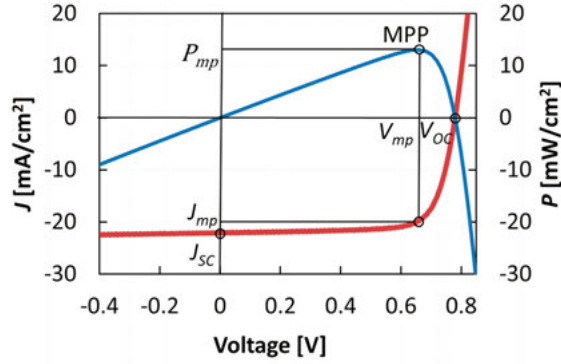$$FF = \frac{V_{mp} \cdot J_{mp}}{V_{OC} \cdot J_{SC}} \qquad (66)$$

Figure 15. Current density-voltage (*JV*) curve and power density-voltage (*PV*) curve of a solar cell from **paper I**. The absorber of this solar cell is 1.50 μm thick and has a $GGI \approx 0.6$. The short-circuit current density J_{SC}, the open-circuit voltage V_{OC}, the maximum power point (MPP), the voltage V_{mp}, the current density J_{mp} and the maximum power density P_{mp} at the MPP are marked.

The maximum power conversion efficiency η is the ratio between maximum output power density and the power density P_{in} arriving at the solar cell from the light source.

$$\eta = \frac{V_{mp} \cdot J_{mp}}{P_{in}} \tag{67}$$

JV curves were also measured at different temperatures in a home-built cryostat with a sample stage cooled with liquid nitrogen. Such measurements are often referred to as *JVT* or *JV(T)* measurements. Even here, a four point-measurement technique is used. The power of the light source, three white LEDs, is adjusted so that the solar cell produces the same J_{SC} as in the *JV*-set up. The spectrum of the white LEDs covers the whole visible spectrum, with two large peaks around 450 and 550 nm, which gives a poor approximation of the AM1.5G spectrum. As the sample stage is only 5 cm x 5 cm and the illumination is very inhomogeneous, the samples have to be cut so that the solar cell under test can be placed into the middle of the sample stage. These measurements are therefore usually the last conducted on a sample. The influence of the temperature on *JV* curves and how the band gap and the height of the hole barrier at the rear contact can be extracted from $V_{OC}(T)$ curves is discussed in chapters 3.4 and 5.4.2.

3.3 Equivalent circuit with one diode and apparent shunt conductance

In **paper I**, the parameters of a one-diode model have been extracted from the *JV* curves according to a method proposed in [93]. This one-diode model describes the solar cell with a single diode modeling the main junction/main recombination path at medium voltages in the dark, a current source depicting J_{ph}, a lumped shunt conductance G_{sh} in parallel to the diode and a series resistance R_S, which lumps together the spreading resistance through the front and back electrodes, contact resistances, the resistance in all films and the collection grid. The analytical form of the *JV* curve according to this one-diode model is

$$J_{light} = J_0 \left(e^{\frac{q(V-R_S)}{AkT}} - 1 \right) + G_{sh}(V - J_{light}R_S) - J_{SC} \qquad (68)$$

As G_{sh}, R, J_{SC} and J_0 are assumed to be constant, this model can only describe solar cells that fulfil these assumptions. As the light *JV* curves of the solar cells in **paper I** could not be described by equation 68, we decided to publish only the extracted parameters for the dark *JV* curves.

To improve the model, we introduced first a voltage-dependent external collection efficiency

$$\eta(V) = \frac{J_{ph}(V)}{J_{SC}} = \frac{q \int \eta_C(x,V)G(x)\,dx}{J_{SC}} \qquad (69)$$

(see chapter 2.3.2). As traditionally described, voltage dependent photocurrent collection[94] takes place in devices with a collection probability < 1 in the quasi neutral region, caused by either a low bulk minority carrier diffusion length or by rear surface recombination, in combination with negligible recombination in the space-charge region. The collected current is then dominated by carriers from the depletion region. When the solar cell is increasingly forward biased, d_w is gradually reduced and hence, current collection is decreased (compare to equation 65). Voltage dependent photocurrent collection can also stem from interface recombination at the front contact and/or a photocurrent barrier at the front contact [18]. As the front contact has not been intentionally changed between the different sample types in **papers I and IV**, we assume that the front contact is not responsible for the increase in voltage dependent photocurrent collection in solar cells with thin absorber layers and unpassivated rear surface.

Neglecting R_S but adding $\eta(V)$, equation 54 can be expanded to

$$J_{light}(V) = J_{diode}(V) + G_{sh}V - J_{ph}(V) = J_{dark}(V) - \eta(V) \cdot J_{SC} \qquad (70)$$

to consider voltage-dependent photocurrent collection. Then the slope dJ_{light}/dV is the sum of the slope dJ_{dark}/dV and the slope of dJ_{ph}/dV, which corresponds to the slope between J_{ph} calculated from the *AQE* and the *EQE* (see *Figure 16*).

$$\left.\frac{dJ_{light}}{dV}\right|_{V<0} = \left.\frac{dJ_{diode}}{dV}\right|_{V<0} + G_{sh}|_{V<0} - \left.\frac{dJ_{ph}}{dV}\right|_{V<0} =$$
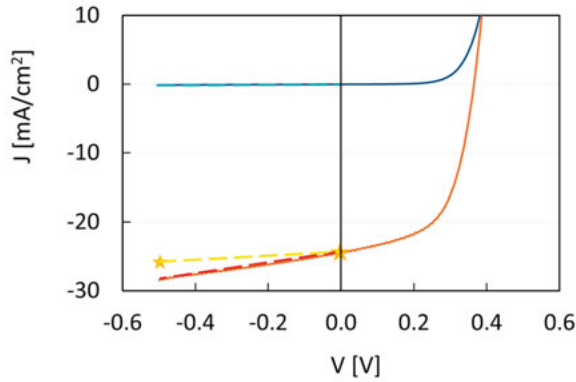$$= \left.\frac{dJ_{dark}}{dV}\right|_{V<0} - \left.\frac{dJ_{ph}}{dV}\right|_{V<0} \qquad (71)$$

Figure 16. Dark and light current density-voltage (*JV)* curve for a cell with a $GGI \approx 0.15$ and a thickness of 0.5 µm (**paper I**). The stars denote the measured photocurrent densities $J_{ph,EQE}$ deducted from voltage-biased apparent quantum efficiency *AQE* and external quantum efficiency (*EQE*) measurements.

As equation 71 could still not describe the measured *AQE, EQE* and *JV* data in **paper I**, we added a third term on the right-hand side, which we called "residual slope" dJ_{res}/dV.

$$\left.\frac{dJ_{light}}{dV}\right|_{V<0} = \left.\frac{dJ_{diode}}{dV}\right|_{V<0} + G_{sh}|_{V<0} - \left.\frac{dJ_{ph}}{dV}\right|_{V<0} - \left.\frac{dJ_{res}}{dV}\right|_{V<0} =$$
$$= \left.\frac{dJ_{dark}}{dV}\right|_{V<0} - \left.\frac{dJ_{ph}}{dV}\right|_{V<0} - \left.\frac{dJ_{res}}{dV}\right|_{V<0} \qquad (72)$$

As the *AQE* and *EQE* were measured under much lower photon fluxes j_{y2} than the light *JV* curves, which are measured under AM1.5 light bias j_{y1}, this residual slope stems from the light dependency of one or several of the terms in equation 70, namely $J_{diode}(V,j_y)$, $G_{sh}(j_y)$ or $\eta(V,j_y)$. If only $\eta(V,j_y)$ depends on j_y, then

$$\left.\frac{dJ_{res}}{dV}\right|_{V<0} = \frac{dJ_{ph}(V=0,j_{y1})}{dV} - \frac{dJ_{ph}(V=0,j_{y2})}{dV}$$

and the solar cell is described by

$$J_{light}(V, j_\gamma) = J_{diode}(V) + G_{sh}V - \eta(V, j_\gamma)J_{SC}$$
$$= J_{dark}(V) - \eta(V, j_\gamma)J_{SC} \qquad (73)$$

If only $G_{sh}(j_\gamma)$ depends on the solar photon flux, then

$$\left.\frac{dJ_{res}}{dV}\right|_{V<0} = G_{sh}(j_{\gamma 1}) - G_{sh}(j_{\gamma 2})$$

and the current density under illumination becomes

$$J_{light}(V, j_\gamma) = J_{diode}(V) + G_{sh}(j_\gamma)V - \eta(V)J_{SC} \qquad (74)$$

If all three parameters, $G_{sh}(j_\gamma)$, $J_{diode}(V, j_\gamma)$ and $\eta(V, j_\gamma)$ depend on the solar photon flux, the solar cell needs to be described by the following general equation:

$$J_{light}(V) = J_{diode}(V, j_\gamma) + G_{sh}(j_\gamma)V - J_{ph}(V, j_\gamma) =$$
$$= J_{diode}(V, j_\gamma) + G_{sh}(j_\gamma)V - \eta(V, j_\gamma)J_{SC} \qquad (75)$$

Reasons for the light dependence of J_{diode} include, amongst others, an illumination dependent carrier lifetime, a large series resistance changing the boundary condition for recombination in the quasi-neutral region or a change from low to high injection under illumination[18]. $G_{sh}(j_\gamma)$ can depend on the solar photon flux density, due to light dependent shunt paths. $\eta(V, j_\gamma)$ can become light dependent due to a phototransistor effect as proposed in reference [12] and a high recombination rate at the rear surface.

In *Figure 17* a quantitative comparison of the four slopes $\left.\frac{dJ_{light}}{dV}\right|_{V<0}$, $\left.\frac{dJ_{dark}}{dV}\right|_{V<0}$, $\left.\frac{dJ_{ph}}{dV}\right|_{V<0}$, $\left.\frac{dJ_{res}}{dV}\right|_{V<0}$ is depicted for the samples with varying *GGI* and d_a in **paper I**. For all cells the dark shunt conductance $G=J_{dark}/dV$ (the slope for the dark *JV* curve) is smaller than dJ_{light}/dV (the slope for the light *JV* curve) and voltage dependent current collection (dJ_{ph}/dV) (the slope from J_{ph} derived from *AQE* or *EQE* data) can only partially explain this discrepancy. The remaining part of the light *JV* curve's slope (dJ_{res}/dV) is also shown. For the cells with 0.5 µm thin absorbers and regardless of the GGI, about 70% of the value of dJ_{light}/dV cannot be explained by a voltage dependent current collection (dJ_{ph}/dV) that is independent of light bias and remain as a residual slope dJ_{res}/dV. dJ_{res}/dV decreases with increasing absorber thickness, regardless of *GGI*. The dark shunt conductance contributes only with less than 5% to the slope of the light *JV* curve ($dJ_{light}t/dV$). The dependency of the dark shunt conductance on the *GGI* becomes therefore negligible. According to unpublished *EQE* and *AQE* measurement data, which

was recorded under different photon flux densities, the *EQE* and *AQE* indeed increase with increasing j_γ. A light bias dependent *EQE* indicates that $\eta(V, j_\gamma)$ is light dependent. With the available *EQE* set-up it was however not possible to quantify the dependency of $\eta(V, j_\gamma)$ on the light bias.

I present more details in chapter 5.4.4 but state already here that the large apparent shunts for CIGS solar cells with ultra-thin absorber layers are strongly reduced by rear surface passivation in **paper IV**. For those solar cell samples, the Al_2O_3 rear surface passivation layer reduces both the voltage dependent current collection and the residual shunt compared to the unpassivated references.
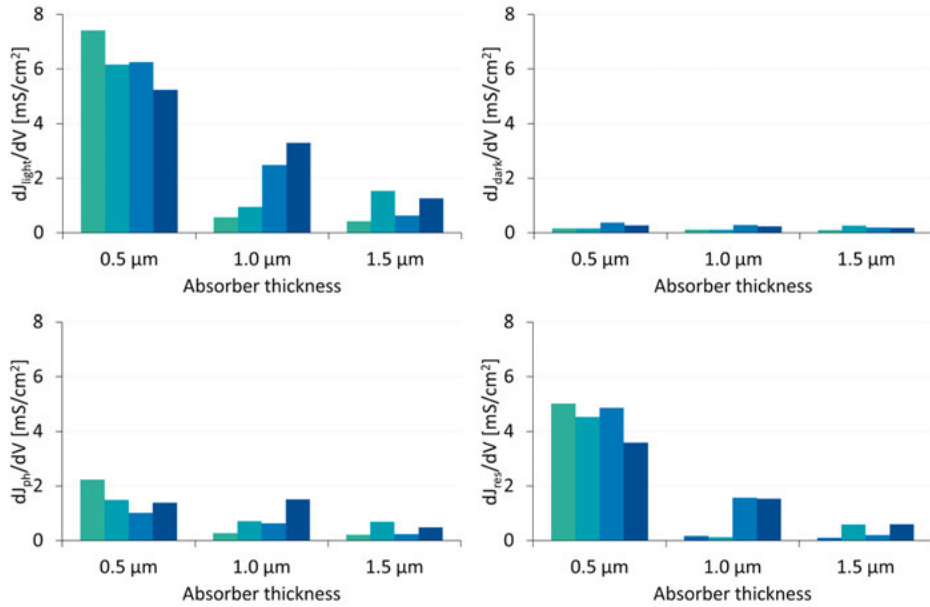

Figure 17. Apparent shunt behavior of samples with different values of the $GGI \approx 0.15$, 0.30, 0.45 and 0.60 and absorber layer thickness (**paper I**). Apparent shunt conductance derived from a) the light *JV* curves, b) the dark *JV* curves and c) *EQE/AQE* measurements(c). In d) the residual slope dJ_{res}/dV is plotted.

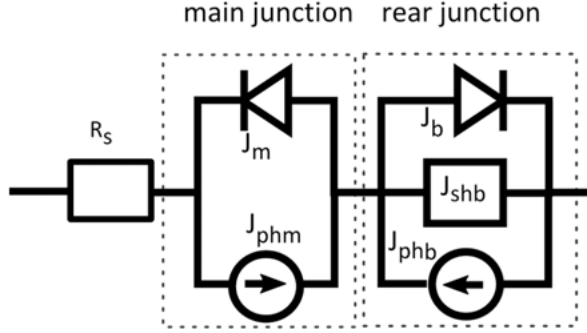## 3.4 Equivalent circuit with two diodes in series

Figure 18. Equivalent circuit of the two-diode model for thin film solar cells used in **papers II and III**. The primary diode with a current source in parallel, represents the main junction and the associated currents, i.e. the diode current density J_m and the photocurrent density $J_{phm,}$ the secondary diode with a current source and a shunt in parallel represents an energy barrier at the rear contact and the associated current densities: a diode current density J_b, a secondary photocurrent density J_{phb} and a shunt current density $J_{shb}=G_b V_b$. The different series resistance components are combined in a lumped series resistance R_S.

By adding the equivalent circuit of the rear contact described at the end of chapter 2.4 to the one-diode equivalent circuit in chapter 3.3, we arrive at an equivalent circuit with two diodes in series (see *Figure 18*). As I have already described the currents at the rear contact in chapter 2.4, I only present the derivation of the V_{OC}-T behavior for the two diode model here and explain how $\varphi_b{}^h$ can be extracted from JV measurements at different temperatures.

The derivation of the V_{OC}-T behavior for the phototransistor model[63] can be generalized, so that the V_{OC}-T behavior also describes solar cells not functioning as a phototransistor. At open circuit the current densities J_m and J_b over the main junction and the rear contact, respectively, are given as

$$J_m = J_{0m}\left(e^{\frac{qV_{ocm}}{A_m kT}} - 1\right) - J_{phm} = J_{00m}e^{\frac{-E_a}{A_m kT}}\left(e^{\frac{qV_{ocm}}{A_m kT}} - 1\right) - J_{phm} = 0 \quad (76)$$

$$J_b = -J_{0b}\left(e^{\frac{qV_{OCb}}{A_b kT}} - 1\right) + J_{phb} - G_b \cdot V_b =$$

$$= -J_{00b}e^{\frac{-\varphi_b^h}{A_b kT}}\left(e^{\frac{qV_{OCb}}{A_b kT}} - 1\right) + J_{phb} - G_b \cdot V_b = 0 \quad (77)$$

where E_a is the activation energy for the dominant recombination process in the solar cell (band to band recombination over the CIGS band gap or the interface band gap or recombination over interface states in the case of Fermi level pinning at the interface[95]), A_m and A_b are the ideality factors for the

two junctions, V_{OCm} and V_{OCb} are the voltages over the main junction and the barrier at the rear contact under open circuit conditions, respectively, (compare *Figure 18*). As both junctions are in series, the V_{OC} over the device is

$$V_{OC} = V_{OCm} + V_{OCb} \tag{78}$$

By substituting

$$V_{OCm} = \frac{A_m kT}{q} \ln\left(\frac{J_{phm}}{J_{0m}} + 1\right) \tag{79}$$

and

$$V_{OCb} = -\frac{A_b kT}{q} \ln\left(\frac{J_{phb} - G_b \cdot V_{OCb}}{J_{ob}} + 1\right) \tag{80}$$

the V_{OC} can be written as

$$V_{OC} = \frac{kT}{q}\left(A_m \ln\left(\frac{J_{phm}}{J_{0m}} + 1\right) - A_b \ln\left(\frac{J_{phb} - G_b \cdot V_{OCb}}{J_{ob}} + 1\right)\right) \tag{81}$$

At high temperatures $J_{0b} \gg J_{phb}$ (low injection) and if $J_{0b} \gg G_b V_{OCb}$, the second term can be neglected and equation 81 simplifies to

$$V_{OC} \approx \frac{A_m kT}{q} \ln\left(\frac{J_{phm}}{J_{0m}} + 1\right) \tag{82}$$

As $J_{0m} \ll J_{phm}$, V_{OC} can be further simplified and J_{0m} can be substituted according to equation 76, giving an approximately linear relationship between the V_{OC} and the temperature at high temperatures:

$$V_{OC} \approx \frac{E_a}{q} + \frac{A_m kT}{q} \ln\left(\frac{J_{phm}}{J_{00m}}\right) \tag{83}$$

At low temperatures (and high photon flux densities), $J_{0b} \ll J_{phb}$ and $J_{0m} \ll J_{phm}$, so that V_{OC} simplifies to

$$V_{OC} \approx \frac{kT}{q}\left(A_m \ln\frac{J_{phm}}{J_{0m}} - A_b \ln\frac{J_{phb} - G_b \cdot V_{OCb}}{J_{ob}}\right) =$$
$$= \frac{kT}{q} \ln\left(\left(\frac{J_{phm}}{J_{0m}}\right)^{A_m}\left(\frac{J_{0b}}{J_{phb} - G_b \cdot V_{OCb}}\right)^{A_b}\right) \tag{84}$$

By substituting for J_{0m} and J_{0b} according to equations 76 and 77, V_{OC} for low temperatures finally becomes

$$V_{OC} \approx \frac{E_a - \varphi_b^h}{q} + \frac{kT}{q} \ln \left(\left(\frac{J_{phm}}{J_{00m}}\right)^{A_m} \left(\frac{J_{00b}}{J_{phb} - G_b \cdot V_{OCb}}\right)^{A_b} \right) \qquad (85)$$

If $G_b V_{OCb} < J_{phb}$ or if V_{OCb} is approximately temperature independent, and if A_m and A_b are approximately temperature independent, the ln-term is only slightly temperature dependent and the relationship of the V_{OC} and the temperature is also approximately linear at low temperature.

The slope and the constant describing the linear relation differ between the low and high temperature behavior (compare equation 82 and 85). Therefore, two values φ_L and φ_H can be extrapolated for $T = 0\ K$ from linear fits to the V_{OC}-T data at low and high temperature (see *Figure 19*). If the ideality factor of the main diode stays constant in the temperature range used for the extrapolation, $\varphi_L = E_a$. If $\varphi_L = E_a$ is equal to the band gap, the difference $\Delta\varphi = E_a - \varphi_H = \varphi_b{}^h$ is the height of the barrier for hole transport at the rear contact. Thus, it is possible to determine $\Delta\varphi$ as the difference $\Delta\varphi = \varphi_L - \varphi_H$ between the extrapolated V_{OC} at $0\ K$ for a linear fit of the low and high temperature regions of the V_{OC} - T curve.

For the phototransistor, equation 82 is equivalent, but equation 84 becomes independent of the photocurrents [63]. In equation 86, which is valid for the phototransistor behavior, β denotes the gain, which is influenced by L^e and the base width:

$$V_{OC} \approx \frac{E_a - \varphi_b^h}{q} + \frac{kT}{q} \ln \left(\frac{J_{00b}}{\beta J_{00m}} \right) \qquad (86)$$

Therefore, the phototransistor can be differentiated from the model with two independent diodes by evaluating the dependency of the V_{OC} on the photocurrent at low temperatures. As the V_{OC} was not light independent for the solar cells in both **papers II and III**, they could be better described by independent diodes. According to [41,96], where both majority and minority carrier currents into the front and rear contact were modelled by a diode-like behavior, a photocurrent-independent V_{OC} indicates high injection conditions at both contacts. Under these conditions, recombination depends on the concentration of both minority and majority carriers at the contacts instead of only the minority carrier concentration under low-injection conditions. Under high injection conditions the V_{OC} depends on the ratio of the majority to minority carrier current into the contacts, i.e. the contact selectivity as defined in [41], instead of depending on the ratio of the photocurrent to minority carrier current.
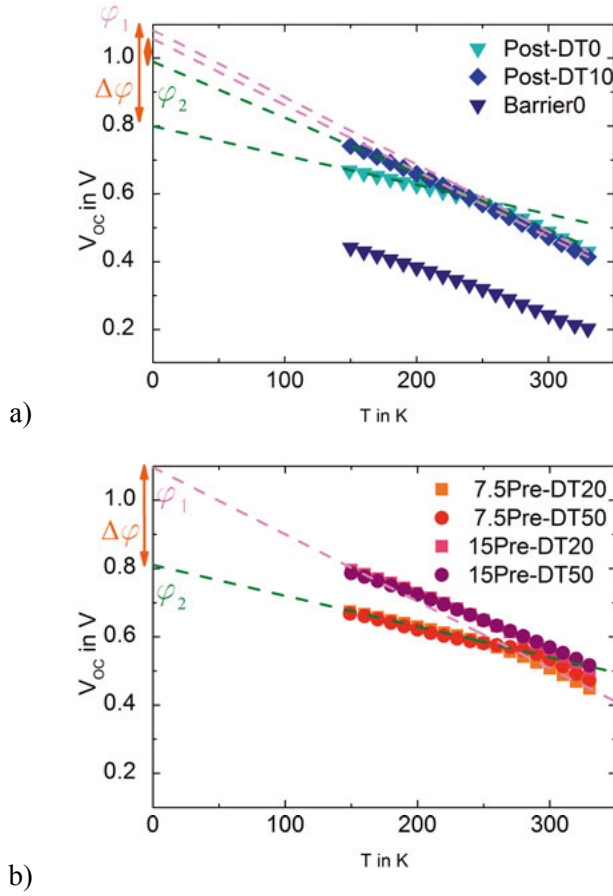
Figure 19. V_{OC}-*T* graphs for the *JVT* measurements presented in **paper III** on a) the post-DT0, the post-DT10 and the barrier0 sample and b) the pre-DT20 and pre-DT50 sample. A definition of the sample names can be found in Table 1 in chapter 4.1. In graph a) the extrapolations towards 0 K at low (150-180 K) and high temperatures (300-330 K) are illustrated for post-DT samples and the values φ_1, φ_2 and $\Delta\varphi$ are marked on the V_{OC}-axis. In graph b) the extrapolation of graphs at low and high temperatures is exemplified for the 7.5pre-DT20 sample. In both cases the green lines mark the extrapolation at low temperatures and magenta lines the extrapolation at high temperatures.

In **paper III**, (see *Figure 19*) two categories of samples can be discerned concerning the bending of the *JV* curve: the *JV* curves of the unpassivated post-DT (postDT0) sample, the barrier sample and the two 15pre-DT samples bend only slightly towards lower V_{OC} for decreasing temperatures. Contrary, the *JV* curves of the post-DT10 and the 7.5pre-DT samples bend strongly towards a much lower V_{OC} at decreasing temperatures (see chapters 4.3 and 5.4.3).

3.5 Photoluminescence

As introduced in **paper IV**, spectral PL has been used to characterize CIGS and CZTS $(Cu_2(Zn,Sn)_2(Se,S)_4)$ solar cells with and without passivation layers. Passivation layers applied on top of the absorber layer can increase the PL yield[97–99]. However, as these passivation layers have not undergone the heat-treatment and Se atmosphere during CIGS processing, they are not representative for the passivation layers at the rear contact in a substrate structure[99]. To get samples that are more representative of an actual rear contact, Joel et al.[99] built a "rear" PL structure of soda-lime glass/Mo/Al_2O_3/CIGS/CdS to be illuminated through the glass. In order to achieve transparency, these samples had an only 10 nm thin Mo rear contact. As their Al_2O_3 passivation layers were too thick and did not have openings for charge transport, the characterization of complete solar cells on these samples was not possible. To make the PL results and the solar cell characteristics directly comparable in the study leading to **paper IV**, we attempted to measure spectral PL and then to complete the solar cell processing to characterize the completed solar cells. Only recently, Salomé et al.[94] compared the PL signals measured on completed unpassivated and passivated CIGS solar cells with a 350 nm thick absorber and found a larger width of the peak for the unpassivated cells after normalization to peak height, but they were cautious and did not report intensities. Generally, PL intensities are very low, if measured on completed CIGS solar cells with a ZnO/ZnO:Al layer. As the full stack of window layers induces a much stronger electric field in the CIGS than only CdS, it separates the charges fast and efficiently as explained in [100] (in a traditional way), so that the radiative recombination rate and thus the PL intensity are strongly reduced. Therefore, we measured on the samples only with a CdS buffer layer but without ZnO/ZnO:Al window layers on the absorber.

The photon current density[23] or photon flux density[18] $dj_\gamma/d(\hbar\omega)$ per unit area and unit energy emitted from the surface of a semiconductor into the environment via radiative recombination depends exponentially on the difference of the quasi-Fermi levels according to [23]

$$dj_\gamma = A(\hbar\omega)e^{\frac{\varepsilon_{FC}-\varepsilon_{FV}}{kT}} \frac{\Omega}{4\pi^3 c^2} \frac{(\hbar\omega)^2}{e^{\frac{\hbar\omega}{kT}}-1} \, d\hbar\omega =$$

$$= A(\hbar\omega) \, e^{\frac{qV_{OCmax}}{kT}} \frac{\Omega}{4\pi^3 c^2} \frac{(\hbar\omega)^2}{e^{\frac{\hbar\omega}{kT}}-1} \, d\hbar\omega \qquad (87)$$

This equation is the Boltzmann approximated version of Planck's generalized law. The absorptance $A(\hbar\omega)$ is a characteristic of a body and a function of the body's geometry (see also chapter 2.3.2) and $V_{OCmax} = \varepsilon_{FC} - \varepsilon_{FV}$ is the maximally extractable V_{OC} for a certain minority carrier recombination rate. Ω

is the solid angle, c the velocity of light, $\hbar$ the reduced plank constant, k the Boltzmann constant and q the elemental charge. As this equation was derived with help of the Boltzmann approximation of the Fermi distribution, it is only valid for non-degenerate semiconductors. In contrast to Planck's law, however, they do not need to be black bodies and can have different Fermi distributions for electrons and holes over states, as is the case in illuminated semiconductors. As

$$e^{\frac{\varepsilon_{FC}-\varepsilon_{FV}}{kT}} = \frac{p \cdot n}{n_i^2} \tag{88}$$

dj_γ is proportional to the concentration of free charge carriers. As non-radiative recombination reduces those concentrations and the Fermi level splitting in the absorber bulk, a low PL intensity indicates high non-radiative radiation rates. A difference in V_{OC} between two samples with similar absorptance can be thus estimated from the PL intensities $j_{\gamma 1}$ and $j_{\gamma 2}$ measured at a fixed wavelength according to

$$\Delta V_{OC,PL} = \frac{kT}{q} ln\frac{j_{\gamma 1}}{j_{\gamma 2}} \tag{89}$$

The results of the PL measurements presented in **paper IV** are discussed in the chapter 5.1.

On all samples in **paper IV**, photoluminescence (PL) was measured at room temperature in a Renishaw inVia confocal Raman microscope after the CBD of the CdS buffer layer, but before the sputtering of the i-ZnO/ZnO:Al window layer. On every sample, five random measurement spots were selected and illuminated by a 785 nm continuous wave laser at a power of 0.07 µW and a spot size of about 20 µm. An InGaAs photodetector was used to measure the PL response between 0.81 and 1.55 eV. The data was integrated over the whole spectrum, which essentially consisted of a single broad PL peak centered at about 1.08 eV.

3.6 Transmission electron microscopy (TEM)

3.6.1 Sample preparation

For **papers III and IV**, TEM cross-section lamellae were prepared with a dual beam focused ion beam and scanning electron microscope (FIB-SEM, FEI Strata DB235) by the in-situ lift out technique[101]. First, a 2 µm thick Pt protective layer is deposited with assistance of the electron beam. Thereafter, the lamella is formed by removing a step profile along both of its sides with a 30 kV Ga beam controlled by a script. It is welded to a W needle by ion

deposited Pt, cut free, removed from the sample and transferred to a TEM grid. There, it is welded in place with Pt and the W needle is removed. Afterwards, the lamella is polished to electron transparency with a slightly tilted Ga ion beam. In the final step of the polishing procedure, the beam current is 50 pA and the ions are accelerated by a voltage of 5 kV. A comprehensive description of the lamellae preparation is found in [102].

3.6.2 Scanning transmission electron microscopy (STEM)

In this work, TEM was used in scanning mode. Thereby, the electron beam is focused and scanned over the lamella. From the signals of the transmitted electrons for all beam positions, the bright-field (BF) image is built. The signal of the diffracted electrons is detected by an annular dark field detector and the dark-field (DF) image is assembled. A high-angle annular dark-field image (HAADF) is produced from the signal of electrons, that are scattered incoherently and at a high angle. As these electrons are Rutherford scattered from the nucleus, HAADF is highly sensitive to variations in the atomic number Z of atoms in the sample (Z-contrast images).

3.6.3 Energy dispersive X-Ray Spectroscopy (EDX)

EDX can be used to obtain a chemical contrast in TEM. A primary electron beam is focused and scanned in STEM mode over the lamella and the energy spectrum of the emitted X-rays is detected, recorded and analyzed for every exposed point. Some primary electrons are inelastically scattered by ionizing the atoms in the lamella through ejecting inner shell electrons. X-rays with characteristic energies are emitted upon relaxation, i.e. when an electron from an outer, higher-energy shell fills the hole left by the secondary electron. As the samples for TEM are thin lamellae, the reabsorption of the X-rays can be neglected. Therefore, relative peak intensities can be used to map local compositional changes.

    For the EDX analysis in **paper IV** a probe corrected FEI Titan Themis operated at 200 kV and equipped with a SuperX system was used. The STEM-EDX spectral images were acquired and evaluated with the Esprit software by Burker.

3.6.4 Electron Energy Loss Spectroscopy (EELS)

Again, the primary electron beam is focused and scanned over the sample and some electrons inelastically scattered. The transmitted electrons are collected and sent into an energy filter. There, the Lorentz force distributes them according to their energy onto a detection plane. The spectrum consists of a high zero-loss peak, a background due to plasmon excitations and characteristic ionization edges rising from the background. In this thesis

(**paper III**), only the inner-shell ionization losses that are characteristic of each element were analyzed. The signal intensity depends strongly on the lamella thickness. A correct background subtraction is necessary for quantification. EELS works best for light elements, as the excitation edges tend to be sharp and the energy losses are experimentally accessible.

For **paper III**, the EELS data was collected using a FEI Tecnai F30ST with a Tridiem post filter (863, Gatan).

3.7 X-ray fluorescence and profilometer measurements

X-ray fluorescence (XRF) is a fast method to determine the average composition and thickness of the CIGS layer. In a PANanalytica Epsilon 5 a primary X-ray beam is directed at the CIGS layer and removes core electrons from the material. When other bound electrons relax into the empty core orbitals, X-rays with characteristic energy values are emitted. These secondary X-rays are detected in an energy-dispersive semiconductor detector. The measured peak intensities can be compared with the peak intensities of a calibration sample with known thickness and composition and the elemental concentrations and thickness of the layer can be estimated. As the samples in this thesis have thicknesses and compositions far from the standard sample, the CIGS layer thickness was additionally measured with a Bruker Dektak stylus profiler. Here, the CIGS layer is scratched away at a part of the sample and the stylus tip is physically moved along the surface and over the step. The force from the sample pushing up against the tip as it is drawn along the surface and the position of the arm are monitored.

4 Sodium and sodium fluoride

In this chapter, I present content from **papers II, III and IV**, add some background information and hopefully make it more easily accessible to the reader compared to reading the three articles. Process data can be found in the articles.

4.1 Sodium application methods

Among the multiple methods of introducing Na into the absorber layer[103], three methods have been used in this work.

1. In the baseline process, soda-lime glass substrates act as a source of Na during the CIGS co-evaporation. Thereby, the Na diffuses from the soda lime glass along the oxygenated grain boundaries of the polycrystalline Mo into the CIGS[103]. This indiffusion can be prevented by an alkali diffusion barrier, as for example a thick (here 26 nm) Al_2O_3 layer on top of the glass.

2. A thin NaF precursor layer can be evaporated on the rear surface before CIGS evaporation (pre-deposition treatment, pre-DT)[104]. Most authors report a NaF layer thickness between 10 and 20 nm. Thinner layers result in lower values of the V_{OC}, indicating a Na deficiency. Thicker layers can lead to cell degradation or delamination of the CIGS layer from the rear surface. As high concentrations of Na and F are found in the Mo layer, the Mo layer might act as a sink for Na and F during the CIGS evaporation. The effects of F onto CIGS have not been reported upon, but F has been found in the CIGS absorber at a concentration of 10^{17} compared to the Na concentration of 10^{19}[103].

3. NaF can be evaporated on top of the freshly co-evaporated CIGS layer during an anneal step under a Se atmosphere (post-deposition treatment, post-DT)[59]. Even in this case, Na reaches the rear contact[105].

Table 1. Overview over solar cell sample stacks processed for **paper III**. xx stands for the number of ALD cycles for the Al$_2$O$_3$ deposition. 10 ALD cycles correspond to 0.9 nm.

Sample type	Sample name
Post-Deposition	post-DTxx
7.5 nm pre-Deposition	7.5pre-DTxx
15 nm pre-Deposition	15pre-DTxx
Diffusion barrier	barrierxx
Baseline	baselinexx

In this work, the amount of Na(F) and the application methods have been varied in the following ways: For **paper I**, Na was supplied to all CIGS absorbers by indiffusion from the soda-lime glass substrate. For **paper II**, a NaF post-deposition treatment was used for all CIGS absorbers. For **paper III**, we studied the influence of Na(F) on Al$_2$O$_3$ rear surface passivation layers and therefore we used a variety of methods (compare *Figure 20*): a) post-deposition treatment, b) pre-deposition treatment with a 7.5 or 15 nm NaF precursor layer, c) an alkali diffusion barrier between the soda-lime glass and the Mo rear contact and d) Na indiffusion from the rear contact (referred to as baseline). The sample names can be found in Table 1. During the solar cell processing for **paper IV**, 7.5 and 15 nm NaF were applied onto the Al$_2$O$_3$ and HfO$_2$ passivation layers prior to absorber deposition.
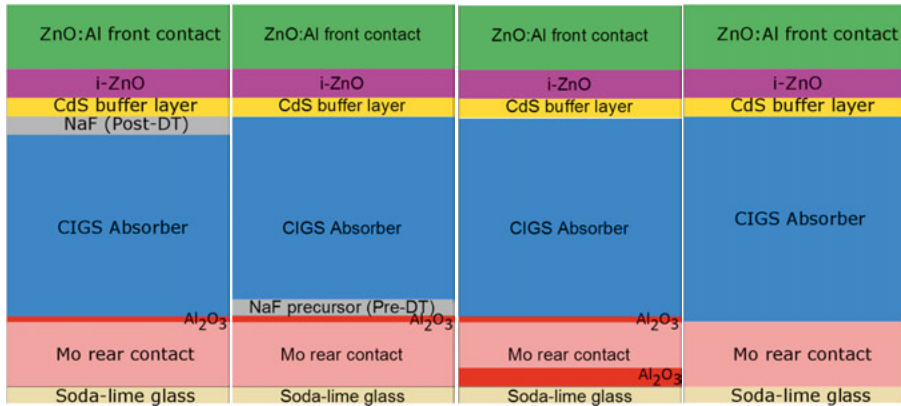
Figure 20. Schematic representation of the different sample types used in **paper III**. From the left to the right: a) NaF post-deposition treated (post-DT) b) NaF pre-deposition treated (pre-DT), c) barrier, d) baseline. The passivation layer is very thin compared to all other layers and is indicated as a red line on top of the Mo rear contact.

The amount of NaF that arrives at the samples during the post-DT is solely determined by the (constant) evaporation geometry and the amount of NaF in the crucible, as all NaF in the crucible is evaporated. To control the amount of

NaF in the crucibles accurately, NaF is first dissolved in water. Then, the crucibles are filled with a well-defined amount of the solution and dried at room temperature.

4.2 Sodium and the CIGS absorber

Na(F) is known to play a major role for the structural and electronic properties of the CIGS absorbers. Based on [103,105–107], I present a short review. Na incorporation at optimal concentrations increases the free majority carrier concentration by decreasing the number of electrically active donors dramatically, thus reducing the compensation level. A high majority carrier concentration in turn increases the Fermi level splitting, which translates into a higher V_{OC} and FF, compared to lower Na concentrations (see equations 12, 88 and 90). It also reduces the resistivity of CIGS films by one to two orders of magnitude compared to Na free films. The JV curves of solar cells with too low Na concentrations can also suffer from a roll-over effect. Too high concentrations lead to small grain sizes, porous films and low cell efficiencies. The optimum concentration depends on the Na incorporation method and the CIGS growth process, but generally lies in the order of 0.1% atom percent ($\sim 10^{19}$ atoms/cm^3). The underlying mechanism of the increase in carrier concentration is however still debated. Na can influence CIGS in four different ways: (1) if Na is present during film growth, it influences the growth process (grain size and crystal orientation) and the elemental intermixing of Ga and In, (2) Na may be built into the CIGS lattice, for example by taking Cu sites Na_{Cu} during growth [108,109] and precipitating during cool-down leaving Cu vacancies V_{Cu} behind[110], (3) Na accumulates at grain boundaries and passivates defects there, (4) Na might act indirectly, by for example influencing other parameters such as defects. The effectiveness of post-deposition treatments and the observation of higher Na concentrations in absorber regions with smaller grain size, indicate that the accumulation of Na in grain boundaries is of major importance. Effect (2) and (4) can however not be excluded. In **paper II**, we used capacitance-voltage *(CV)* measurements to determine the apparent free majority carrier concentration for the different sample types. Indeed, we found a positive correlation between the amount of Na applied, and the apparent free carrier concentration.

4.3 Sodium and the rear contact

As summarized in the introduction to **paper III**, the rear contact region is strongly affected by the presence of Na. While there is a general agreement, that Na enhances the electrical properties of the rear contact, the exact mechanism is unclear. For example, according to[60,104] a roll-over

measured on Na-free devices at room temperature can be reduced by a NaF pre-deposition treatment. Pre-deposited Na[104] or Na from the soda-lime glass acts as a catalyst and promotes the formation of $MoSe_2$, which in turn creates an ohmic contact[67,111,112]. In contrast, Yoon et al.[113] doubt that the $MoSe_2$ layer is the origin of the ohmic nature of the rear contact. They suggest that Na reduces the hole barrier at the $CIGS/MoSe_2$ interface as it increases the (effective) doping and thus the majority carrier concentration in the CIGS or the $MoSe_2$ layer. Umehara et al.[114] found a kink and roll-over in the JV curves and a disadvantageous band-bending for hole transport towards the rear contact when they simulated $Ag(In,Ga)Se_2$ solar cells, although they modelled an ohmic $MoSe_2/Mo$ contact without a hole barrier in the dark. Increasing the majority carrier concentration (by a Na post-deposition treatment), reduced the kink and roll-over in both the simulated and the fabricated solar cells. Jarzembowski et al.[115] observed that the rear surface recombination velocity for samples with an alkali diffusion barrier is lowered by NaF post-deposition treatment. They concluded that Na reduces the defect concentration at either the $MoSe_2/CIGS$ interface or the $MoSe_2/Mo$ interface.

NaF precursor layers have been widely used on Al_2O_3 passivation layers without any intention to ensure unimpeded current transport and without any intentions to change the properties of the $Al_2O_3/CIGS$ interface[12,82,94,116–118]. Only in rare cases have Al_2O_3 rear contact reflection/passivation layers been implemented into CIGS solar cells without any extra Na added [81,119] or NaF being added after CIGS deposition (post-deposition treatment)[89,119]. In contrast, the electronic properties of $Al_2O_3/CIGS$ interfaces have been investigated without taking the influence of heat-treatment of the Al_2O_3 layer in presence of Na(F) (and Se) into account. The Al_2O_3 layers were either deposited on top of the CIGS layer or a NaF precursor was not used, if the CIGS was co-evaporated on top of the Al_2O_3 layer[91,99,119,120].

We showed that NaF precursor layers allow unimpeded current transport through unpatterned ALD-Al_2O_3 rear surface passivation layers and decrease the photoluminescence intensity of glass/ALD-Al_2O_3/CIGS/CdS stacks with increasing NaF layer thickness (**papers III and IV**). Therefore, the results from the previous studies might need to be revisited. No such effects of NaF were found for HfO_2 passivation layers (**paper IV**).

Furthermore, an analysis of the dependence of the V_{OC} on T indicates that a thicker NaF precursor layer lowers the height of the hole barrier at Al_2O_3 passivated rear surfaces (**paper III**). The method can however not distinguish between whether that hole barrier is a barrier at a $CIGS/Mo(Se_2)$ contact in possible openings of the Al_2O_3 layer or whether the barrier is associated with current transport through the Al_2O_3 layer, as for example in Frenkel-Poole emission. Transmission electron microscopy (TEM) analysis suggested that

openings have been formed in the Al_2O_3 layer, so that it is most likely the barrier at the CIGS/Mo(Se$_2$) contact that is reduced by the NaF treatment.

5 Rear surface passivation with metal oxides

In this chapter, I present material from **papers II, III and IV**, add some background information and hopefully make it more easily accessible to the reader compared to reading the three articles.

5.1 Passivation materials

5.1.1 ALD-Alumina

A large variety of oxides have been studied as passivation or reflection layers in CIGS solar cells, namely for example TiO_2[119], SiO_2[79,121,122] and ZnO [123] at the rear surface and Ga_2O_3[85], Al_2O_3[84], SiO_x and Si_3N_x [124] at the front surface. The most commonly investigated rear surface passivation layer material is Al_2O_3 though. It has been shown to increase solar cell efficiencies for both c-Si and CIGS solar cells. Thin (<15 nm) Al_2O_3 passivation layers mostly increase V_{OC} by lowering the recombination rate at the rear surface[118]. Both, thicker Al_2O_3 layers (30 nm)[12] and Mo nanospheres[82] also increase the J_{SC} by increased reflection at the rear surface and/or by absorption-enhancing phonons between Mo nanospheres. The electrical passivation effect increases strongly from 5 to 50 nm passivation layer thickness[120]. Both its oxide charge and the reduced interface trap density[91,120] are seen as responsible for its efficiency. Both a negative and positive charge[91,120,124] have been observed in Al_2O_3 layers deposited by ALD on top of CIGS. In the latter case the oxide charge can become negative after an anneal[91,125]. As the Al_2O_3 layer also gets heat-treated during CIGS deposition, it probably has a negative charge as a rear surface passivation layer. The negative oxide charge is attributed to negatively charged centers (aluminum vacancies V_{Al} and/or oxygen interstitials O_i) in oxygen rich Al_2O_3 layers.

In the study published in **paper III**, J_{ph} is increasingly blocked in solar cells samples that have > 1 nm thick Al_2O_3 rear passivation layers and either have an alkali diffusion barrier or were NaF post-deposition treated (see *Figure 21*). In contrast, if 7.5 or 15 nm NaF precursor layers are deposited onto the Al_2O_3 rear passivation layers prior to absorber deposition, no such blocking can be observed up to 6.3 nm passivation layer thickness. For even thicker Al_2O_3

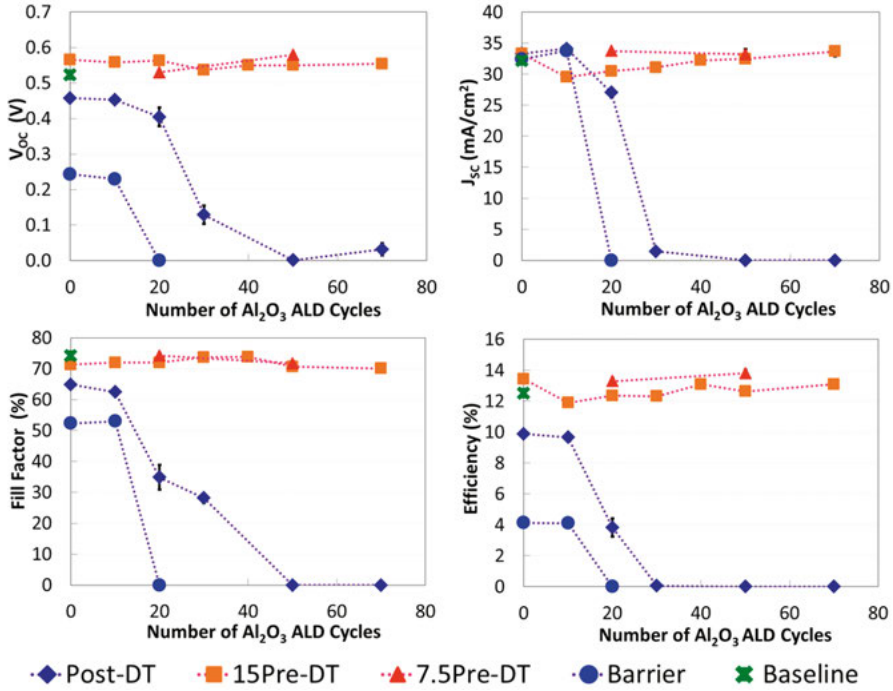layers the CIGS layer peeled from the passivation layer during chemical bath deposition (CBD).

Figure 21. Average open-circuit voltage V_{OC}, short-circuit current density J_{SC}, fill factor *FF* and efficiency for all sample types. The error bars indicate the standard deviation σ, which is in most cases smaller than the marker and thus not visible.

In our study presented in **paper IV**, we showed with the help of PL measurements that Al_2O_3 rear surface passivated CIGS solar cells have a large potential to achieve high values of V_{OC} (+170 mV compared to an unpassivated reference), but also that the potential gain in V_{OC} as estimated from the PL intensities is reduced to 100 mV if the thickness of a NaF precursor layer is doubled from 7.5 nm to 15 nm (*Figure 22*). Unfortunately, 15 nm NaF precursor layers are necessary to ensure sufficiently unimpeded current transport through the 6 nm thick ALD-Al_2O_3 layers in the solar cells processed from the same samples. Fortunately, even the lower-quality passivation achieved is beneficial for the ultra-thin CIGS solar cells processed from the samples used for the PL measurements: apart from an increase in V_{OC} (+120 mV), it also increases the J_{SC} (+6 mA/cm^2) and thus the efficiency significantly (+3%) (*Figure 23*). Additionally, it decreases the number of strongly shunted cells (*Figure 23*) and decreases the apparent shunt conductance dJ_{light}/dV under illumination (see *Figure 27*). The theory for the shunt-behavior can be found in chapter 3.3 and the results in discussion in chapter 5.4.4.We cannot exclude that the observed effects of NaF only happen

in ALD deposited Al_2O_3, which involves the use of a metal-organic precursor, and not for example in sputtered Al_2O_3.
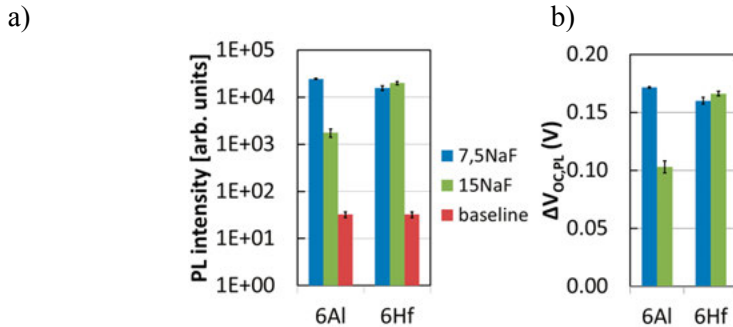
a)

b)

Figure 22. a) Photoluminescence (PL) intensities for the investigated samples in **paper IV**. 7.5NaF and 15NaF denotes the samples that had a 7.5 and 15 nm NaF precursor deposited onto the rear contact prior to CIGS co-evaporation. b) Estimated open-circuit voltage gains $\Delta V_{OC,PL}$ of the passivated samples compared to the baseline reference calculated from the PL intensities.

Passivation with Al_2O_3 layers with NaF on top might thus be the best choice, if expensive and time-consuming patterning steps are to be avoided. In this case, Na(F) precursor deposition needs to be used (which does not exclude other additional Na application methods), and a compromise between conduction through the Al_2O_3 layer, passivation effectiveness of the Al_2O_3 layer and beneficial and detrimental effects of Na on the absorber needs to be found.

Nanopatterned Al_2O_3 layers will not only enable thicker Al_2O_3 layers and thus a slightly higher reflectance of the rear surface, but probably make above mentioned optimization easier. If patterning is used, NaF does not need to be applied to ensure conduction through the passivation layer and other Na application methods can be used that impact the passivation quality less than NaF precursor deposition. Then, the optimization tasks are split between the patterning method and the Na application method. The patterning method has to be optimized for both conduction and passivation effectiveness. The optimal Na application method and concentration then only need to minimize the negative effect of NaF on the passivation effectiveness and optimize the Na content in the absorber. However, a compromise between these two parameters might still be necessary. In addition, the patterning will determine the amount of Na diffusion through the Al_2O_3, so that the problem might be hard to solve, unless an alkali-diffusion barrier is used on soda-lime glass. Any dependency of Al_2O_3 characteristics on NaF might thus be of disadvantage if the layer is patterned in an extra fabrication step and the large passivation potential of Al_2O_3 might never be fully exploited.
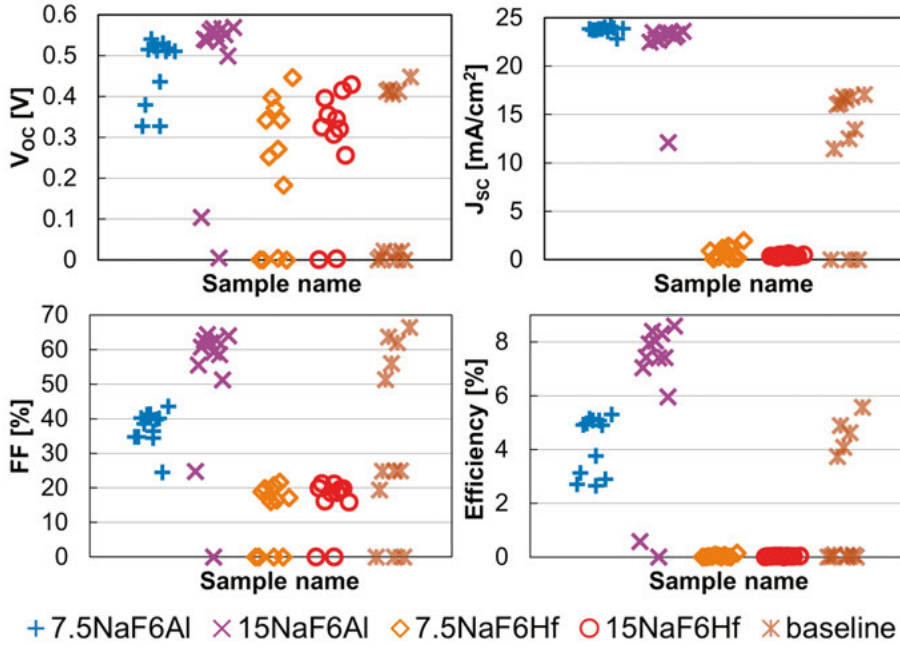
Figure 23. **Paper IV**. Solar cell parameters short-circuit current density (J_{SC}), open-circuit voltage (V_{OC}), fill-factor (*FF*) and efficiency for all 12 cells on all samples. The Al_2O_3 and HfO_2 rear surface passivation layers were deposited by ALD to a thickness of 6 nm. A 7.5 or 15 nm thick NaF precursor layer was evaporated onto the passivated rear surface prior to absorber co-evaporation. The samples are referred to according to their passivation and precursor layer thicknesses as "baseline reference", "7.5NaF6Al", "15NaF6Al", "7.5NaF6Hf" and "15NaF6Hf", respectively.

5.1.2   ALD-Hafnia

Hafnia (HfO_2) has been considered as a material for passivation layers in solar cells, as for example c-Si solar cells[125–129] and organic solar cells[130], and recently even for front surface passivation in CIGS solar cells[124]. It has a higher refractive index of 2.09 compared to 1.66[131] for Al_2O_3. Its band gap is 5.3 eV compared to 6.5 eV for Al_2O_3 and its valence band edge energy is 0.83 eV higher and its electron affinity 0.43 eV larger compared to Al_2O_3[132]. The effectiveness of HfO_2 passivation layers on crystalline Si (c-Si) and the sign of its charge depend on several factors, like on the cleaning method[129], ALD precursor, process and temperature[129], the post-deposition annealing method[125] and also on illumination[129]. Therefore, the passivation properties of HfO_2 as passivation layer in CIGS solar cells could not be deducted from the existing literature. This gap in knowledge motivated **paper IV**.

   Based on the results of the PL measurements in **paper IV**, solar cells with a patterned HfO_2 rear surface passivation layer can be expected to have high

V_{OC} values (+160 mV compared to an unpassivated reference) (*Figure 22*). As no dependencies of the passivation effectiveness and conduction on NaF have been observed for HfO_2 layers in the study presented in **paper IV** (*Figure 23*), it might be the passivation material of choice, if conduction through the HfO_2 layer is obtained by an extra fabrication step such as nanopatterning. Good surface passivation properties are then ensured independently of the Na incorporation method and concentration and no compromise concerning these is needed. Conduction through the passivation layer and passivation effectiveness can be optimized by the nanopatterning method, and independently of the optimization of the Na application method to achieve good electrical absorber properties.

5.2 Current transport through the passivation layer

5.2.1 Nanopatterning (partial rear contact)

As all the oxide passivation layers mentioned are electric insulators, they are usually nanostructured when used as a passivation layer. On CIGS solar cells the nanostructures include point contacts and line contacts[81,133]. Mo nanoparticles forming at contacting points[82], electron-beam lithography[89,118], photo-lithography[79,81,133], laser-interference lithography[121] and nanoimprint lithography[119] have been used to open up the passivation layers. Nanosphere shaped CdS particles precipitated during a CBD[12,116,117] have been used in lift-off processing. A self-organized spray-pyrolysis process has also been applied to deposit porous Al_2O_3 onto a transparent SnO_2:F rear-contact[134]. The passivation layers in **paper II** were opened up by electron-beam lithography in combination with reactive ion etching as described in [11] and in chapter 1.3.

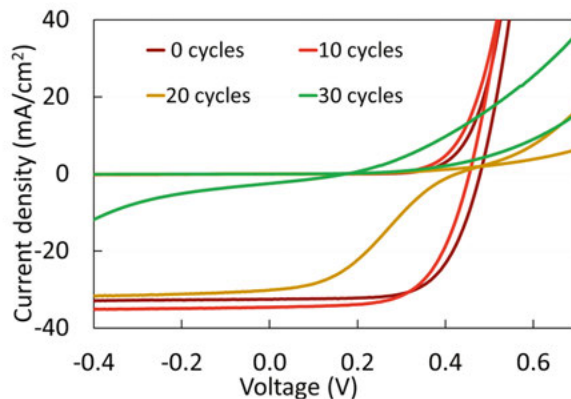## 5.2.2 Tunneling or pinhole assisted current transport

Figure 24. **Paper III**. Current density -voltage (*JV*) curves (left) in the dark and under illumination for selected post-deposition treated (post-DT) samples with different ALD-Al_2O_3 thicknesses. 1 ALD cycle corresponds to 0.9 Å.

Above listed nanopatterning processes require several additional fabrication steps and increase production cost. In our study for **paper III**, we wanted to find out if the rear surface could be effectively passivated without these additional steps. More specifically, we wanted to know if there exist Al_2O_3 thicknesses that on the one hand allow sufficiently high tunneling currents or currents through pinholes and on the other hand still have a sufficient passivation effect. This type of contact is known as metal-insulator-semiconductor (MIS) contact in device physics[135–138]. We introduced Al_2O_3 rear surface passivation layers with thicknesses between 0.9 and 27 nm into solar cells. We found, that J_{ph} is blocked by Al_2O_3 rear surface passivation layers deposited by more than 10 ALD cycles (~0.9 nm) if no NaF precursor layer is used (see *Figure 24*) (post-deposition treated samples and samples with a diffusion barrier). Although the 0.9 nm thin Al_2O_3 layers increase the J_{SC}, they do not increase the solar cell efficiency either due to a lower *FF* and/or due to a lower V_{OC}. For samples with Al_2O_3 deposited by 20 ALD cycles (~1.8 nm), the *JV* curve has a kink and roll-over, indicating that both, hole injection and extraction by the rear contact, are blocked. For even thicker Al_2O_3 layers, J_{ph} is increasingly blocked, so that the device mostly acts as a resistor. This result can be interpreted as φ_I increasingly reducing the carrier transmission coefficient in equation 58.

Similarly blocking *JV* curves have been measured on solar cell samples, which were passivated with a < 5 nm thick Al_2O_3 passivation layer from the same ALD process without contact openings and were produced on soda-lime glass and without extra Na supply[12]. The authors concluded that their measured *JV* curves disprove a sufficient contact through the passivation layer and indicate that the passivation layer is intact. For solar cell samples with a

front surface passivation layer, a thickness of about 1 nm is the maximum thickness that still allows for negligible current losses, either due to sufficiently high tunneling currents[84] or currents through pinholes. The series resistance increases significantly for solar cells with 1.7 nm thick passivation layers compared to solar cells on a reference sample. For solar cells with a 2.2 nm thick passivation layer, the light JV curve has a kink and roll-over. In agreement with these references, we concluded that the passivation layer for the post-deposition treated samples and the samples with an alkali diffusion barrier are completely covering after CIGS processing for more than 20 ALD cycles, i.e. 1.8 nm.

5.2.3 NaF assisted current transport
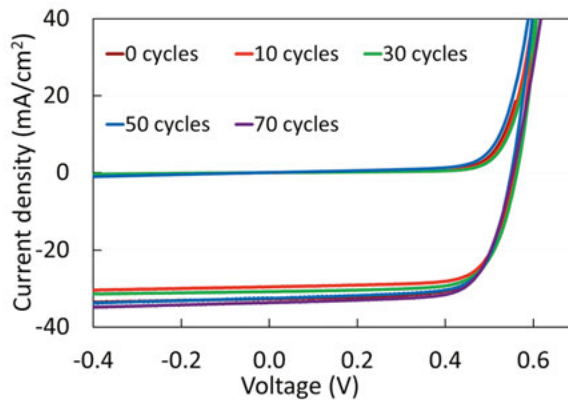
Figure 25. **Paper III**. Current density-voltage (*JV)* curves in the dark and under illumination for selected samples with a 15 nm NaF precursor layer (15PreDT samples) and different ALD-Al_2O_3 passivation layer thicknesses. One ALD cycle corresponds to 0.9 Å.

Whereas the effects of Na(F) on CIGS absorbers were well known (even if not completely explained) when I started my work on rear surface passivation, its effects on passivation layers had not been studied in detail. Vermang et al.[12,116] had concluded that 2 and 5 nm thick Al_2O_3 rear surface passivation layers do not conduct sufficient current in the completed solar cells and that point contacts are required in the passivation layers, by comparing rear surface passivated samples without NaF precursor and without nanopatterning with a rear surface passivated samples with NaF precursor and nanopatterning. They did not report any results from samples with both unpatterned Al_2O_3 layers and a NaF precursor, motivating us to have a look at this combination in our study for **paper III**.

 We showed in **paper III** (and later in **paper IV**) that using a NaF precursor layer on top of < 7 nm thin Al_2O_3 rear surface passivation layers can increase the conduction through the Al_2O_3 layers sufficiently to make the extra

fabrication step of opening up the passivation layer unnecessary (see *Figure 25*). Therefore, the assumption that intentionally patterned Al_2O_3 passivation layers conduct current only via the point contacts needs to be reconsidered. Al_2O_3 passivation layers, that were deposited by the same ALD process to similar thicknesses and intentionally patterned either by nanoparticles [12,118] or electron-beam lithography [82] and had a NaF precursor applied onto them before the CIGS evaporation, probably do not conduct current only through the intentional contacts. On the other hand, we had already shown in **paper II** that post-DT solar cells with 27 nm thick Al_2O_3 passivation layers that were patterned by electron-beam lithography with a similar pitch and contact area are sufficiently conductive (**paper II**).

5.2.4 The unsolved riddle: How do NaF precursor layers enhance current transport through and the passivation effectiveness of ALD-Al_2O_3 layers?

The increase in conduction and decrease in passivation effectiveness of Al_2O_3 passivation layers due to the use of a (thicker) NaF precursor layer raises the question how a NaF precursor modifies the rear contact region. In **paper III and IV**, we proposed two hypotheses on how the NaF precursor alters the current transport through the Al_2O_3 layer and the passivation effectiveness: 1) It opens up holes in the Al_2O_3 and a $MoSe_2$ layer is formed between the Mo and CIGS layer, so that the current transport occurs from the CIGS to the Mo via the $MoSe_2$ layer. These openings are probably areas with a higher recombination rate. The recombination rate at a solar cell's rear surface is then a weighted average recombination rate of the Al_2O_3 passivated rear surface area and the unpassivated area of the nanocontacts. 2) Chemical changes in the Al_2O_3 passivation layer due to the presence of Na and/or F could enhance the conductivity and/or oxide charge. For example, it has been shown that oxygen vacancies V_O in AlO_x can form a defect band close to the band edge, which acts as a "conduction band"[139]. A quasi-conduction band consisting of a wide range of defect states has also been observed in $LaAlO_3$[140]. Doping can also introduce traps that increase the likelihood for Frenkel-Poole emission, which is a trap-assisted carrier transport mechanism[141]. The proposed traps/quasi-conduction band would have to either compensate the negative oxide charge or increase the interface trap density to enhance both the conductivity and decrease the passivation effectivity simultaneously.

Whereas we could collect some indications that point to hypothesis 1 in our studies, we have been unable to rule out hypothesis 2. The two hypotheses do however not exclude each other. It is for example possible that the openings provide for conduction, but that the passivation effectiveness is additionally reduced by changes in the oxide charge or interface defect density. In this case, NaF precursor layers would have a negative effect even on the passivation

quality of thick Al_2O_3 layers, which block the current transport completely regardless of a NaF precursor layer.

5.2.4.1 Temperature dependent current density-voltage measurements (paper III)

If we assume that there are openings in the Al_2O_3 layer for the pre-deposition treated samples (hypothesis 1), the measured $\Delta\varphi$ is an estimate of φ_b^h at the CIGS-MoSe$_2$ interface. If the openings in the Al_2O_3 layer were large enough, the band bending at the CIGS-MoSe$_2$ interface would not be affected by the oxide charge. Even though the oxide charge increases with Al_2O_3 layer thickness[120], φ_b^h would not depend on the thickness of the passivation layer. Indeed, our results do not show any correlation between $\Delta\varphi$ and the passivation layer thickness.

According to the literature[104,113] the contact resistance, φ_b^h and the likelihood for a roll-over in a temperature range between 100 and 300 K decreases for higher Na concentrations at CIGS-MoSe$_2$ interfaces. $\Delta\varphi$ is indeed 0.2 eV lower for the 15preDT20 and the 15preDT50 sample compared to the 7.5PreDT20 (and 0.3 eV lower compared to the 7.5PreDT50 sample, which had however degraded; for the definition of sample names see Table 1). In summary, our results do not contradict hypothesis 1.

The current blocking for the post-DT samples with more than 2 nm thick Al_2O_3 layers indicate that the direct tunneling of holes and current transport through pinholes can be excluded for these Al_2O_3 layers and that the energy barrier φ_I associated with an assumed current transport through the Al_2O_3 layer via traps or a quasi-conduction band is too large to be overcome. The carrier exchange coefficient in equation 58 has become too low. According to hypothesis 2 then, Na or F doping lowers φ_I. However, the *JVT* measurements probe the largest hole barrier in the valence band at the rear contact and cannot per-se distinguish the hole barrier associated with the Al_2O_3 layer from the one associated with the band bending in the CIGS. If Na or F doping reduces the former below the latter, the latter will be detected and changes in barrier height will be changes in band bending. Yoon et al[113] proposed that Na directly reduces the hole barrier height at the CIGS-MoSe$_2$ interface by increasing the carrier concentration in the CIGS or MoSe$_2$, and not indirectly by enhancing the formation of MoSe$_2$. Even this effect can explain our results. In conclusion, the *JVT* measurement cannot distinguish between the two hypotheses, conduction through openings in the passivation layer or an increase in conductivity due to a change of the electrical properties of the passivation layer.

5.2.4.2 X-ray photospectroscopy (XPS)

In the course of a Master thesis project in our group[142], X-ray photospectroscopy (XPS) was used to confirm hypothesis 1. MoSe$_2$ is probably formed in the holes of a locally non-covering passivation layer,

whereas no MoSe$_2$ is formed on a closed passivation layer. Thus, detecting MoSe$_2$ would indicate that the passivation layer is not closed. The XPS analysis could however not confirm the existence of MoSe$_2$ on samples with a NaF precursor layer on a Mo-coated glass substrate with an Al$_2$O$_3$ layer, which had been annealed in a Se atmosphere and in vacuum as a reference. This result neither excludes nor confirms hypothesis 1. A possibility to verify hypothesis 2 is to prove the existence of other Al-compounds than Al$_2$O$_3$ at the rear contact. However, when comparing annealed glass-Mo-Al$_2$O$_3$ stacks with and without a NaF precursor on top, the existence of an additional chemical shift in the Al signal for the samples with NaF could not be verified. Especially, AlF$_3$ signals could not be distinguished from the Al signals. This result neither confirms nor contradicts hypothesis 2.

5.2.4.3 TEM, EELS (paper III)

The TEM and EELS analysis in **paper III** confirmed a conformal Al$_2$O$_3$ layer growth but Ga is incorporated into the oxide layer, apparently as GaO$_x$, regardless if NaF was supplied before or after CIGS evaporation. If a NaF precursor layer is applied on top of the Al$_2$O$_3$ layer, the layer deteriorates at some locations, probably leading to direct contact between the CIGS absorber layer and the Mo rear contact. In such locations the intensity of the Mo signal drops consistently more gradually, which can indicate a formation of MoSe$_2$. If NaF is supplied in a post-deposition treatment, the integrity of the oxide layer is preserved, even though GaO$_x$ is formed. This result is evidence for hypothesis 1 but does not exclude hypothesis 2.

5.2.4.4 TEM, EDX (paper IV)

The TEM and EDX data presented in **paper IV** confirms that both the Al$_2$O$_3$ and HfO$_2$ layers are generally conformal. Areas that could be interpreted as openings are visible in all passivation layers, also in the HfO$_2$ ones, although these should be closed according to the *JV* analysis of the solar cells. While the analysis in paper III was done on very thin lamellae, the lamellae in **paper IV** were probably thicker. Thus, the surface/interface roughness made the interpretation of the data more difficult. In conclusion, we were not able to use this TEM work neither to support nor contradict hypothesis 1 or 2.

5.3 CIGS solar cells with a high band gap absorber

This chapter is based on **paper I and II**. Grading the *GGI* of the absorber reduces the surface recombination rate and thus solar cell efficiencies[10,143]. For both single and double graded absorbers, a high *GGI* is used at the rear contact. For single graded absorbers, a small *GGI* is used at the front contact and the *GGI* is continuously varied between the two extremes. For double graded absorbers, the *GGI* decreases towards a minimum and increases again

towards the front contact. The *GGI* at the rear contact in both single-graded and double-graded solar cells is often in the order of 0.6[144]. A better understanding of both, the bulk properties of high Ga CIGS and the rear surface passivation of absorbers with high *GGI* at the rear contact, might help to optimize Ga graded solar cells with or without an additional passivation layer. A high *GGI* increases the band gap of CIGS by elevating mostly the conduction band edge. A discussion of the underlying passivation mechanism is provided in chapter 2.4. Moreover, a high Ga content also implies a low In content, In being more pricy and more limited in supply than Ga[4].

In **paper I** we studied a two-dimensional matrix of solar cells with absorber layers without Ga grading and with a *GGI* ≈ 0.15, 0.30, 0.45 and 0.60 and a thickness of 0.5, 1.0 and 1.5 µm. Neither NaF nor any rear surface passivation was used. The samples with a *GGI* ≈ 0.60 showed nearly identical *EQE* curves for CIGS thicknesses of 1.0 and 1.5 µm even for long wavelengths, while the *EQE* increased for all wavelengths with increasing d_a for all other values of the *GGI* (see *Figure 26*). As the generation rate (see chapter 2.3.2) is not reduced accordingly for photons with energies close to the band gap energy, it is the collection function that is very low close to the rear surface for these high Ga absorbers (see chapter 3.1). Recombination at the rear surface should play a smaller role for thicker absorbers and thus not be responsible for the reduction in *EQE* for the 1.5 µm absorber. Therefore, a short collection length ($L_{QNR} + d_w$; see chapter 2.3.2) for the samples with a *GGI* ≈ 0.60 was proposed in **paper I**.

A hypothesis was that by changing d_a, only the generation function and the recombination rate at the rear contact would be changed, and not the defect density in the bulk. We hoped that we therefore would be able to distinguish the influence of recombination in the space charge region and the bulk from the influence of recombination at the rear surface on the collection function. We also aimed at quantifying the recombination rate at the rear contact for these unpassivated samples, but also later for a similar series of passivated samples. The solar cells were modelled with the numerical solar cell simulation tool SCAPS [145] and with an *EQE* simulation tool applying the collection function derived in [33]. Absorption coefficient data from both literature[146–148] and data derived from own reflection and transmission measurements on thin films on glass were used. The simulation results showed that differences in generation and the rear contact recombination rate cannot explain the low *EQE* and J_{SC} for solar cells with 0.5 µm thin absorbers compared to the solar cells with thicker absorbers. There must exist additional recombination centers in these thin solar cells to explain the results. The simulation results have not been published and the idea of quantifying the contributions abandoned.

When I joined the research group, the rear surface passivation of absorber layers without Ga grading and with a low *GGI* ≈ 0.3 was studied [12,82,118] and no studies had been done yet for high values of GGI. Considering the

results in **paper I**, we hypothesized that a passivation effect would not be observable for solar cells with 1.5 µm thick absorber layers with a $GGI \approx 0.60$ (**paper II**). Furthermore, we wanted to verify that the collection length and not the rear surface recombination reduces the collection function at the rear surface. Therefore, both passivated and rear surface passivated solar cells with similar d_a as in **paper I** were produced and compared with each other. To our surprise, a passivation effect could be discerned from the *IQE* data even for the 1.50 µm thick absorbers (see chapter 5.4.1).
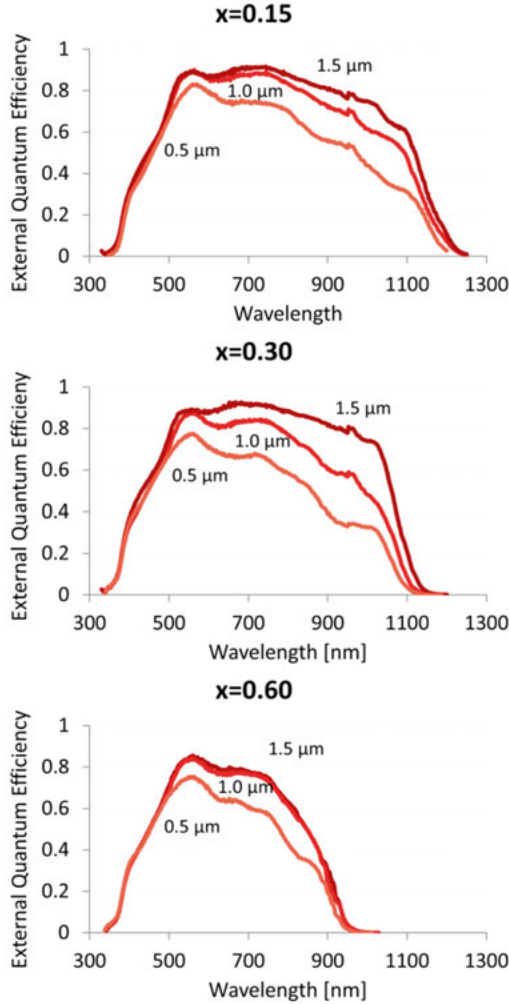
Figure 26. **Paper I**. External quantum efficiencies (*EQE*) of CIGS solar cells with absorbers with values of $x =: GGI \approx 0.15, 0.30, 0.60$ and absorber thicknesses d_a of 0.5, 1.0 and 1.5 µm.

5.4 The effect of passivation layers at the rear surface on the device properties

5.4.1 Fill factor, external quantum efficiency and short-circuit current density

In addition to increasing V_{OC}, the surface passivation can increase the J_{SC}/EQE, as fewer charge carriers recombine at the rear surface and more charge carriers are collected at the contacts. A reduction of the fill-factor (and eventually even the V_{OC}, see chapter 2.4) is expected, if

1. the resistance for the hole transport towards a contact opening is large (spreading resistance)[149–156]
2. the specific contact resistance at the contact openings is large
3. the resistance of the Al_2O_3 layer is large (if no contact openings exist).

On the other hand, an increase in V_{OC} should also lead to an increase in FF according to[23]

$$FF = \frac{\frac{qV_{OC}}{AkT} - ln\left(1 + \frac{qV_{OC}}{AkT}\right)}{1 + \frac{qV_{OC}}{AkT}} \qquad (90)$$

In this work, the fill-factor did not change significantly, neither for the high band gap solar cells with nanopatterned Al_2O_3 rear surface passivation layers (**paper II**), nor for the solar cells with unpatterned Al_2O_3 rear surface passivation layers, if sufficiently thin Al_2O_3 layers and sufficiently thick NaF layers were used.

In **paper II**, i.e. for the high band gap solar cells, the passivation effect could only be discerned with the help of the IQE data, although the efficiencies of the passivated samples exceed those of the unpassivated references by 1.1 to 1.6 % (absolute), as the gains in V_{OC} were lower compared to gains in the literature for similar, but not identical sample stacks[12,116–118]. In **paper III**, the efficiency of the passivated samples did generally not exceed the efficiency of the unpassivated samples for 1 μm thick absorbers (*Figure 23*), but a small passivation effect could still be discerned by comparing the EQEs of the samples with different passivation layer thicknesses within one sample type. Finally, in case of the ultra-thin cells (**paper IV**), we attributed most of the gain in efficiency of 3% (absolute) to the passivation effect (compare *Figure 27*).

Five effects can be responsible for differences in EQE for different solar cells: differences in the absorptance A_a (see chapter 3.1), differences in

recombination rate at the front contact, differences in d_w with $\eta_C \approx 1$, differences in L_{QNR} in the quasi-neutral region and/or differences in the recombination rate at the rear surface. Generally, no intentional optical or electronic differences have been introduced at the front surface of the absorber between the passivated samples and the unpassivated references. In **paper II**, all samples were post-deposition treated. In **paper IV**, none of the samples were post-deposition treated. Therefore, a similar surface recombination rate at the front contact can be expected for both the passivated samples and the unpassivated reference samples in **papers II and IV**, and also within a sample category in **paper III**.

On the other hand, larger concentrations of Na in the absorber increase the net acceptor concentration and shorten d_w. The Na concentration also influences L_{QNR} and Na post- and pre-deposition treatment are not equal in their effects on the absorber, as Na is present during crystal growth in the latter case but not in the former (see chapter 4). Therefore, the *EQE* of different samples can only be compared in a straightforward manner, if the same Na supply methods and concentrations have been used.
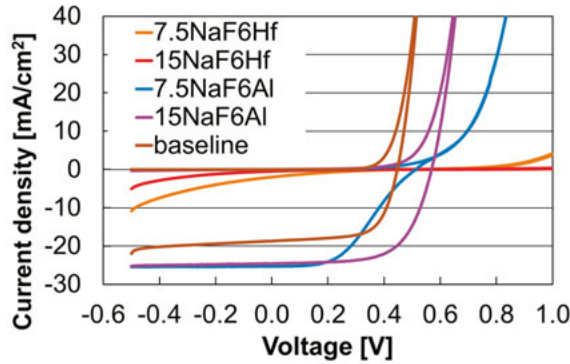

Figure 27. Dark and light current density-voltage (*JV*) curves for the best cell of each sample in **paper IV**. The Al_2O_3 and HfO_2 rear surface passivation layers were deposited by ALD to a thickness of 6 nm. A 7.5 or 15 nm thick NaF precursor layer was evaporated onto the passivated rear surfaces prior to absorber co-evaporation. The samples are referred to according to their passivation and precursor layer thicknesses as "baseline reference", "7.5NaF6Al", "15NaF6Al", "7.5NaF6Hf" and "15NaF6Hf", respectively.

In **paper II**, the Na concentration might be larger for the unpassivated references than for the passivated samples, as they were both subjected to a post-deposition treatment and Na indiffusion was inhibited only in the passivated samples by the 26 nm thick Al_2O_3 passivation layer. As a lower Na concentration corresponds to a lower net acceptor concentration, the increase in *EQE* for the passivated samples (see *Figure 28*), can be partially explained by a larger d_w. The lower net acceptor concentration is also detrimental to the V_{OC} according to [18]

$$\Delta V_{OC} \approx \frac{AkT}{q} ln \ \left(\frac{N_{A,pas}}{N_{A,ref}} \right) \tag{91}$$

where $N_{A,pas}$ and $N_{A,ref}$ are the net acceptor concentration of the passivated and the reference solar cells, respectively. Therefore, gains in V_{OC} due to the passivation effect are probably counteracted by losses in V_{OC} due to the lower acceptor concentration and converted into gains in J_{SC} (see *Figure 28* and Table 2).

For the ultra-thin solar cells in **paper IV**, Na was supplied via diffusion from the glass for the baseline reference and via a NaF precursor for the passivated samples, but Na indiffusion probably still happens for 6 nm thin passivation layers.
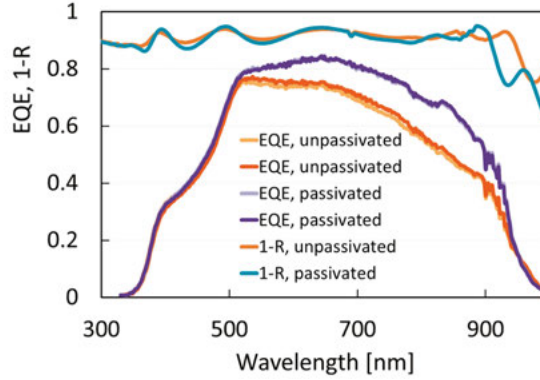
Figure 28. Solar cells with a high band gap absorber with a $GGI \approx 0.60$ from **paper II**. *EQE* for two devices per sample and *1-R* (1-reflectance) of the complete solar cell stack for the samples with a 1.45 μm thick absorber layer.

The five effects can be in some cases distinguished, as they impact the *EQE* in different wavelength regions. Front surface recombination reduces the *EQE* at all wavelengths[54] (compare also *Figure 13*). A higher reflection at the rear surface enhances especially the absorption of photons with long wavelengths, as photons with short wavelengths have a high absorption coefficient and are to a large degree already absorbed before they reach the rear surface.

Table 2. Solar cells with a high band gap absorber with a $GGI \approx 0.60$ from **paper II**. Summary of solar cell parameters (arithmetic average ± standard deviation).

Absorber thickness d_a in μm	Passi-vation	V_{oc} in V	J_{sc} in mA/cm²	Fill factor in %	Efficiency in %
0.6	yes	0.732±0.003	18.8±0.5	68±3	9.3±0.5
0.6	no	0.709±0.004	15.6±0.2	69±1	7.7±0.2
0.85	yes	0.721±0.010	20.0±0.2	69±0	9.9±0.1
0.85	no	0.727±0.003	17.6±0.2	69±1	8.8±0.1
1.45	yes	0.747±0.004	22.9±0.7	70±1	12.0±0.4
1.45	no	0.718±0.010	20.7±0.3	71±1	10.5±0.1

Whether the passivation effect increases the *EQE* only for long wavelengths or evenly for medium to long wavelengths depends on the relations between the L_{QNR}, w_a and d_a (see chapter 2.4). Light with a long wavelength creates free electrons closer to the rear surface. Thus, the collection probability and the *EQE* for these free electrons is reduced, if the recombination rate at the rear surface is large or if L_{QNR} is small compared to d_a. If the space charge region reaches far back into the CIGS layer, the influence of the rear surface recombination and a short L_{QNR} on the collection probability is counteracted by the electrical field in the space charge region at short circuit. In this case, the rear surface passivation enhances the *EQE* mostly in the long wavelength region.
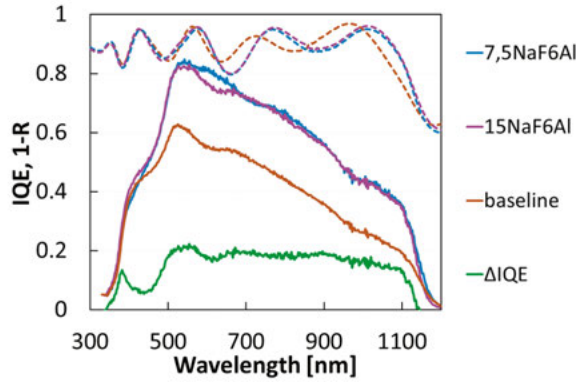

Figure 29. Ultra-thin solar cells in paper IV. Dashed lines: 1-reflectance *(1-R)* of the whole solar cell stack. Sold lines (except green): Internal quantum efficiency *(IQE),* Green solid line: *IQE* difference between the 15NaF6Al sample and the baseline reference.

On the other hand, if L_e is long and w_a is small compared to d_a, a high recombination rate at the rear surface decreases the *EQE* for both medium and long wavelengths. In this case, a rear surface passivation enhances the *EQE* in this wavelength region.

For the solar cells with a high band gap absorber (**paper II**) the *EQE* is larger for the passivated samples than for the unpassivated samples for wavelengths larger than 530 nm, even for the sample with the thickest absorber (1.45 μm) (see *Figure 28*). For the samples with ultra-thin (215 nm absorbers) studied in **paper IV**, the *EQE* for wavelengths larger than 330 nm is higher for solar cells with an Al_2O_3 passivation layer and NaF pre-deposition treatment, compared to the unpassivated reference (see *Figure 29*).

The increase in *EQE* for all wavelengths also indicates a narrow space charge region or incomplete collection in the space charge region for the ultra-thin solar cells. Additionally, optical and electrical modeling show that the higher *EQE* for passivated samples can only partially (< 10%) be explained by the higher reflection at the passivated contact in both cases. Thus,

differences in the *EQE* most probably stem from electrical effects. For the high band gap solar cells, they likely stem from a combination of passivation effects and doping effects. For the ultra-thin solar cells in **paper IV**, it is most likely the rear surface passivation layer that enhances the *EQE* for the samples passivated by an Al_2O_3 layer.

5.4.2   Current densities in the 2-diode model

In *Figure 30* the results of current density-voltage measurement at 100 K of the high band gap solar cells in **paper II** are shown. The measurements were performed in darkness and for three different illumination intensities. We observe for all samples in that study that for low temperatures the forward current density is limited at forward biases larger than V_{OC}, i.e. the *JV* curves have a roll-over. The magnitude of the roll-over current density is – as expected for a photocurrent density - larger for higher photon flux densities. It is also larger for the unpassivated samples as compared to the passivated samples in **paper II**. For the unpassivated samples it increases with reduced absorber layer thickness, but not so for the passivated samples. At even higher voltages and for low photon flux densities, the slopes of the current density curves increase again for most samples. J_{dark} is also severely limited for voltages over V_{OC} at low temperatures. When plotting the V_{OC} as a function of temperature for the different illumination intensities, the V_{OC} saturates at low temperatures for all illumination intensities, but at different values. The V_{OC} for small light fluxes is always lower than the V_{OC} for larger light fluxes at the same temperature – in agreement with 85 but disagreement with 86[63].

   To explain these results we proposed an energy barrier at the rear contact and applied the 2-diode model as described in chapter 2.4 and chapter 3.4. According to this model, the temperature independent J_{phb} dominates the roll-over current density for the unpassivated samples at low temperatures. As a photocurrent density, it depends on the amount of photons absorbed and the collection function, and thereby on the incident primary light flux on the solar cell, the absorption profile and the absorber layer thickness (see also chapter 2.3.2). With decreasing d_a more electrons are generated close to the rear contact and thus have a higher probability of reaching the rear contact and contributing to J_{phb}. For the passivated samples, the fixed charges in the passivation layer reduce the electrical field of the secondary junction, increase the carrier concentration asymmetry and decrease the conductivity for electron transport towards the contact. Therefore, J_{phb} and thus the roll-over current density decrease and become independent of the absorber layer thickness, and J_{phm} increases. In contrast to the unpassivated case, J_{0b} is also a significant part of the roll-over current density at low temperatures. Thus, by comparing passivated and unpassivated samples and different d_a, J_{phb} can be discerned. As J_{phb} is temperature independent, we can conclude that for unpassivated

samples J_{SC} and V_{OC} are reduced due to the rear surface also for these CIGS solar cells, with a high band gap and a flat Ga profile.
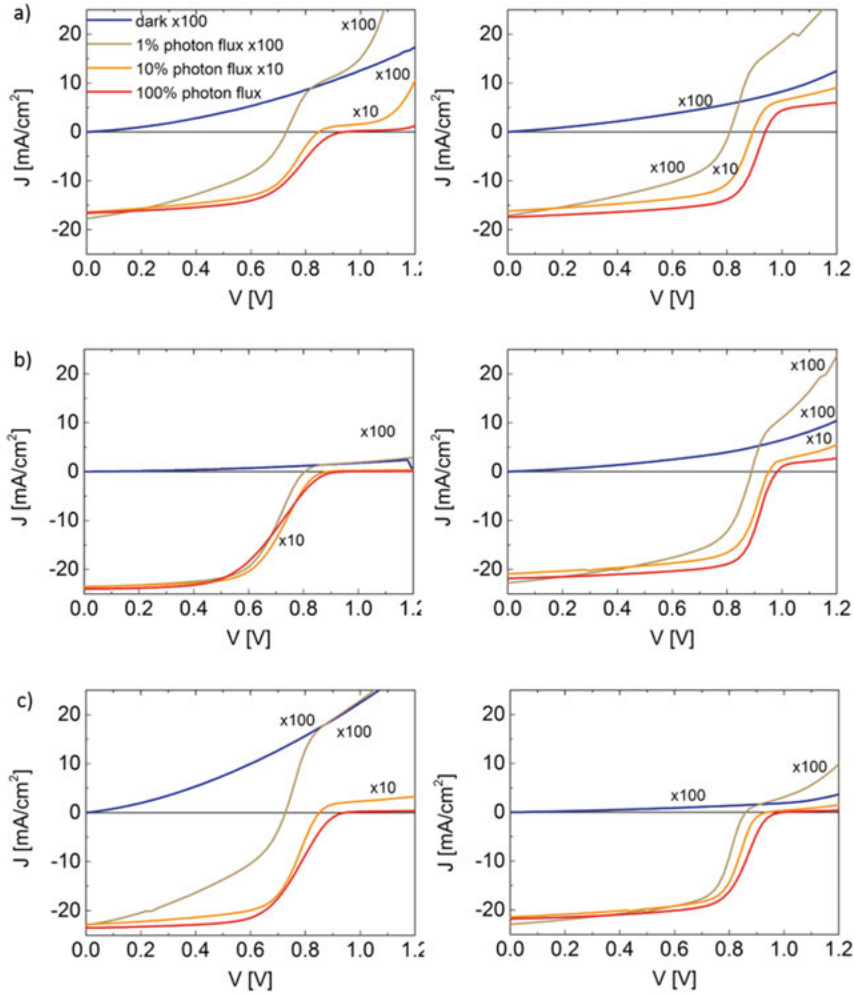
Figure 30. High band gap solar cells in **Paper II**. Current density-voltage (*JV*) curves measured at a temperature *T*=100 K for 0, 1, 10 and 100% photon flux density for samples with a a) 0.60 μm, b) 0.85 μm and c) 1.45 μm absorber layer. The left chart shows the curves for the passivated sample, the right chart shows the curves for the unpassivated reference sample. To be able to depict the current densities for the different photon flux densities on one axis, the measured current densities have been multiplied with a factor of 10 for the measurements at 10 % photon flux density and with a factor 100 for the measurements at 1 % photon flux density.

For the *JVT* measurement results at 100% light flux, no general trend for $\Delta\varphi$ and thus for J_{0b} was observed. This lack of a trend means that the band diagram of the contact for J^h is not observably influenced by the electrical

field stemming from the oxide charge in the passivation layer although $V_b < 0$ (see chapter 2.2). This can be explained in two ways: the passivation layer does not induce an additional electrical field and the passivation layer only passivates chemically, or the electrical field does not spread far enough laterally into the point contacts. We assume here that the electrical field spreads both longitudinally into the absorber layer, but also laterally into the CIGS at the point contacts and thus to the CIGS-MoSe$_2$ interface. As the rear contact barrier height remains unchanged in the experiment, there probably is a path for the holes in the middle of the point contacts through the CIGS-MoSe$_2$ interface that lies outside of the region affected by the field of the fixed oxide charges. As the smallest dimension of the contact opening is 0.4 µm, the d_w has to be smaller than half of that value, namely 0.2 µm. Only charge carriers within that distance or less from the oxide layer are affected by the additional electrical field.

5.4.3   Barrier height for holes in the 2-diode model

As described in **paper III**, we found that a 0.9 nm thick Al$_2$O$_3$ passivation layer lowers the hole barrier at the rear contact by 0.2 eV for the post-deposition treated samples compared to the unpassivated reference. If we assume that the Al$_2$O$_3$ layer is completely covering for post-deposition treated samples, the holes need to tunnel through the Al$_2$O$_3$ layer and pass the rear interface region of the CIGS absorber, where the electrical field effect stemming from the negative charges in the passivation layer reduces the band bending and thus the associated hole barrier height. As long as the passivation layer is so thin that the holes can tunnel through it, the energy off-set at the passivation layer is not visible in the *JVT* measurements, but the reduced band bending due to the negative oxide charge in the Al$_2$O$_3$ is. On the other hand, if sufficiently large openings existed in the passivation layer, J^h will not be affected by the electrical field as we showed in **paper II** for the samples with point contacts. We could thus conclude that the Al$_2$O$_3$ layer in post-DT samples not only completely covers the rear contact, but that the current probably tunnels through the layer and that the Al$_2$O$_3$ layer lowers the barrier for hole transport associated to the band bending in the CIGS at the rear contact.

5.4.4   Components of the apparent shunt conductance

For CIGS solar cells with thin and ultra-thin absorbers [76,94,117–119] the light *JV* curves of the unpassivated reference samples have larger values of the apparent shunt conductance ($dJ_{light}/dV|_{V=0}$) than the light *JV* curves of the passivated samples. The large apparent shunt conductances for the

unpassivated case have been explained by voltage dependent current collection[157,158]. However, when quantifying the voltage dependent current collection by biased AQE measurements, a residual shunt $\frac{dJres}{dV}\Big|_{V\approx0}$ in the light JV curve still remains unexplained for solar cells without passivation layer in **paper I,** (see chapter 3.3). $\frac{dJres}{dV}\Big|_{V\approx0}$ can be attributed to a voltage and light-dependent photocurrent collection $\eta(j_\gamma,V)$, light depend shunt paths $G_{sh}(j_\gamma)$ or light dependent diode current densities $J_{diode}(V,j_\gamma)$.

Here I present the comparison of a sample with Al_2O_3 rear surface passivation (15NaF6Al) and an unpassivated reference sample from **paper IV**. As seen in *Figure 27*, the light JV curve of the unpassivated reference has a larger slope around $V = 0$ V than the light JV curve of the sample with Al_2O_3 rear surface passivation (15NaF6Al). The slope of the dark curve is $\frac{dJ_{dark}}{dV}\Big|_{V\approx0} \approx 0.08$ mS/cm^2 on the unpassivated reference sample. It increases by a factor 46 to $\frac{dJ_{light}}{dV}\Big|_{V\approx0} \approx 3.7$ mS/cm^2 under illumination. In contrast, the slope only doubles from $\frac{dJ_{dark}}{dV}\Big|_{V\approx0} \approx 0.58$ to $\frac{dJ_{light}}{dV}\Big|_{V\approx0} \approx 1.15$ mS/cm^2 on the passivated 15NaF6Al sample. As derived from AQE/EQE measurements $\frac{dJ_{ph}}{dV}\Big|_{V\approx0} \approx 1.7$ mS/cm^2 for the reference and 1.0 mS/cm^2 for the passivated sample. Thus, whereas the dark shunt together with the voltage-dependent current collection can completely explain the observed shunt-like behavior for the passivated sample, a residual slope of $\frac{dJres}{dV}\Big|_{V\approx0} \approx 2$ mS/cm^2 is left unexplained for the reference. Summarizing, the passivation layer reduces not only voltage-dependent current collection, but also extinguishes the residual shunt-like behavior in the ultra-thin devices in **paper IV**.

6 Concluding remarks

First, I would like to summarize the results and discussion presented in chapter 3, 4 and 5.

- For CIGS solar cells with 0.45, 0.85 and 1.45 μm thick absorber layers with a *GGI* = 0.60 and without Ga grading, a passivation effect could be discerned for 30 nm thick Al_2O_3 rear surface passivation layers by comparing and modeling the *IQE* and *JVT* data for the passivated solar cells and the unpassivated reference solar cells.
- The rear contact of CIGS solar cells could be electrically described by a hole current over a hole barrier (including a breakthrough current at high voltages), an electron photocurrent and a hole shunt current.
- A high hole barrier reduces the asymmetry between the majority and minority carriers at the rear contact, which increases the detrimental electron photocurrent into the rear contact or the rear surface recombination rate (depending on the electrical model of the contact used).
- The results indicate that the barrier can be decreased if the charge carriers tunnel through a passivating MIS contact structure with ALD-Al_2O_3 in the role of the insulator. The Al_2O_3 layer probably lowers the barrier for hole transport associated with the band bending in the CIGS at the rear contact.
- The Al_2O_3 layer probably covers the rear contact completely already for 10 ALD cycles, thus establishing a MIS contact. The charge carriers probably tunnel through the Al_2O_3 layer.
- A (tunneling) MIS rear contact does not increase the efficiency compared to samples with a standard rear contact if a NaF precursor is not used. An optimal thickness for the Al_2O_3 layer in these MIS contacts was not found.
- Nano-structuring is necessary for sufficient conduction through ALD-Al_2O_3 layers thicker than 1 nm, if NaF is not applied at all or in a post-deposition treatment after CIGS deposition. Otherwise, J_{ph} is blocked.
- A partial rear contact (i.e. a rear contact with a nanostructured Al_2O_3 passivation layer inserted between the absorber and the contact) can decrease the electron photocurrent over the hole barrier.
- The hole barrier at the MoSe$_2$-CIGS interface in the point contacts of a partial rear contact may be decreased by using a thicker NaF precursor layer.
- According to a one-diode model, rear surface passivation with Al_2O_3 decreases the apparent shunt conductance dJ_{light}/dV under illumination. It

does not only reduce the part of the apparent shunt conductance stemming from voltage-dependent current collection, but also strongly reduces a residual shunt-like behavior. Thus, the residual shunt-like behavior is probably associated with recombination at the rear surface.

- Inserting an Al_2O_3 passivation layer can reduce the number of shunted cells per sample.
- NaF precursor layers deposited on ALD-Al_2O_3 passivation layers prior to CIGS evaporation can ensure unimpeded current transport, so that an additional fabrication step for contacting can be avoided.
- Sufficient conduction has been shown for up to 6 nm thick ALD-Al_2O_3 passivation layers in this work. The thickness of the NaF precursor layer is a factor in determining the maximum thickness of the Al_2O_3 layer that still allows for sufficient conduction.
- PL measurement results indicate that Al_2O_3 rear surface passivated CIGS solar cells can potentially achieve high values of V_{OC}. They also suggest that the potential gain in V_{OC} may be reduced if the thickness of a NaF precursor layer is increased. Unfortunately, thick precursor layers are necessary to obtain sufficient conduction through unpatterned ALD-Al_2O_3 layers.
- This lower-quality passivation is nevertheless beneficial for the ultra-thin CIGS solar cells with a d_a of 215 nm. Compared to reference samples, the passivated samples had a higher V_{OC} (+120 mV), an increased J_{SC} (+6 mA/cm^2) and EQE and thus a higher efficiency (+3% to 8.6%). Most of the gain stems from the passivation and not from optical effects.
- Any studies on the electrical properties of Al_2O_3 passivation layers should consider the Na(F) concentration at the rear contact and the Na(F) supply method.
- In previous studies, if a few nanometers thin Al_2O_3 passivation layers were used in combination with NaF precursor layers, the current did most likely not only flow through the intentional nanocontacts. Details on the contact area, pitch and contact size might thus be misleading.
- For the high band gap solar cells with a partial rear contact, the applied nanostructuring was sufficient for conduction. The Al_2O_3 rear surface passivation layers were 30 nm thick and not subjected to a NaF precursor, so that conduction through the layers themselves can be excluded.
- Passivation with Al_2O_3 layers with a NaF precursor layer on top might be the best choice, if expensive and time-consuming patterning steps are to be avoided. In this case, Na(F) precursor deposition needs to be used (which does not exclude other additional Na application methods) and a compromise between conduction through the Al_2O_3 layer, passivation effectiveness of the Al_2O_3 layer and beneficial and detrimental effects of Na on the absorber needs to be found.
- Photoluminescence data indicate that ALD-HfO_2 layers passivate the rear contact well, though slightly worse than ALD-Al_2O_3 layers. In their case,

the PL signal does not depend on the NaF concentration in the used samples. Thus, CIGS solar cells with a patterned HfO_2 rear surface passivation layer can be expected to have high V_{OC} values regardless of NaF application method.

- Solar cells with unpatterned HfO_2 layers block the current regardless of NaF supply.
- HfO_2 might be the passivation material of choice, if conduction through the HfO_2 layer is obtained by an extra fabrication step such as nanopatterning. Good surface passivation properties are then ensured independently of the Na incorporation method and concentration and no compromise concerning these is needed. Conduction through the passivation layer and passivation effectiveness can be optimized by the nanopatterning method and independently of the optimization of the Na application method to achieve good electrical absorber properties.

In 2012/2013 the idea of partial rear contacts from the Si solar cell world was imported to the CIGS world. Unfortunately, partial rear contacts usually require time consuming and expensive patterning steps and the contacts themselves (in the narrow sense, i.e. the point contacts) are left unpassivated. Today, Si solar cell researchers are turning away from partial rear contacts and rear contact research focuses increasingly on Si heterojunction solar cells, described by the selective membrane model. In these solar cells, current transport to the contacts is selective. The complete rear surface both serves as a contact and is passivated, namely both chemically and due a strong carrier density asymmetry. Passivation and conduction are in series instead of parallel as in cells with partial rear contacts. Not patterning the passivation layer as I have done in two papers in this thesis – no matter if the rear contact is in fact partial or not- is a first step into this direction. I hope that the CIGS solar cell community in future considers both CIGS solar cells with a heterojunction at the rear contact and the selective membrane model.

Bibliography

[1]   N. Lefèvre, Measuring the energy security implications of fossil fuel resource concentration, Energy Policy. 38 (2010) 1635–1644.

[2]   L. Al-Ghussain, Global warming: review on driving forces and mitigation, Environ. Prog. Sustain. Energy. 38 (2019) 13–21. doi:10.1002/ep.13041.

[3]   M.A.A. Pedrasa, T.D. Spooner, I.F. MacGill, A novel energy service model and optimal scheduling algorithm for residential distributed energy resources, Electr. Power Syst. Res. 81 (2011) 2155–2163.

[4]   S. Davidsson, M. Höök, Material requirements and availability for multi-terawatt deployment of photovoltaics, Energy Policy. 108 (2017) 574–582. doi:10.1016/j.enpol.2017.06.028.

[5]   M. Raugei, S. Bargigli, S. Ulgiati, Life cycle assessment and energy pay-back time of advanced photovoltaic modules: CdTe and CIS compared to poly-Si, Energy. 32 (2007) 1310–1318.

[6]   K. Branker, M.J.M. Pathak, J.M. Pearce, A review of solar photovoltaic levelized cost of electricity, Renew. Sustain. Energy Rev. 15 (2011) 4470–4482.

[7]   X. Wang, L. Kurdgelashvili, J. Byrne, A. Barnett, The value of module efficiency in lowering the levelized cost of energy of photovoltaic systems, Renew. Sustain. Energy Rev. 15 (2011) 4248–4254.

[8]   O.D. Miller, E. Yablonovitch, S.R. Kurtz, Strong Internal and External Luminescence as Solar Cells Approach the Shockley – Queisser Limit, IEEE J. Photovoltaics. 2 (2012) 303–311.

[9]   A. Cuevas, T. Allen, J. Bullock, Yimao Wan, Di Yan, Xinyu Zhang, Skin care for healthy silicon solar cells, in: 42nd IEEE Photovolt. Spec. Conf., New Orleans, LA, USA, 2015: pp. 1–6. doi:10.1109/PVSC.2015.7356379.

[10]   O. Lundberg, M. Edoff, L. Stolt, The effect of Ga-grading in CIGS thin film solar cells, Thin Solid Films. 480–481 (2005) 520–525. doi:10.1016/j.tsf.2004.11.080.

[11]   B. Vermang, J.T. Watjen, C. Frisk, V. Fjallstrom, F. Rostvall, M. Edoff, P. Salome, J. Borme, N. Nicoara, S. Sadewasser, Introduction of Si PERC rear contacting design to boost efficiency of Cu(In,Ga)Se$_2$ solar cells, IEEE J. Photovoltaics. 4 (2014) 1644–1649. doi:10.1109/JPHOTOV.2014.2350696.

[12]   B. Vermang, V. Fjallström, X. Gao, M. Edoff, Improved rear surface passivation of Cu(In,Ga)Se$_2$ solar cells: A combination of an Al$_2$O$_3$ rear surface passivation layer and nanosized local rear point contacts, IEEE J. Photovoltaics. 4 (2014) 486–492. doi:10.1109/JPHOTOV.2013.2287769.

[13]   T.S. Cells, S. Paul, S. Grover, I.L. Repins, B.M. Keyes, M.A. Contreras, K. Ramanathan, Analysis of Back-Contact Interface Recombination in Thin-Film Solar Cells, IEEE J. Photovoltaics. 8 (2018) 871–878. doi:10.1109/JPHOTOV.2018.2819664.

[14]   M.A. Green, Y. Hishikawa, E.D. Dunlop, D.H. Levi, J. Hohl-Ebinger, A.W.Y. Ho-Baillie, Solar cell efficiency tables (version 52), Prog. Photovoltaics Res. Appl. 26 (2018) 427–436. doi:10.1002/pip.3040.

[15]   M.A. Green, K. Emery, Y. Hishikawa, W. Warta, E.D. Dunlop, Solar cell efficiency tables (version 40), Prog. Photovoltaics Res. Appl. 20 (2012) 606–614. doi:10.1002/pip.2267.

[16]   J. Lindahl, U. Zimmermann, P. Szaniawski, T. Törndahl, A. Hultqvist, P. Salome, C. Platzer-Björkman, and M.E. Orkman, Inline Cu(In,Ga)Se$_2$ Co-evaporation for High-Efficiency Solar Cells and Modules, IEEE J. Photovoltaics. 3 (2013) 1100–1105. doi:10.1109/JPHOTOV.2013.2256232.

[17]   W.N. Shafarman, L. Stolt, Cu(InGa)Se$_2$ Solar Cells, in: A. Luque, S.S. Hegedus (Eds.), Handb. Photovolt. Sci. Eng., John Wiley & Sons, Ltd, 2003: pp. 567–616.

[18]   R. Scheer, H.-W. Schock, Chalcogenide Photovoltaics: Physics, Technologies, and Thin film Devices, Wiley-Vch Verlag GmbH & Co. KGaA, 2011.

[19]   A. Cuevas, S. Member, Geometrical Analysis of Solar Cells With Partial Rear Contacts, IEEE J. Photovoltaics. 2 (2012) 485–493. doi:10.1109/JPHOTOV.2012.2204958.

[20]   A. Cuevas, D. Yan, F. Haase, J.H. Petermann, R. Brendel, A Comparison of Models to Optimize Partial Rear Contact Solar Cells, Energy Procedia. 38 (2013) 13–21. doi:10.1016/j.egypro.2013.07.244.

[21]   B. Thaidigsmann, E. Lohmüller, F. Fertig, F. Clement, A. Wolf, Characterization and modeling of screen-printed metal insulator semiconductor tunnel junctions for integrated bypass functionality in crystalline silicon solar cells, J. Appl. Phys. 113 (2013) 214502. doi:10.1063/1.4807931.

[22]   D. Abou-Ras, T. Kirchartz, U. Rau, eds., Advanced Characterization Techniques for Thin Film Solar Cells, 1st ed., Wiley-VCH Verlag GmbH & Co. KGaA, Weinheim, Germany, 2011. doi:10.1002/9783527636280.

[23]   P. Würfel, U. Würfel, Physics of Solar Cells, Wiley-VCH Verlag GmbH, Weinheim, Germany, 2005. doi:10.1002/9783527618545.

[24]   A. Cuevas, D. Yan, Misconceptions and misnomers in solar cells, IEEE J. Photovoltaics. 3 (2013) 916–923. doi:10.1109/JPHOTOV.2013.2238289.

[25]   K. Decock, S. Khelifi, M. Burgelman, Analytical versus numerical analysis of back grading in CIGS solar cells, Sol. Energy Mater. Sol. Cells. 95 (2011) 1550–1554. doi:10.1016/j.solmat.2010.10.020.

[26]   S. Smit, Passivating selective contacts for silicon photovoltaics : Solar cells designed by physics, Technische Universiteit Eindhoven, 2015.

[27]   F.A. Lindholm, J.G. Fossum, E.L. Burgess, Application of the Superposition Principle to Solar-Cell Analysis, IEEE Trans. Electron Devices. 26 (1979) 165–171. doi:10.1109/T-ED.1979.19400.

[28]   W.W. Gärtner, Depletion-layer photoeffects in semiconductors, Phys. Rev.
        116 (1959) 84.

[29]   S.J. Robinson, A.G. Aberle, M.A. Green, Departures from the principle of
        superposition in silicon solar cells, J. Appl. Phys. 76 (1994) 7920.
        doi:10.1063/1.357902.

[30]   U. Würfel, A. Cuevas, P. Würfel, Charge carrier separation in solar cells,
        IEEE J. Photovoltaics. 5 (2015) 461–469.
        doi:10.1109/JPHOTOV.2014.2363550.

[31]   N.G. Tarr, D.L. Pulfrey, An investigation of dark current and photocurrent
        superposition in photovoltaic devices, Solid State Electron. 22 (1979) 265–
        270. doi:10.1016/0038-1101(79)90032-7.

[32]   W. Shockley, The Theory of p-n Junctions in Semiconductors and p-n
        Junction Transistors, Bell Syst. Tech. J. 28 (1949) 435–489.
        doi:10.1002/j.1538-7305.1949.tb03645.x.

[33]   M.A. Green, Do built-in fields improve solar cell performance?, Prog.
        Photovoltaics Res. Appl. 17 (2009) 57–66. doi:10.1002/pip.851.

[34]   P. Würfel, Is an illuminated semiconductor far from thermodynamic
        equilibrium?, Sol. Energy Mater. Sol. Cells. 38 (1995) 23–28.
        doi:10.1016/0927-0248(94)00211-8.

[35]   A. Cuevas, Y. Wan, D. Yan, C. Samundsett, T. Allen, X. Zhang, J. Cui, J.
        Bullock, Carrier population control and surface passivation in solar cells,
        Sol. Energy Mater. Sol. Cells. 184 (2018) 38–47.
        doi:10.1016/j.solmat.2018.04.026.

[36]   F. Herrmann, P. Würfel, The semiconductor diode as a rectifier, a light
        source, and a solar cell: A simple explanation, Am. J. Phys. 74 (2006) 591–
        594. doi:10.1119/1.2192786.

[37]   R.F. Pierret, Semiconductor Device fundamentals, 2nd ed., Addison Wesley,
        1996.

[38]   A. Rockett, The Materials Science of Semiconductors, Springer US, Boston,
        MA, 2008. doi:10.1007/978-0-387-68650-9.

[39]   U. Mishra, J. Singh, Semiconductor Device Physics and Design, 1st ed.,
        Springer Netherlands, Dordrecht, 2007. doi:10.1007/978-1-4020-6481-4.

[40]   R. Brendel, R. Peibst, Contact Selectivity and Efficiency in Crystalline
        Silicon Photovoltaics, IEEE J. Photovoltaics. 6 (2016) 1413–1420.
        doi:10.1109/JPHOTOV.2016.2598267.

[41]   E.T. Roe, K.E. Egelhofer, M.C. Lonergan, Limits of Contact
        Selectivity/Recombination on the Open-Circuit Voltage of a Photovoltaic,
        ACS Appl. Energy Mater. 1 (2018) 1037−1046.
        doi:10.1021/acsaem.7b00179.

[42]   J. Melskens, B.W.H. Van De Loo, B. Macco, L.E. Black, S. Smit, W.M.M.
        Kessels, Passivating Contacts for Crystalline Silicon Solar Cells: From
        Concepts and Materials to Prospects, IEEE J. Photovoltaics. 8 (2018) 373–
        388. doi:10.1109/JPHOTOV.2018.2797106.

[43]   B. Macco, B.W.H. Van De Loo, J. Melskens, S. Smit, W.M.M.E. Kessels,
        Status and prospects for atomic layer Deposited metal oxide thin films in
        passivating contacts for c-Si photovoltaics, in: 43th Photovolt. Spec. Conf.,
        IEEE, 2016: pp. 2473–2478. doi:10.1109/PVSC.2017.8366571.

[44] J. Bullock, D. Yan, A. Cuevas, Passivation of aluminium-n+ silicon contacts for solar cells by ultrathin Al_2O_3 and SiO_2 dielectric layers, Phys. Status Solidi - Rapid Res. Lett. 7 (2013) 946–949. doi:10.1002/pssr.201308115.

[45] J. Bullock, Advanced Contacts for crystalline silicon solar cells, Australian National University, 2016.

[46] R.S. Bonilla, B. Hoex, P. Hamer, P.R. Wilshaw, Dielectric surface passivation for silicon solar cells: A review, Phys. Status Solidi Appl. Mater. Sci. 214 (2017) 1700293. doi:10.1002/pssa.201700293.

[47] A. Fell, F. Feldmann, C. Messmer, M. Bivour, M.C. Schubert, S.W. Glunz, Adaption of basic Metal-Insulator-Semiconductor (MIS) theory for passivating contacts within numerical solar cell modeling, IEEE J. Photovoltaics. 8 (2018) 1546–1552. doi:10.1109/JPHOTOV.2018.2871953.

[48] A. Fell, J. Schön, M.C. Schubert, S.W. Glunz, The concept of skins for silicon solar cell modeling, Sol. Energy Mater. Sol. Cells. 173 (2017) 128–133. doi:10.1016/j.solmat.2017.05.012.

[49] S.W. Glunz, M. Bivour, C. Messmer, F. Feldmann, R. Müller, C. Reichel, A. Richter, F. Schindler, J. Benick, M. Hermle, Passivating and Carrier-selective Contacts – Basic Requirements and Implementation, 44th IEEE Photovolt. Spec. Conf. (2017) 2046–2069.

[50] T. Kirchartz, J. Bisquert, I. Mora-Sero, G. Garcia-Belmonte, Classification of solar cells according to mechanisms of charge separation and charge collection, Phys. Chem. Chem. Phys. 17 (2015) 4007–4014. doi:10.1039/c4cp05174b.

[51] U. Rau, S. Wang, Do solar cells need a built-in potential?, in: Quantsol Work. Proc., European Society for Quantum Solar Energy Conversion, 2018. http://www.quantsol.org/pub/pub18_02.pdf.

[52] U. Rau, G. Kron, J.H. Werner, Reply to Comments on "Electronic Transport in Dye-Sensitized Nanoporous TiO2 Solar Cells - Comparison of Electrolyte and Solid-State Devices". On the Photovoltaic Action in pn-Junction and Dye-Sensitized Solar Cells, J. Phys. Chem. B. 107 (2003) 13547–13550. doi:10.1021/jp036050i.

[53] G.H. Bauer, Photovoltaic Solar Energy Conversion, 1st ed., Springer Berlin Heidelberg, Berlin, Heidelberg, 2015. doi:10.1007/978-3-662-46684-1.

[54] J. Malmström, On Generation and Recombination in $Cu(In,Ga)Se_2$ thin-film solar cells, Uppsala Universitet, 2005.

[55] O. Lundberg, M. Bodegård, J. Malmström, L. Stolt, Influence of the $Cu(In,Ga)Se_2$ thickness and Ga grading on solar cell performance, Prog. Photovoltaics Res. Appl. 11 (2003) 77–88. doi:10.1002/pip.462.

[56] K.R. McIntosh, L.E. Black, On effective surface recombination parameters, J. Appl. Phys. 116 (2014) 014503. doi:10.1063/1.4886595.

[57] E.H. Rhoderick, Metal-semiconductor contacts, Oxford Univeristy Press, Oxford, 1978.

[58] S. Puttnins, M.S. Hammer, J. Neerken, I. Riedel, F. Daume, A. Rahm, A. Braun, M. Grundmann, T. Unold, Impact of sodium on the device characteristics of low temperature-deposited $Cu(In,Ga)Se_2$ solar cells, Thin Solid Films. 582 (2015) 85–90. doi:10.1016/j.tsf.2014.07.048.

[59]   F. Pianezzi, P. Reinhard, A. Chirilă, B. Bissig, S. Nishiwaki, S. Buecheler, A.N. Tiwari, Unveiling the effects of post-deposition treatment with different alkaline elements on the electronic properties of CIGS thin film solar cells., Phys. Chem. Chem. Phys. 16 (2014) 8843–51. doi:10.1039/c4cp00614c.

[60]   M. Richter, C. Schubbert, P. Eraerds, J. Parisi, I. Riedel, T. Dalibor, J. Palm, Comprehensive simulation model for Cu(In,Ga)(Se,S)$_2$ solar cells, Sol. Energy Mater. Sol. Cells. 132 (2015) 162–171. doi:10.1016/j.solmat.2014.08.047.

[61]   S.H. Demtsu, J.R. Sites, Effect of back-contact barrier on thin-film CdTe solar cells, Thin Solid Films. 510 (2006) 320–324. doi:10.1016/j.tsf.2006.01.004.

[62]   N. Neugebohrn, M.S. Hammer, J. Neerken, J. Parisi, I. Riedel, Analysis of the back contact properties of Cu(In,Ga)Se$_2$ solar cells employing the thermionic emission model, Thin Solid Films. 582 (2015) 332–335. doi:10.1016/j.tsf.2014.10.073.

[63]   T. Ott, F. Schönberger, T. Walter, D. Hariskos, O. Kiowski, O. Salomon, R. Schäffler, Verification of phototransistor model for Cu(In,Ga)Se$_2$ solar, Thin Solid Films. 582 (2015) 392–396. doi:10.1016/j.tsf.2014.09.025.

[64]   T. Ott, T. Walter, D. Hariskos, Accelerated Aging and Contact Degradation of CIGS Solar Cells, IEEE J. Photovoltaics. 3 (2013) 514–519. doi:10.1109/PVSC-Vol 2.2013.6656770.

[65]   A. Rockett, J.K.J. van Duren, A. Pudov, W.N. Shafarman, First quadrant phototransistor behavior in CuInSe$_2$ photovoltaics, Sol. Energy Mater. Sol. Cells. 118 (2013) 141–148. doi:10.1016/j.solmat.2013.07.032.

[66]   G.T. Koishiyev, J.R. Sites, Determination of back contact barrier height in Cu(In,Ga)(Se,S)2 and CdTe solar cells, in: 33rd IEEE Photovolt. Spec. Conf., San Diego, CA, USA, 2008: pp. 1–3. doi:10.1109/PVSC.2008.4922886.

[67]   K.-J. Hsiao, J.-D. Liu, H.-H. Hsieh, T.-S. Jiang, Electrical impact of MoSe$_2$ on CIGS thin-film solar cells., Phys. Chem. Chem. Phys. 15 (2013) 18174–8. doi:10.1039/c3cp53310g.

[68]   T. Ott, T. Walter, T. Unold, Phototransistor effects in Cu(In,Ga)Se$_2$ solar cells, Thin Solid Films. 535 (2013) 275–278. doi:10.1016/j.tsf.2012.11.084.

[69]   A. Niemegeers, M. Burgelman, Effects of the Au/CdTe back contact on IV and CV characteristics of Au/CdTe/CdS/TCO solar cells, J. Appl. Phys. 81 (1997) 2881. doi:10.1063/1.363946.

[70]   T. Eisenbarth, R. Caballero, M. Nichterwitz, C.A. Kaufmann, H.-W. Schock, T. Unold, Characterization of metastabilities in Cu(In,Ga)Se$_2$ thin-film solar cells by capacitance and current-voltage spectroscopy, J. Appl. Phys. 110 (2011) 094506. doi:10.1063/1.3656453.

[71]   T. Eisenbarth, T. Unold, R. Caballero, C.A. Kaufmann, H.-W. Schock, Interpretation of admittance, capacitance-voltage, and current-voltage signatures in Cu(In,Ga)Se2 thin film solar cells, J. Appl. Phys. 107 (2010) 034509. doi:10.1063/1.3277043.

[72] M. Roy, S. Damaskinos, J.E. Phillips, The diode current mechanism in CuInSe$_2$/(CdZn)S heterojunctions, in: 20th IEEE Photovolt. Spec. Conf., Las Vegas, NV, 1988: pp. 1618–1623. doi:10.1109/PVSC.1988.105986.

[73] A. Urbaniak, M. Igalson, F. Pianezzi, S. Bücheler, A. Chirilă, P. Reinhard, A.N. Tiwari, Effects of Na incorporation on electrical properties of Cu(In,Ga)Se$_2$-based photovoltaic devices on polyimide substrates, Sol. Energy Mater. Sol. Cells. 128 (2014) 52–56. doi:10.1016/j.solmat.2014.05.009.

[74] T. Negami, S. Nishiwaki, Y. Hashimoto, N. Kohara, Effect of the absorber thickness on performance of Cu(In,Ga)Se2 solar cells, in: Proc. 2nd WCPEC, Vienna, 1998: pp. 1181–1184.

[75] W.N. Shafarman, R.W. Birkmire, S. Marsillac, M. Marudachalam, N. Orbey, T. Russel, Effect of reduced deposition temperature, time, and thickness on Cu(In,Ga)Se$_2$ films and devices, in: 26th IEEE Photovolt. Spec. Conf., Anaheim, CA, USA, 1997: pp. 331–334. doi:10.1109/pvsc.1997.654095.

[76] D. Ledinek, B. Vermang, M. Edoff, Thickness and Ga-content variations in co-evporated CIGS solar cells with flat Ga profile - an electrical characterization, in: 29th Eur. Photovolt. Sol. Energy Conf. Exhib., 2014: pp. 1832–1836.

[77] Z. Jehl, F. Erfurth, N. Naghavi, L. Lombez, I. Gerard, M. Bouttemy, P. Tran-Van, A. Etcheberry, G. Voorwinden, B. Dimmler, W. Wischmann, M. Powalla, J.F. Guillemoles, D. Lincot, Thinning of CIGS solar cells: Part II: Cell characterizations, Thin Solid Films. 519 (2011) 7212–7215. doi:10.1016/j.tsf.2010.12.224.

[78] G. Yin, A. Steigert, P. Andrae, M. Goebelt, M. Latzel, P. Manley, I. Lauermann, S. Christiansen, M. Schmid, Integration of plasmonic Ag nanoparticles as a back reflector in ultra-thin Cu(In,Ga)Se$_2$ solar cells, Appl. Surf. Sci. 355 (2015) 800–804. doi:10.1016/j.apsusc.2015.07.195.

[79] C. Van Lare, G. Yin, A. Polman, M. Schmid, Light Coupling and Trapping in Ultrathin Cu(In,Ga)Se$_2$ Solar Cells Using Dielectric Scattering Patterns, ACS Nano. 9 (2015) 9603–9613. doi:10.1021/acsnano.5b04091.

[80] M. Schmid, Review on light management by nanostructures in chalcopyrite solar cells, Semicond. Sci. Technol. 32 (2017) 043003. doi:10.1088/1361-6641/aa59ee.

[81] P. Casper, R. Hünig, G. Gomard, O. Kiowski, C. Reitz, U. Lemmer, M. Powalla, M. Hetterich, Optoelectrical improvement of ultra-thin Cu(In,Ga)Se$_2$ solar cells through microstructured MgF$_2$ and Al$_2$O$_3$ back contact passivation layer, Phys. Status Solidi - Rapid Res. Lett. 10 (2016) 376–380. doi:10.1002/pssr.201600018.

[82] B. Vermang, J.T. Wätjen, V. Fjällström, F. Rostvall, M. Edoff, R. Gunnarsson, I. Pilch, U. Helmersson, R. Kotipalli, F. Henry, D. Flandre, Highly reflective rear surface passivation design for ultra-thin Cu(In,Ga)Se$_2$ solar cells, Thin Solid Films. 582 (2014) 300–303. doi:10.1016/j.tsf.2014.10.050.

[83] J. Malmström, O. Lundberg, L. Stolt, Potential for light trapping in Cu(In,Ga)Se$_2$ solar cells, in: 3rd World Conf. Photovolt. Energy Convers. May 11-18, 2003 Osaka, Japan, 2003: pp. 344–347.

[84] J. Keller, F. Gustavsson, L. Stolt, M. Edoff, T. Törndahl, On the beneficial effect of Al2O3 front contact passivation in Cu(In,Ga)Se2 solar cells, Sol. Energy Mater. Sol. Cells. 159 (2017) 189–196. doi:10.1016/j.solmat.2016.09.019.

[85] S. Garud, N. Gampa, T.G. Allen, R. Kotipalli, D. Flandre, M. Batuk, J. Hadermann, M. Meuris, J. Poortmans, A. Smets, B. Vermang, Surface Passivation of CIGS Solar Cells Using Gallium Oxide, Phys. Status Solidi. 215 (2018) 1700826. doi:10.1002/pssa.201700826.

[86] R. Kotipalli, B. Vermang, V. Fjällström, M. Edoff, R. Delamare, D. Flandre, Influence of Ga/(Ga+In) grading on deep-defect states of Cu(In,Ga)Se$_2$ solar cells, Phys. Status Solidi - Rapid Res. Lett. 9 (2015) 157–160. doi:10.1002/pssr.201510024.

[87] J.G. Fossum, Physical Operation of Back-Surface-Field Silicon Solar Cells, IEEE Trans. Electron Devices. ED-24 (1977) 322–325. doi:10.1109/T-ED.1977.18735.

[88] A. Goetzberger, J. Knobloch, B. Voß, Crystalline Silicon Solar Cells, John Wiley & Sons, Ltd, Chichester, UK, 2014. doi:10.1002/9781119033769.

[89] D. Ledinek, P. Salome, C. Hägglund, U. Zimmermann, M. Edoff, Rear Contact Passivation for High Band Gap Cu(In,Ga)Se$_2$ Solar Cells with a flat Ga profile, IEEE J. Photovoltaics. 8 (2018) 864–870. doi:10.1109/JPHOTOV.2018.2813259.

[90] R. Kotipalli, O. Poncelet, G. Li, Y. Zeng, L.A. Francis, B. Vermang, D. Flandre, Addressing the impact of rear surface passivation mechanisms on ultra-thin Cu(In,Ga)Se$_2$ solar cell performances using SCAPS 1-D model, Sol. Energy. 157 (2017) 603–613. doi:10.1016/j.solener.2017.08.055.

[91] R. Kotipalli, B. Vermang, J. Joel, R. Rajkumar, M. Edoff, D. Flandre, Investigating the electronic properties of Al2O3/Cu(In,Ga)Se$_2$ interface, AIP Adv. 5 (2015) 107101. doi:10.1063/1.4932512.

[92] C. Frisk, Modeling and electrical characterization of Cu(In,Ga)Se2 and Cu2ZnSnS4 solar cells, Uppsala University, 2017. http://urn.kb.se/resolve?urn=urn:nbn:se:uu:diva-320308.

[93] S.S. Hegedus, W.N. Shafarman, Thin-film solar cells: device measurements and analysis, Prog. Photovoltaics Res. Appl. 12 (2004) 155–176. doi:10.1002/pip.518.

[94] P.M.P. Salomé, B. Vermang, R. Ribeiro-Andrade, J.P. Teixeira, J.M.V. Cunha, M.J. Mendes, S. Haque, J. Borme, H. Águas, E. Fortunato, R. Martins, J.C. González, J.P. Leitão, P.A. Fernandes, M. Edoff, S. Sadewasser, Passivation of Interfaces in Thin Film Solar Cells: Understanding the Effects of a Nanostructured Rear Point Contact Layer, Adv. Mater. Interfaces. 5 (2017) 1701101. doi:10.1002/admi.201701101.

[95] R. Scheer, Activation energy of heterojunction diode currents in the limit of interface recombination, J. Appl. Phys. 105 (2009) 104505. doi:10.1063/1.3126523.

110

[96]   E.T. Roe, K.E. Egelhofer, M.C. Lonergan, Exchange current density model for the contact-determined current-voltage behavior of solar cells, J. Appl. Phys. 125 (2019) 225302. doi:10.1063/1.5090519.

[97]   Y.S. Lee, T. Gershon, T.K. Todorov, W. Wang, M.T. Winkler, M. Hopstaken, O. Gunawan, J. Kim, Atomic Layer Deposited Aluminum Oxide for Interface Passivation of $Cu_2ZnSn(S,Se)_4$ Thin-Film Solar Cells, Adv. Energy Mater. 6 (2016) 1600198. doi:10.1002/aenm.201600198.

[98]   S. Luo, C. Eisler, T.H. Wong, H. Xiao, C.E. Lin, T.T. Wu, C.H. Shen, J.M. Shieh, C.C. Tsai, C.W. Liu, H.A. Atwater, W.A. Goddard, J.H. Lee, J.R. Greer, Suppression of surface recombination in $CuInSe_2$ (CIS) thin films via Trioctylphosphine Sulfide (TOP:S) surface passivation, Acta Mater. 106 (2016) 171–181. doi:10.1016/j.actamat.2016.01.021.

[99]   J. Joel, B. Vermang, J. Larsen, O. Donzel-Gargand, M. Edoff, On the assessment of CIGS surface passivation by photoluminescence, Phys. Status Solidi - Rapid Res. Lett. 9 (2015) 288–292. doi:10.1002/pssr.201510081.

[100]   W.K. Metzger, I.L. Repins, M. Romero, P. Dippo, M. Contreras, R. Noufi, D. Levi, Recombination kinetics and stability in polycrystalline $Cu(In,Ga)Se_2$ solar cells, Thin Solid Films. 517 (2009) 2360–2364. doi:10.1016/j.tsf.2008.11.050.

[101]   R.M. Langford, C. Clinton, In situ lift-out using a FIB-SEM system, Micron. 35 (2004) 607–611. doi:10.1016/j.micron.2004.03.002.

[102]   O. Donzel-Gargand, The multiple faces of Interfaces - Electron micrososcopy analysis of $CuInSe_2$ thin-film solar cells, Uppsala University, 2018.

[103]   P.M.P. Salomé, H. Rodriguez-Alvarez, S. Sadewasser, Incorporation of alkali metals in chalcogenide solar cells, Sol. Energy Mater. Sol. Cells. 143 (2015) 9–20. doi:10.1016/j.solmat.2015.06.011.

[104]   R. Caballero, M. Nichterwitz, A. Steigert, A. Eicke, I. Lauermann, H.W. Schock, C.A. Kaufmann, Impact of Na on $MoSe_2$ formation at the CIGSe/Mo interface in thin-film solar cells on polyimide foil at low process temperatures, Acta Mater. 63 (2014) 54–62. doi:10.1016/j.actamat.2013.09.051.

[105]   D. Rudmann, A.F. Cunha, M. Kaelin, F. Kurdesau, H. Zogg, A.N. Tiwari, G. Bilger, Efficiency enhancement of $Cu(In,Ga)Se_2$ solar cells due to post-deposition Na incorporation, Appl. Phys. Lett. 84 (2004) 1129. doi:10.1063/1.1646758.

[106]   D. Rudmann, D. Bŕmaud, H. Zogg, A.N. Tiwari, Na incorporation into $Cu(In,Ga)Se_2$ for high-efficiency flexible solar cells on polymer foils, J. Appl. Phys. 97 (2005) 10–15. doi:10.1063/1.1857059.

[107]   D. Rudmann, Effects of sodium on growth and properties of $Cu(In,Ga)Se_2$ thin films and solar cells, Swiss federal institute of technology (ETH) Zurich, 2004.

[108]   M.A. Contreras, B. Egaas, P. Dippo, J. Webb, J. Granata, K. Ramanathan, S. Asher, A. Swartzlander, R. Noufi, On the role of Na and modifications to $Cu(In,Ga)Se_2$ absorber materials using thin-MF (M=Na, K, Cs) precursor layers, in: 26th IEEE Photovolt. Spec. Conf., IEEE, Anaheim, CA, USA, 1997: pp. 359–362. doi:10.1109/PVSC.1997.654102.

[109]   S. Wei, S.B. Zhang, A. Zunger, Effects of Na on the electrical and structural properties of CuInSe$_2$, J. Appl. Phys. 85 (1999) 7214–7218. doi:10.1063/1.370534.

[110]   Z.-K. Yuan, S. Chen, Y. Xie, J. Park, H. Xiang, X. Gong, S.-H. Wei, Na-Diffusion Enhanced p-type Conductivity in Cu(In,Ga)Se2: A New Mechanism for Efficient Doping in Semiconductors, Adv. Energy Mater. 6 (2016) 1601191. doi:10.1002/aenm.201601191.

[111]   T. Wada, N. Kohara, S. Nishiwaki, T. Negami, Characterization of the Cu(In,Ga)Se$_2$/Mo interface in CIGS solar cells, Thin Solid Films. 387 (2001) 118–122. doi:10.1016/S0040-6090(00)01846-0.

[112]   N. Kohara, S. Nishiwaki, Y. Hashimoto, T. Negami, T. Wada, Electrical properties of the Cu(In,Ga)Se$_2$/MoSe$_2$/Mo structure, Sol. Energy Mater. Sol. Cells. 67 (2001) 209–215. doi:10.1016/S0927-0248(00)00283-X.

[113]   J. Yoon, J. Kim, W. Kim, Electrical properties of CIGS/Mo junctions as a function of MoSe$_2$ orientation and Na doping, Prog. Photovoltaics Res. Appl. 22 (2014) 90–96. doi:10.1002/pip.

[114]   T. Umehara, K. Nakada, A. Yamada, Impact of roll-over-shaped current–voltage characteristics and device properties of Ag(In,Ga)Se$_2$ solar cells, Jpn. J. Appl. Phys. 56 (2017) 012302. doi:10.7567/JJAP.56.012302.

[115]   E. Jarzembowski, F. Syrowatka, K. Kaufmann, W. Fränzel, T. Hölscher, R. Scheer, The influence of sodium on the molybdenum/Cu(In,Ga)Se$_2$ interface recombination velocity, determined by time resolved photoluminescence, Appl. Phys. Lett. 107 (2015) 051601. doi:10.1063/1.4928187.

[116]   B. Vermang, V. Fjällström, J. Pettersson, P. Salomé, M. Edoff, Development of rear surface passivated Cu(In,Ga)Se$_2$ thin film solar cells with nano-sized local rear point contacts, Sol. Energy Mater. Sol. Cells. 117 (2013) 505–511. doi:10.1016/j.solmat.2013.07.025.

[117]   B. Vermang, J.T. Wätjen, V. Fjällström, F. Rostvall, M. Edoff, R. Kotipalli, F. Henry, D. Flandre, Employing CIGS solar cell technology to increase efficiency of ultra-thin Cu(In,Ga)Se$_2$ solar cells, Prog. Photovoltaics Res. Appl. 22 (2014) 1023–1029. doi:10.1002/pip.

[118]   B. Vermang, J.T. Wätjen, C. Frisk, V. Fjällstrom, F. Rostvall, M. Edoff, P. Salome, J. Borme, N. Nicoara, S. Sadewasser, Introduction of Si PERC rear contacting design to boost efficiency of Cu(In,Ga)Se$_2$ solar cells, IEEE J. Photovoltaics. 4 (2014) 1644–1649. doi:10.1109/JPHOTOV.2014.2350696.

[119]   F. Mollica, J. Goffard, M. Jubault, F. Donsanti, S. Collin, A. Cattoni, L. Lombez, N. Naghavi, Comparative study of patterned TiO$_2$ and Al$_2$O$_3$ layers as passivated back-contact for ultra-thin Cu(In,Ga)Se$_2$ solar cells, 43rd IEEE Photovolt. Spec. Conf. (2016) 2213–2217. doi:10.1109/PVSC.2016.7750028.

[120]   W.-W. Hsu, J.Y. Chen, T.-H. Cheng, S.C. Lu, W.-S. Ho, Y.-Y. Chen, Y.-J. Chien, C.W. Liu, Surface passivation of Cu(In,Ga)Se$_2$ using atomic layer deposited Al$_2$O$_3$, Appl. Phys. Lett. 100 (2012) 023508. doi:10.1063/1.3675849.

[121] E. Jarzembowski, B. Fuhrmann, H. Leipner, W. Fränzel, R. Scheer, Ultrathin Cu(In,Ga)Se$_2$ solar cells with point-like back contact in experiment and simulation, Thin Solid Films. 633 (2017) 61–65. doi:10.1016/j.tsf.2016.11.003.

[122] G. Yin, M. Song, S. Duan, P. Manley, D. Greiner, C.A. Kaufmann, M. Schmid, Well-controlled dielectric nanomeshes by colloidal nanosphere lithography for optoelectronic enhancement of ultrathin Cu(In,Ga)Se$_2$ solar cells, ACS Appl. Mater. Interfaces. 8 (2016) 31646–31652. doi:10.1021/acsami.6b10135.

[123] W. Ohm, W. Riedel, Ü. Askünger, M.D. Heinemann, C.A. Kaufmann, J.L. Garcia, V. Izquierdo, X. Fontané, T. Goislard, M.C. Lux-Steiner, S. Gledhill, An overview of technological aspects of Cu(In,Ga)Se2 solar cell architectures incorporating ZnO nanorod arrays, Phys. Status Solidi. 212 (2015) 76–87. doi:10.1002/pssa.201431230.

[124] J.M.V. Cunha, P.A. Fernandes, A. Hultqvist, J.P. Teixeira, S. Bose, B. Vermang, S. Garud, D. Buldu, J. Gaspar, M. Edoff, J.P. Leitao, P.M.P. Salome, Insulator Materials for Interface Passivation of Cu(In,Ga)Se$_2$Thin Films, IEEE J. Photovoltaics. 8 (2018) 1313–1319. doi:10.1109/JPHOTOV.2018.2846674.

[125] A. Morato, B. Vermang, H. Goverde, E. Cornagliotti, G. Meneghesso, J. John, J. Poortmans, Electrical characterization of ALD Al2O3-HfO2 and PECVD Al2O3 passivation layers for p-type CZ-Silicon PERC solar cells, in: 38th IEEE Photovolt. Spec. Conf., 2012: pp. 001077–001082. doi:10.1109/PVSC.2012.6317790.

[126] T. Tachibana, T. Sameshima, Y. Iwashita, Y. Kiyota, T. Chikyow, H. Yoshida, K. Arafune, S.I. Satoh, A. Ogura, Material research on high-quality passivation layers with controlled fixed charge for crystalline silicon solar cells, Jpn. J. Appl. Phys. 50 (2011) 04DP09-1-04DP09-4. doi:10.1143/JJAP.50.04DP09.

[127] J. Cui, Y. Wan, Y. Cui, Y. Chen, P. Verlinden, A. Cuevas, Highly effective electronic passivation of silicon surfaces by atomic layer deposited hafnium oxide, Appl. Phys. Lett. 110 (2017) 021602-1-021602–5. doi:10.1063/1.4973988.

[128] J. Cui, S.P. Phang, H.C. Sio, Y. Wan, Y. Chen, P. Verlinden, A. Cuevas, Passivation of Phosphorus Diffused Black Multi-Crystalline Silicon by Hafnium Oxide, Phys. Status Solidi - Rapid Res. Lett. 11 (2017) 1700296. doi:10.1002/pssr.201700296.

[129] X. Cheng, P. Repo, H. Halvard, A.P. Perros, E.S. Marstein, M. Di Sabatino, H. Savin, Surface Passivation Properties of HfO$_2$ Thin Film on n-Type Crystalline Si, IEEE J. Photovoltaics. 7 (2017) 479–485. doi:10.1109/JPHOTOV.2016.2645399.

[130] E. Polydorou, M. Botzakaki, C. Drivas, K. Seintis, I. Sakellis, A. Soultati, A. Kaltzoglou, T. Speliotis, M. Fakis, L.C. Palilis, S. Kennou, A. Fakharuddin, L. Schmidt-Mende, D. Davazoglou, P. Falaras, P. Argitis, C.A. Krontiras, S.N. Georga, M. Vasilopoulou, Insights into the passivation effect of atomic layer deposited hafnium oxide for efficiency and stability enhancement in organic solar cells, J. Mater. Chem. C. 6 (2018) 8051–8059. doi:10.1039/c8tc02243g.

[131] J.T. Gaskins, P.E. Hopkins, D.R. Merrill, S.R. Bauers, E. Hadland, D.C. Johnson, D. Koh, J.H. Yum, S. Banerjee, B.J. Nordell, M.M. Paquette, A.N. Caruso, W.A. Lanford, P. Henry, L. Ross, H. Li, L. Li, M. French, A.M. Rudolph, S.W. King, Review—Investigation and Review of the Thermal, Mechanical, Electrical, Optical, and Structural Properties of Atomic Layer Deposited High-k Dielectrics: Beryllium Oxide, Aluminum Oxide, Hafnium Oxide, and Aluminum Nitride, ECS J. Solid State Sci. Technol. 6 (2017) N189–N208. doi:10.1149/2.0091710jss.

[132] H.Y. Yu, M.F. Li, D.L. Kwong, ALD $(HfO_2)_x Al_2O_3)_{1-x}$ high-k gate dielectrics for advanced MOS devices application, Thin Solid Films. 462–463 (2004) 110–113. doi:10.1016/j.tsf.2004.05.010.

[133] S. Bose, J.M.V. Cunha, S. Suresh, D. Wild de, T.S. Lopes, J.R.S. Barbosa, R. Silva, J. Borme, P.A. Fernandes, B. Vermang, P.M.P. Salomé, Optical Lithography patterning of SiO_2 layers for interface passivation of thin film solar cells, Sol. RRL. 11 (2018) 1800212. doi:10.1002/solr.201800212.

[134] W. Ohm, W. Riedel, U. Aksunger, D. Greiner, C.A. Kaufmann, M.C. Lux-Steiner, S. Gledhill, Bifacial $Cu(In,Ga)Se_2$ solar cells with submicron absorber thickness: back-contact passivation and light management, in: IEEE 42nd Photovolt. Spec. Conf., 2015: pp. 1–5. doi:10.1109/PVSC.2015.7356416.

[135] N. Tarr, D. Pulfrey, D.S. Camporese, An analytic model for the MIS tunnel junction, IEEE Trans. Electron Devices. 30 (1983) 1760–1770. doi:10.1109/T-ED.1983.21442.

[136] Mohamed Yehya Doghish and Fat Duen Ho, A comprehensive analytical model for metal-insulator-semiconductor (MIS) devices: A solar cell application, IEEE Trans. Ele. 40 (1992) 1446–1454.

[137] S.K. Krawczyk, New method for the determination of the surface barrier heights in mis tunnel diodes (solar cells), Solid. State. Electron. 25 (1982) 1027–1031.

[138] P. Chattopadhyay, A.N. Daw, On the current transport mechanism in a metal-insulator-semiconductor (MIS) diode, Solid State Electron. 29 (1986) 555–560. doi:10.1016/0038-1101(86)90078-X.

[139] S. Nigo, M. Kubota, Y. Harada, T. Hirayama, S. Kato, H. Kitazawa, G. Kido, Conduction band caused by oxygen vacancies in aluminum oxide for resistance random access memory, J. Appl. Phys. 112 (2012) 033711. doi:10.1063/1.4745048.

[140] Z.Q. Liu, D.P. Leusink, W.M. Lü, X. Wang, X.P. Yang, K. Gopinadhan, Y.T. Lin, A. Annadi, Y.L. Zhao, A.R. Barman, S. Dhar, Y.P. Feng, H.B. Su, G. Xiong, T. Venkatesan, Ariando, Reversible metal-insulator transition in LaAlO3 thin films mediated by intragap defects: An alternative mechanism for resistive switching, Phys. Rev. B. 84 (2011) 165106. doi:10.1103/PhysRevB.84.165106.

[141] C. Jin, H. Lu, Y. Zhang, Y. Zhang, H. Guan, L. Wu, B. Lu, C. Liu, Transport mechanisms of leakage current in Al_2O_3/InAlAs MOS capacitors, Solid. State. Electron. 123 (2016) 106–110. doi:10.1016/j.sse.2016.06.006.

[142]   B.J. Palmer, Improved Rear Surface Passivation of Cu(In,Ga)Se$_2$ Solar
        Cells : A Combination of an Al$_2$O$_3$ Rear Surface Passivation Layer and
        Nanosized Local Rear Point Contacts, Diploma Thesis, Uppsala, 2017.

[143]   A. Han, Y. Zhang, W. Song, B. Li, W. Liu, Y. Sun, Structure, morphology
        and properties of thinned Cu(In,Ga)Se2 films and solar cells, Semicond. Sci.
        Technol. 27 (2012) 035022. doi:10.1088/0268-1242/27/3/035022.

[144]   C. Frisk, C. Platzer-Björkman, J. Olsson, P. Szaniawski, J.T. Wätjen, V.
        Fjällström, P. Salome, M. Edoff, Optimizing Ga-profiles for highly efficient
        Cu(In,Ga)Se$_2$ thin film solar cells in simple and complex defect models, J. Phys.
        D. Appl. Phys. 47 (2014) 485104. doi:10.1088/0022-3727/47/48/485104.

[145]   M. Burgelman, P. Nollet, S. Degrave, Modelling polycrystalline
        semiconductor solar cells, Thin Solid Films. 361 (2000) 527–532.
        doi:10.1016/S0040-6090(99)00825-1.

[146]   M.I. Alonso, M. Garriga, C.A. Durante Rincón, E. Hernández, M. León,
        Optical functions of chalcopyrite CuGa$_x$In$_{1-x}$Se$_2$ alloys, Appl. Phys. A Mater.
        Sci. Process. 74 (2002) 659–664. doi:10.1007/s003390100931.

[147]   K. Orgassa, Coherent optical analysis of the ZnO/CdS/Cu(In,Ga)Se$_2$ thin
        film solar cell, Universität Stuttgart, 2004.

[148]   P.D. Paulson, R.W. Birkmire, W.N. Shafarman, Optical characterization of
        CuIn$_{1-x}$Ga$_x$Se$_2$ alloy thin films by spectroscopic ellipsometry, J. Appl. Phys.
        94 (2003) 879. doi:10.1063/1.1581345.

[149]   P. Zhang, Y.Y. Lau, R.S. Timsit, Spreading resistance of a contact spot on a
        thin film, in: 59th IEEE Holm Conf. Electr. Contacts, Newport, RI, USA,
        2013: pp. 1–7. doi:10.1109/HOLM.2013.6651426.

[150]   P. Zhang, Y.Y. Lau, R.S. Timsit, On the spreading resistance of thin-film
        contacts, IEEE Trans. Electron Devices. 59 (2012) 1936–1940.
        doi:10.1109/TED.2012.2195317.

[151]   M.B. Read, J.H. Lang, A.H. Slocum, R. Martens, Contact Resistance in Flat
        Thin Films, in: 55th IEEE Holm Conf. Electr. Contacts, 2009: pp. 303–309.
        doi:10.1109/HOLM.2009.5284385.

[152]   M.W. Denhoff, An accurate calculation of spreading resistance, J. Phys. D.
        Appl. Phys. 39 (2006) 1761–1765. doi:10.1088/0022-3727/39/9/009.

[153]   B. Gelmont, M. Shur, Spreading resistance of a round ohmic contact, Solid.
        State. Electron. 36 (1993) 143–146. doi:10.1016/0038-1101(93)90132-A.

[154]   M.S. Leong, S.C. Choo, L.S. Tan, The role of source boundary condition in
        spreading resistance calculations, Solid. State. Electron. 21 (1978) 933–941.
        doi:10.1016/0038-1101(78)90291-5.

[155]   R. Cox, H. Strack, Ohmic contacts for GaAs devices, Solid. State. Electron.
        10 (1967) 1213–1218. doi:10.1016/0038-1101(67)90063-9.

[156]   R.D. Brooks, H.G. Mattes, Spreading Resistance Between Constant
        Potential Surfaces, Bell Syst. Tech. J. 50 (1971) 775–784.
        doi:10.1002/j.1538-7305.1971.tb01882.x.

[157]   P. Salomé, V. Fjällström, A. Hultqvist, M. Edoff, Na doping of CIGS solar
        cells using low sodium-doped Mo layer, IEEE J. Photovoltaics. 3 (2013)
        509–513. doi:10.1109/JPHOTOV.2012.2226144.

[158]   X.X. Liu, J.R. Sites, Solar-cell collection efficiency and its variation with
        voltage, J. Appl. Phys. 75 (1994) 577. doi:10.1063/1.355842.

Sammanfattning på Svenska

Omfattande ansträngningar görs för att ställa om energisystem från fossila energikällor till förnybara energikällor, som solenergi, eftersom fossila energikällor har allvarliga begränsningar. För det första är både mängden och utnyttjandetakten av fossila resurser begränsade. För det andra är de ojämnt fördelade över världen. Därför är priser och tillgång till fossil energi delvis politiskt bestämda och fluktuerar så kraftigt, att energisäkerheten är hotad. Slutligen bidrar användningen av fossil energi allra mest till den mänskligt orsakade globala uppvärmningen.

Förnybara energiresurser är dock inte direkt användbara, utan en energisystemkomponent behöver omvandla dem till en energibärare eller till sekundär energi, som i sin tur levererar en energitjänst (på engelska: energy service) till slutkonsumenten. Solceller är en sådan energisystemkomponent för förnybar energi. De omvandlar solenergi till elektrisk energi, som omvandlas till slutet till exempel till potentiell energi när en kranförare lyfter en vikt med hjälp av en lyftkran. Behovet av material för att bygga energisystemkomponenter behöver också betraktas både från ett kostnads- och ett energisäkerhetsperspektiv. Mängden och produktionstakten för material från primär- och sekundärresurser (dvs. från återvinning) är i princip begränsade och exploaterbara malmer är ojämnt fördelade över världen. Brister och stora prisfluktuationer är således inte heller ovanliga. För $Cu(In,Ga)Se_2$ (CIGS) tunnfilmssolceller är det indium i det ljusabsorberande skiktet som är mest problematiskt.

Således kan en minskning av materialanvändning per serviceenhet (från engelskan: material input per unit of service (MIPS)) förbättra energisäkerheten och bidra till att stabilisera och/eller minska energikostnaden. Allt annat lika reduceras materialanvändningen per serviceenhet om (1) samma mängd energitjänster tillhandahålls med mindre materialanvändning i energisystemkomponenten eller (2) om energitjänstens mängd ökar för samma materialanvändning. I fallet med solceller reduceras materialanvändningen per energiserviceenhet om tex. de ljusabsorberande skikten tunnas ner utan förlust i omvandlingseffektivitet eller om omvandlingseffektiviteten förbättras utan en ökning av material-användningen.

Lyckligtvis kan en minskning av de ljusabsorberande skikten i solceller öka omvandlingseffektiviteten. När dessa skikt tunnas ner, begränsas samma antal fria laddningsbärare (i.e. elektron och hål) till en mindre absorptionsvolym,

förutsatt att generationstakten och rekombinationstakten av fria laddningsbärare vid fram- och bakytorna av det absorberande skiktet inte förändras. Förhöjda koncentrationer av fria laddningsbärare ökar avståndet mellan kvasi-Fermi-nivåerna, vilket kan öka spänningen i en öppen strömkrets.

För verkliga CIGS-solceller ökar emellertid både absorptionsförlusterna och rekombinationstakten i gränsytan mellan det absorberande CIGS-skiktet och Mo-bakkontakten vid minskningen av CIGS-skiktets tjocklek. Avståndet mellan kvasi-Fermi-nivåerna i CIGS-skiktet, spänningen vid öppen strömkrets, kortslutningsströmmen, fyllnadsfaktorn, och därigenom omvandlingseffektiviteten minskar. Sålunda är både en passivering av CIGS-skiktets bakre yta och en optisk optimering avgörande för att bibehålla en hög omvandlingseffektivitet i CIGS-solceller, när solcellens CIGS-skikt tunnas ner.

Passivering av en yta minskar per definition den lokala rekombinationstakten av elektroner och hål där. En yta kan passiveras genom att antingen minska tätheten av defekter på ytan (kemisk passivering) och/eller genom att göra en laddningsbärarkoncentration mycket mindre än den andra (populationskontroll av laddningsbärare). CIGS-skikten i moderna CIGS-solceller är vanligen Ga-graderade med ett högt Ga-innehåll och därmed högre bandgap vid baksidan för att höja hålkoncentrationen och minska elektronkoncentrationen där. Istället för Ga-gradering, införs i detta arbete tunna oxidskikt, så kallade passiveringsskikt, mellan CIGS skitet och Mo-kontakten. De kan passivera CIGS-ytan om CIGS-oxid-gränsytan har en lägre defekttäthet än CIGS-Mo-gränsytan och/eller om de innehåller en negativ oxidladdning, vilket ökar hålkoncentrationen och minskar elektron-koncentration i CIGS i närheten av oxiden.

Eftersom oxider är isolatorer måste den elektriska ledningsförmågan genom passiveringsskiktet säkerställas. Detta görs vanligtvis genom att öppna passiveringsskiktet i ett extra tillverkningssteg, varigenom en direkt elektrisk kontakt upprättas mellan CIGS och Mo. Följaktligen gjordes i en del av detta arbete nanopunktkontakter i passiveringsskiktet. Passiveringsskiktet användes i solceller med ett CIGS-skikt med ett stort bandgap, dvs. CIGS med ett högt gallliuminnehåll och ett lågt indiuminnehåll, för att utforska om ett sådant CIGS-material kan passiveras med hjälp av ett passiveringsskikt. Diffusionslängden för minoritetsladdningsbärare i CIGS med så högt galliuminnehåll är kort jämfört med diffusionslängden i CIGS med lägre galliuminnehåll. Därför är en passiveringseffekt mindre sannolik. Trots detta kunde en passiveringseffekt fastställas med hjälp av mätningar av kvanteffektiviteten och ström-spänningsmätningar under olika temperaturer i samband med optisk och elektrisk modellering.

Dessutom har möjligheten att undvika det extra tillverkningssteget med mönstring av oxiden utforskats för två olika oxider. Resultaten tyder på att passiveringsskiktet inte nödvändigtvis behöver öppnas för elektrisk ledning i

ett ytterligare tillverkningssteg, om en lämplig kombination av det passiverande materialet och ett tillräckligt tjockt lager av NaF läggs på passiveringsskiktet innan CIGS-förångningen. I detta fall har solceller med ett 215 nm tunt CIGS-skikt och ett 6 nm tunt passiverande Al_2O_3-skikt en omvandlingseffektivitet på 8,6%, vilket är 3% (absolut) högre än omvandlingseffektiviteten på referenssolceller utan passiverande skikt. För HfO_2-skikten indikerar fotoluminescensdata en bra passiveringseffekt, men NaF ökade inte HfO_2-skiktens ledningsförmåga i tillräckligt hög utsträckning och skiktet måste därför öppnas för att säkerställa ledningsförmågan.

Acta Universitatis Upsaliensis

Digital Comprehensive Summaries of Uppsala Dissertations from the Faculty of Science and Technology 1834

Editor: The Dean of the Faculty of Science and Technology

ACTA
UNIVERSITATIS
UPSALIENSIS
UPPSALA
2019